

PIEZOREFLECTANCE AND ELECTRONIC STRUCTURE  
OF ALLOYS OF COPPER WITH POLYVALENT SOLUTES

by

Michael Philip Staines

Submitted for the degree of Doctor of Philosophy  
in Physics at Victoria University of Wellington

October, 1979

## ABSTRACT

Piezoreflectance and other optical measurements have been made on  $\alpha$  phase alloys of Cu with Zn, Ga, Al, In and Ge. The samples were evaporated films deposited on the face of a resonant oscillator assembly. The application of this type of strain transducer to piezoreflectance alleviates systematic errors and allows the response to pure shear strains to be distinguished, even in amorphous materials, using the polarisation dependence of the results.

The energies of the d band  $\rightarrow$  Fermi level threshold, the interconduction band threshold, and the  $L_2' \rightarrow L_1$  critical point transition were determined for the alloys. Previous optical studies using more conventional methods either have not been able to resolve these features or have not located them with accuracy comparable with piezoreflectance.

With increasing alloy concentration the d band threshold is found to shift slowly to higher energies, the interconduction band transitions more rapidly to lower energies. Zn impurities produced much smaller shifts than the others, indicating the importance of interactions between impurity d states and the d and conduction states of the host. Significant differences were found between the isovalent solutes Ga and Al. In concentrated alloys with Zn, Ga and Al the interconduction band threshold tended to a common value of about 2.5 eV.

This lack of simple dependence on  $\frac{e}{a}$ , the electron per atom density in the alloy, is relevant to the understanding of the electronic structure of the Hume-Rothery alloys and the regularity of the  $\alpha$  phase boundary.

## ACKNOWLEDGEMENTS

I would like to thank David Beaglehole for introducing me to the field of optical studies and for his support and advice in the course of this work.

Thanks are also due to Dr. Colin Cook for helpful comments, Dr. Bill Robinson for his interest in the project, Dr. W. Darcey for the use of his X-ray fluorescence equipment and Dr. K. Brown and the Chemistry Division of the DSIR for access to the X-ray diffractometer.

Thanks to Dave Gilmour and other technical staff for their help and to Dave, Joe, Bob and others for making my time at VUW a pleasant one,

Lastly I am thankful for the patience shown by my wife Janice and our family.

## CONTENTS

	PAGE
Abstract	i
Acknowledgements	ii
List of Figures and Tables	iv
Chapter 1 INTRODUCTION	1
Chapter 2 THEORETICAL BACKGROUND	
2.1 Electronic Structure of Copper	5
2.2 Alloys:	
Screening	9
Localised states	13
Band structure of alloys	13
Perturbations of the band structure	15
Modern alloy theories	19
2.3 Optical Properties:	
Macroscopic description	19
Microscopic description	21
Intraband transitions	21
Critical points	23
Indirect transitions	25
2.4 Strain-Optic Response:	
Macroscopic description	30
Microscopic description	31
Strain-optic properties of thin films	38
Chapter 3 SAMPLE PREPARATION AND CHARACTERISATION	
3.1 Sample Preparation:	
Multiple sample preparation	39
Deposition monitors	41
Substrates	42
Vacuum system	43
Sources	43
Deposition	44
Annealing	46
3.2 Sample Characterisation:	
Resistivity	47
Lattice constants	50
X-ray fluorescence	52



	PAGE
Summary of results	53
Film structure	55
Chapter 4 OPTICAL MEASUREMENTS	
4.1 Piezoreflectance:	
Optical system	57
Strain transducer	59
Electronics	62
Accuracy	64
4.2 Differential Reflectance	66
Optical system	67
Sample interchange and precision	69
4.3 Angle of Incidence Modulation System	71
4.4 Results:	
Data processing	72
Pure copper results	73
Line fitting	78
Alloy results	83
Comparison with other optical results	92
Chapter 5 DISCUSSION	
5.1 d bands	102
5.2 Fermi Level	108
5.3 Conduction Bands:	
Interpolation band scheme	110
Alloy parameters	112
Comparison with experiment	115
Results at high concentration	120
5.4 Comparison with Alloy Band Structure	
Calculations	121
5.5 Hume-Rothery $\alpha$ phase Boundary Rule	122
5.6 Summary of Experimental Findings and	
Conclusions	124
APPENDICES	
1 Strain-optic response of textured	
films	126

	PAGE
2 Alloy concentration from resistance and XRF measurements	127
3 Notes on experimental systems	128
4 Computing	130
REFERENCES	136

## LIST OF FIGURES

	Page
2. 1 Brillouin zone and band structure of copper	6
2. 2 Renormalised atom viewpoint of electronic structure: copper atomic wavefunctions, renormalisation and band contributions of energy levels in solid copper.	8
2. 3 Charge density distribution surrounding a charged impurity	10
2. 4 Charge transfer at interfaces in metals and its effect on the crystal potential	12
2. 5 Change in the Fermi energy per unit excess valence with concentration of impurity in copper, according to Friedel.	12
2. 6 Distribution of wavenumber in an eigenstate of a dilute alloy.	14
2. 7 Rigid band energy shifts in a free-electron metal alloy	17
2. 8 Examples of single electron optical transitions in metals	22
2. 9 Important critical point transitions in copper	26
2.10 Interband $\epsilon_2$ spectra for copper: experimental and theoretical	27
2.11 Direct and indirect thresholds for interconduction band transitions near L	29
2.12 Derivative line shape for broadened square root singularity	35
2.13 Piezo-optic constants for copper from the experimental measure- ments of Gerhardt (1968)	37
3. 1 Placement of components in vacuum system for multiple sample deposition	40
3. 2 Typical measurements for composition analysis: (a) X-ray diffraction line shapes (b) X-ray fluorescence spectra	51
4. 1 Piezoreflectance optical system schematic diagram	58
4. 2 Piezoreflectance strain transducer	60
4. 3 Piezoreflectance system electronics - schematic diagram	63
4. 4 Typical experimental piezoreflectance trace for pure copper film	65
4. 5 Differential reflectometer: optics, spinner, detector output	68
4. 6 Differential reflectance system electronics	70
4. 7 Difference between effective aperture sizes of differential reflectance spinner for reflected and transmitted beams	70
4. 8 Measured reflectance and $\epsilon_2$ spectra for a pure copper film	74
4. 9 Strain normalised $\frac{\Delta R}{R}$ piezoreflectance spectra for a pure copper film	75
4.10 Comparison between single crystal piezoreflectance results and present results for vacuum-deposited films	76

4.11	$(\hbar\omega)^2 \Delta\epsilon_2/e$ spectra for pure copper film	79
4.12	Line fit to interconduction band piezo-optic structure for a pure copper film	81
4.13	Line fit to d band threshold piezo-optic structure for a pure copper film	82
4.14	Strain normalised $\frac{\Delta R}{R}$ and $(\hbar\omega)^2 \Delta\epsilon_2$ spectra for alloys of copper with Zn, Ga, Al, In, and Ge	84-88
4.15	Examples of linefitting piezo-optic structure in alloys	90
4.16	Critical energy for d band threshold transitions as a function of alloy composition	93
4.17	Critical energy for interconduction band transitions $E_F \rightarrow Q_+(L_1^u)$ and $L_2^c \rightarrow L_1^u$ as a function of alloy composition	94
4.18	Examples of determination of d band threshold from static $\epsilon_2$ spectra	96
4.19	Examples of alloy $\epsilon_2$ spectra with critical energies determined from piezoreflectance results marked	97
4.20-4.21	Comparison of piezoreflectance results with those of other workers for the d band and interconduction band thresholds	99-100
5. 1	Shift rates of the d band threshold at low concentration	107
5. 2	Variation in the Fermi energy: the d band threshold energies in alloys at higher concentration with linear contribution to the shift subtracted	109
5. 3	Shift rates of interconduction band critical energies at low concentration compared with theoretical estimates based on band structure interpolation scheme parameters	116
A1	Stray light and polariser data	131
A2	Effects of variation in data treatment on $(\hbar\omega)^2 \Delta\epsilon_2$ results	134

## LIST OF TABLES

	Page
2. 1 Properties of Van Hove singularities in the joint density of states	24
2. 2 Piezo-optic tensor definitions and selection rules	32
2. 3 Critical energies and deformation potentials for important energy gaps in the band structure of copper	34
2.4 Piezo-optic response signatures of singularities in the joint density of states of copper	36
3. 1 Vacuum deposition sources	45
3. 2 Residual resistivity reference data	49
3. 3 Lattice constant reference data	49
4. 1 List of critical energies for alloys determined from piezoreflectance measurements	91
5. 1 Measured rates of shift in the low concentration limit of the d band threshold energy $E_F - E_d^u$	103
5. 2 Changes in the lower conduction band near L as a fraction of the predictions of the rigid band approximation	118
5. 3 Comparison of results of average T-matrix calculations and experiment	121

## 1 INTRODUCTION

In this project the electronic structure of some copper-based  $\alpha$  phase alloys has been investigated by piezoreflectance: the response of the reflectance to strain modulation. The  $\alpha$  phase alloys - sometimes called solid solutions - of the noble metals are disordered substitutional alloys with the same face-centred cubic structure as the host. In this chapter the reasons for using this technique and for the interest in this group of alloys are discussed.

Optical studies have the virtue of being one of the few methods of investigating the density of electronic states in metals at energies appreciably removed from the Fermi level.\* However, there are difficulties - experimental and intrinsic - in their application. Because visible light penetrates only a few hundred angstroms in typical metals they are almost always studied in reflectance, which is difficult to measure absolutely and is much affected by surface condition. Consequently experimental results seldom agree in detail. In contrast to the spectroscopy of atoms, molecules and insulators, the spectra obtained are typically quite smooth and featureless (see the review by Nilsson (1974)), because they are due to electronic transitions by a variety of mechanisms within and between several broad bands. A reliable band structure calculation is almost essential for their interpretation.

The advent of modulation spectroscopy (Cardona, 1969; Seraphin, 1972, 1973) - the study of the effects on the optical properties of the solid of an external perturbation (commonly strain, temperature or electric field) has

---

\*Standard photoemission studies are not able to resolve conduction band features or slight changes in alloy d bands. Fermi surface studies, with the exception of positron annihilation, are confined to extremely dilute alloys.

contributed much to optical studies of solids in the last decade. The advantage of modulation techniques is that the spectra typically have pronounced structure with little background and features can often be unambiguously assigned to a particular transition by considering the form of the response signature or the symmetry of tensorial perturbations. The underlying reasons for the increased resolution and for the selection rules applicable to symmetry-breaking perturbations are discussed in the following chapter.

The common modulated reflectance experiments are piezoreflectance (strain modulation), thermoreflectance (temperature), and electro-reflectance (electric field). Of these piezoreflectance is the "cleanest" in that only the dimensions and symmetry of the lattice are changed - in the others the mechanism of response is more complex.

Since the changes in reflectance caused by physically practicable modulation amplitudes are small, typically less than 1 part in  $10^4$ , the use of a.c. modulation and phase-sensitive detection is essential in most cases. A wide variety of strain modulators has been used by different workers (Cardona, 1969) involving magnetic, pneumatic and piezoelectric transducers in both bending and compressional modes. A common problem with transducers is vibration and sample motion synchronous with the modulation which may lead to unacceptable systematic errors. A novel composite piezoelectric transducer was used in this work which alleviates this problem and, despite the use of evaporated film samples, provides additional information from the polarisation-dependence of the response.

Most of the previous work has been done on semiconductors. In metals, the full set of single-crystal measurements (see Chapter 2) have been made on only the three noble metals (Gerhardt, 1968 (copper); Nilsson & Sandell, 1970 (silver); Szczepanek & Glosser, 1974 (gold)) complementing the earliest work on metal films evaporated on ceramic piezoelectric transducers, (Garfinkel et al, 1966). The technique has so far been little used in alloy studies

(Morris & Lynch, 1969 (Ag-In); Nilsson & Sandell, 1970 (Ag-Au)).

Several factors make copper-based alloys convenient and interesting to study. The electronic structure of the host, copper, is well understood having been intensively studied experimentally and theoretically. The important optical structure is accessible in the visible and near ultraviolet and is easily separable from the background of free-electron absorption.

Alloys of the noble metals with the polyvalent elements to their right in the periodic table, typified by Cu with Zn, Ga, Ge or As, are of interest because the difference in valence between impurity and solvent is the dominant perturbation introduced by the impurity.

Hume-Rothery's recognition in the 1930s of the importance of the concentration of conduction electrons per atom in determining the crystal structure of some phases of these alloys earned them his name. The limit of solubility of these impurities in the  $\alpha$  phase alloys occurs at  $\frac{e}{a}$  (electrons per atom) concentrations of about 1.4 - 40 at% Zn or 20 at% Ga etc. This has been attributed (Mott & Jones, 1936) to expansion of the Fermi surface to contact the Brillouin zone stabilising the fcc crystal structure relative to bcc until after contact is made due to the lowered energy of states below the energy band gap at the zone boundary. Since the volume of the Fermi surface is proportional to the electron density this explained the scaling of the phase boundary with  $\frac{e}{a}$ . Hume-Rothery and Roaf (1961) suggested that contact occurred at the (200) zone faces after it was found that in pure Cu the Fermi surface already contacts the (111) zone faces. Heine and Weaire (1970) raised several objections to this explanation including:

- i) contact at (200) requires the Fermi surface to expand too rapidly,
- ii) the effect of the d bands is neglected even though correlations of structure with  $\frac{e}{a}$  are most characteristic of noble metal-based alloys,
- iii) recent theory suggests the variation of total free energy



as the Fermi surface contacts a zone face is too slight to decisively influence the preferred crystal structure. Another point of view recently argued by Stroud and Ashcroft (1971) attributes the phase boundary rule to the screening anomaly in the dielectric function at twice the Fermi wavevector so that the effect is dependent on conduction electron density rather than on any particular feature of the band structure.

Piezoreflectance is almost uniquely qualified to resolve the question of contact at the (200) zone faces - the conduction band state ( $X_4'$ ) at which contact must occur figures prominently in the response to tetragonal shear strain in Cu whilst the corresponding structure is indistinguishable in static optical spectra. Although the relevant structure is obscured in the present measurements on polycrystalline film samples our results indirectly throw some light on the problem, and reveal an interesting common feature of the conduction bands as the phase boundary is approached, as well as providing accurate information about the perturbation of the electronic structure of copper by polyvalent impurities.

## 2 THEORETICAL BACKGROUND

In this chapter those aspects of the electronic structure and optical properties of metals and alloys relevant to the discussion of our results are briefly reviewed.

### 2.1 Electronic Structure of Copper

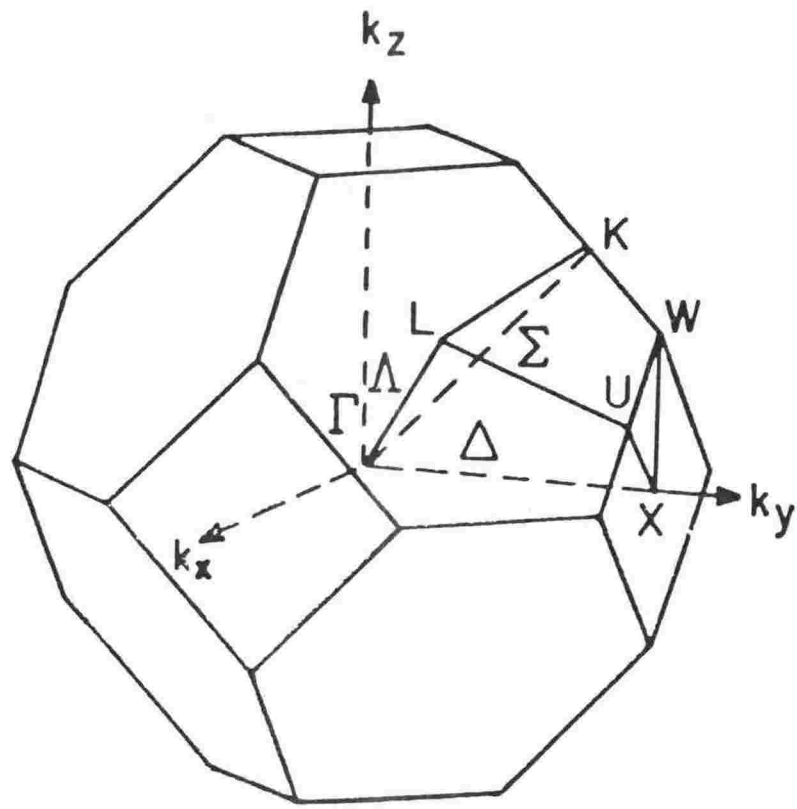
The central problem in much of the physics of perfect crystalline materials is the determination of the band structure,  $E(\underline{k})$ . Numerous calculations have been made for copper - fig.2.1 shows the band structure of copper along directions of high symmetry in the Brillouin zone as calculated by Segall (1962). Roughly speaking, it shows five narrow bands\* derived from the ten atomic d electrons - the d-bands - lying 2-5 eV below the Fermi level overlapping a broad, roughly parabolic band - the conduction band - accommodating the atomic s electron.

In fact, the distinction between conduction and d-bands is not absolute; except at certain symmetry points all states have an admixture of s, p and d character. This is particularly evident where the s and d-bands should cross - there the s-d hybridisation or mixing causes the conduction band and d-band of like symmetry to be repelled - see, for example, the  $\Lambda_1$ , and  $L_1$  states along  $\Gamma L$  in the (111) direction.

The difference in form of the conduction and d-bands is reflected in the wave-functions. The conduction band states are plane-wave like - the associated charge density is almost constant throughout the crystal. The d-band states are generally well represented by a linear combination of atomic orbitals centred on each atom. A combined basis of plane waves and atomic orbitals has been used in parametrised interpolation

---

\*Spin-orbit splitting is negligible. Bands are also degenerate along certain directions of high symmetry.



## COPPER

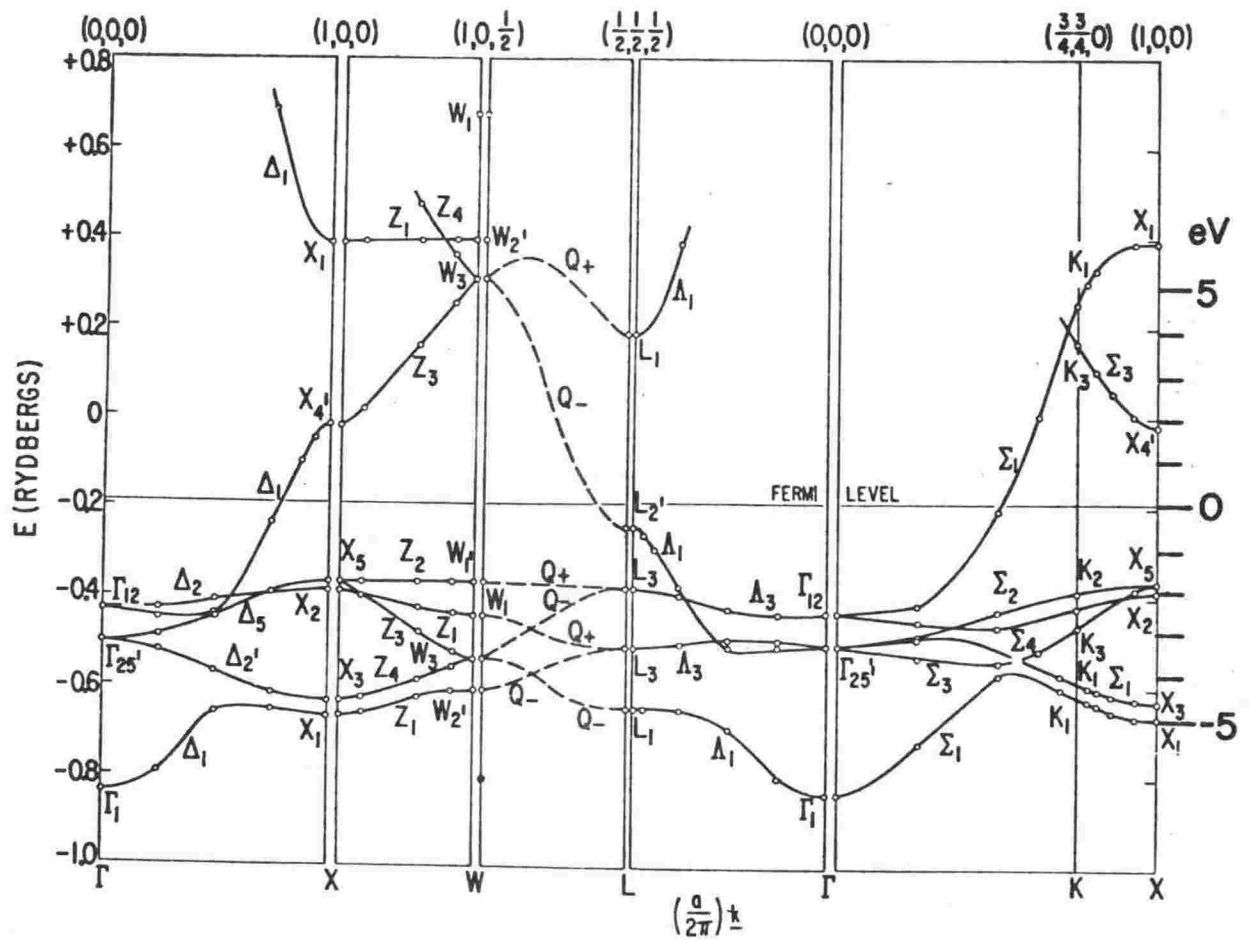


Fig.2.1 Brillouin zone for fcc crystal structure and band structure for copper calculated by Segall (1962).

band schemes (Slater and Koster, 1954; Hodges et al, 1966; Mueller, 1967; Smith and Matthiess, 1974) which successfully describe d-band metals. The width of the d-band in the limit of a narrow band is determined by overlap integrals like  $\langle \phi(\text{site } o) | V(\text{site } o) | \phi(\text{site } \underline{s}) \rangle$ . A single matrix element (Heine, 1967) describes well both the overall width and the hybridisation interaction with the conduction band.

The renormalised atom approach (Hodges, Watson & Ehrenreich, 1972) emphasises another aspect of the interaction between conduction and d states, and the connection between the band and atomic point of view. In constructing solid copper from free atoms one must compress the s and d electrons within the Wigner-Seitz sphere\* to ensure charge neutrality by, for instance, renormalising the atomic wavefunctions (fig.2.2). Because the s wavefunction is more extended than the d wavefunction the charge to be shifted by renormalisation is larger - about 0.6 s electrons compared with 0.2 d electrons. There are two effects on the atomic states apart from the broadening into bands (fig.2.2).

- (1) The energy of the atomic d state is raised by the electrostatic potential of the compressed s and d charge - by about 6 eV and 19 eV per unit increase of s and d charge respectively within the Wigner-Seitz sphere.
- (2) The kinetic energy of the conduction state at the bottom of the band is lowered relative to the atomic s state because the Wigner-Seitz boundary condition  $\frac{d\psi}{dr} = 0$  at  $r = r_s$  requires less curvature in the wavefunction.

Finally, for d-band states, the concept of a bond can be useful; for example, the three  $\Gamma_{25'}$  d states (transforming as xy, yz, zx) have maximum charge density between nearest-neighbour atoms, along the (110) directions, and so these orbitals are "bonding" compared to the anti-bonding

---

\*The Wigner-Seitz sphere (radius  $r_s = 2.67$  au in copper) has a volume equal to the volume per atom in the solid.

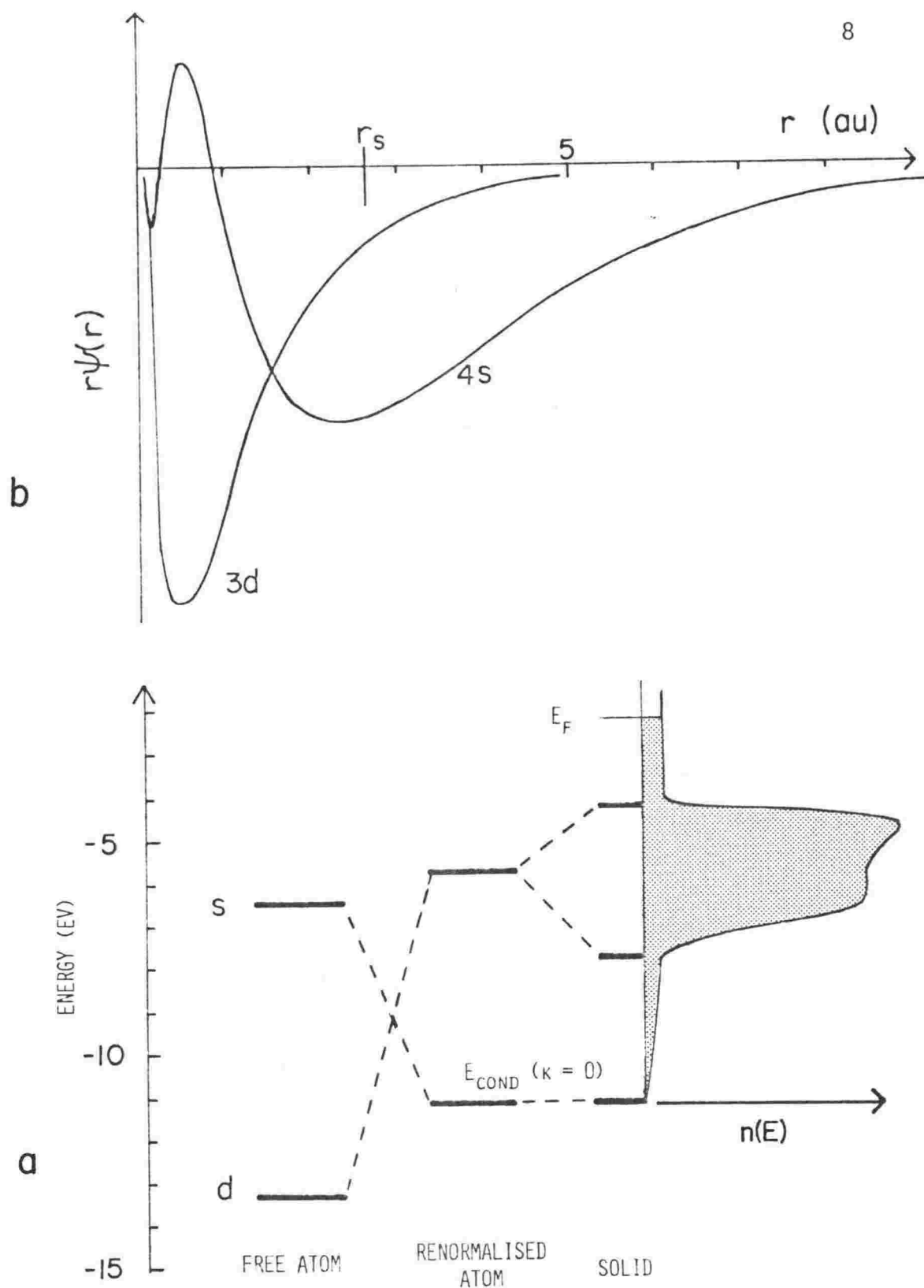


Fig.2.2 Renormalised atom viewpoint of electronic structure :  
 a) copper 3d and 4s atomic wavefunctions (Herman and Skillman, 1963)  
 b) renormalisation and band contributions to energy levels in solid copper (based on figure in Hodges et al (1972)).

next-nearest-neighbour directed  $\Gamma_{12}$  states.

## 2.2 Alloys

In this section we consider in turn some spatial aspects of impurity electronic structure, the implications for band structure theories of the lack of periodicity in a disordered alloy, and first order perturbations of the band structure, concluding with a mention of more sophisticated theoretical treatments.

### Screening

Substitution of an impurity for a host atom changes the ionic potential and introduces a local distortion of the lattice. Characteristically in metals there is an accompanying transfer of charge between the impurity and the host atoms in its vicinity. If the impurity ion has an excess valence  $Z$  relative to the host it will attract a screening cloud of electrons to neutralise its excess valence and maintain the electron distribution in equilibrium. A linearised Thomas-Fermi treatment (Friedel, 1954) gives a screening charge density

$$\Delta\rho(r) = \frac{Zq^2}{r} \exp(-qr)$$

where the screening length  $q^{-1} \sim 0.8$  au for copper. More exact treatments show the presence of long range Friedel oscillations in the charge density

$$\Delta\rho(r) \sim \frac{\cos 2K_F r}{r^3}.$$

Fig.2.3 compares the results of a many-body perturbation calculation by Langer and Vosko (1960) with the Thomas-Fermi approximation. Both agree that the screening is highly efficient. About 90% and 75% respectively of the screening charge is localised within the impurity site Wigner-Seitz sphere. The results of nuclear magnetic resonance quadrupole effect experiments on copper alloys (reviewed by Grüner and Minier, 1977) are in accord with long range oscillations in the charge density. However, the measured

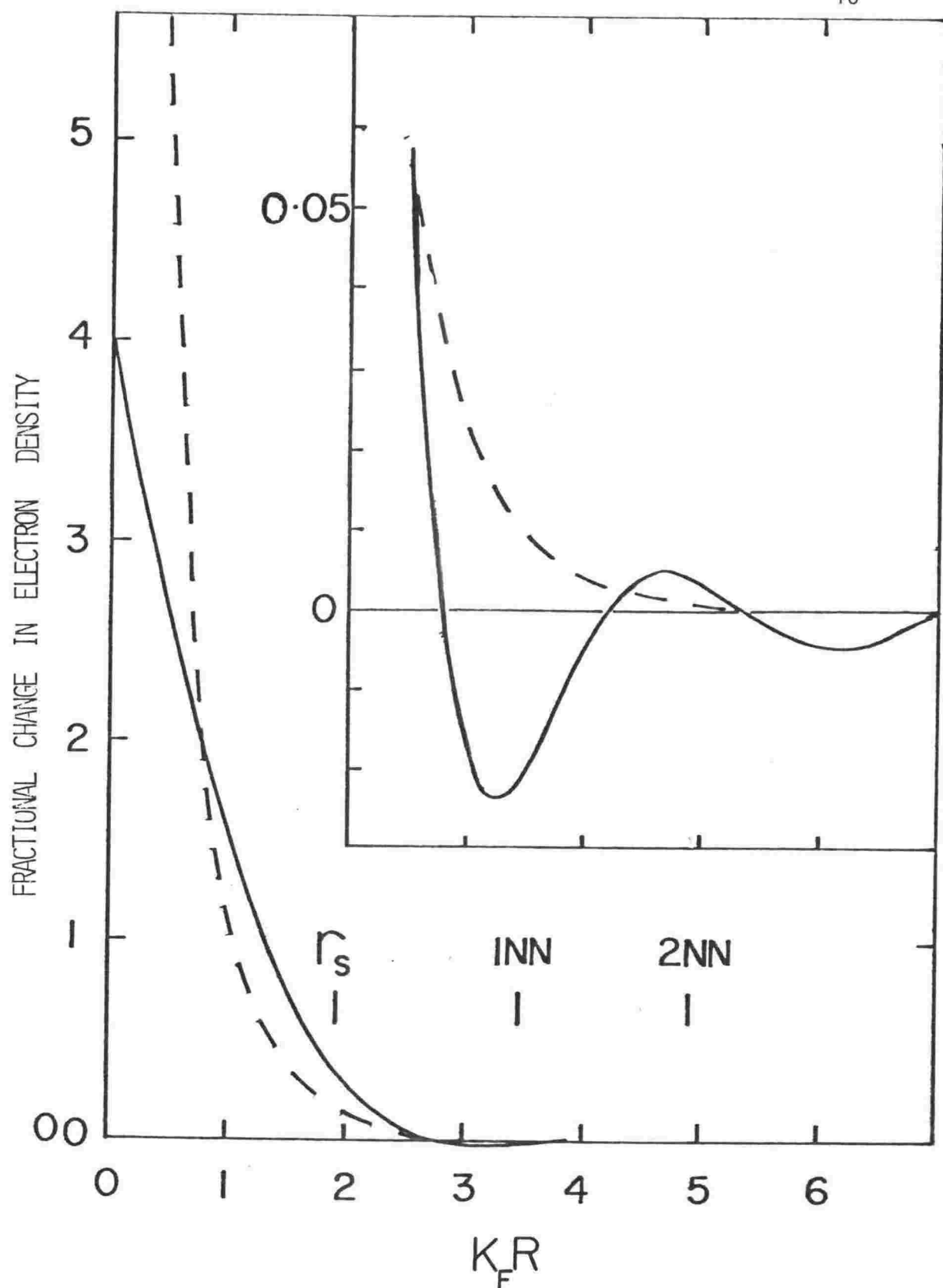


Fig.2.3 Charge density distribution surrounding a singly charged impurity in an electron gas with a Wigner-Seitz radius  $r_s$  of 3 au ( $r_s$  for Cu = 2.67 au). The result of Langer and Vosko (1960) (solid curve) is compared with the linearised Thomas-Fermi approximation result (dashed curve). The positions of the first and second nearest neighbours in Cu, and  $r_s$  are indicated.

electric field gradients at near neighbours are not well understood, being almost independent of impurity valence at the nearest neighbour rather than directly proportional. An exact treatment of valence, lattice distortion (Sagalyn & Alexander, 1977) and band structure effects seems to be required. The valence effect by itself predicts a charge density deficiency of several percent in the vicinity of the nearest neighbour of a singly charged impurity. Nuclear magnetic resonance Knight shift measurements (Rowland, 1962) on silver alloys are consistent with this, suggesting a decrease in S charge density proportional to the impurity valence. The possibility of  $\lambda$ -dependent charge exchange (Hodges, 1978) should not be discounted.

The extent of the screening charge distribution determines the absolute shift of the Fermi level. According to Stern (1976) the shift can be related to the electrostatic potential step due to charge transfer across the interface between a piece of pure metal and alloy (fig.2.4). This charge transfer is caused by the screening clouds overlapping the interface. The Fermi level is constant throughout the system but in the alloy the zero of the crystal potential (Ashcroft & Mermin, 1976, p.354) is shifted relative to the Fermi level due to the dipole layer at the interface. Friedel (1954) has pointed out that, with localised screening, in the low impurity concentration limit there are regions of the alloy with negligible perturbation of the charge density and potential, and hence the Fermi level of the alloy is unaffected:

$$\frac{dE_F}{dc} \rightarrow 0 \text{ as } c \rightarrow 0 .$$

This is important for the interpretation of optical spectra for dilute alloys. At finite concentrations the screening clouds overlap and the Fermi level is affected - the Thomas-Fermi approximation (Friedel, 1954) predicts



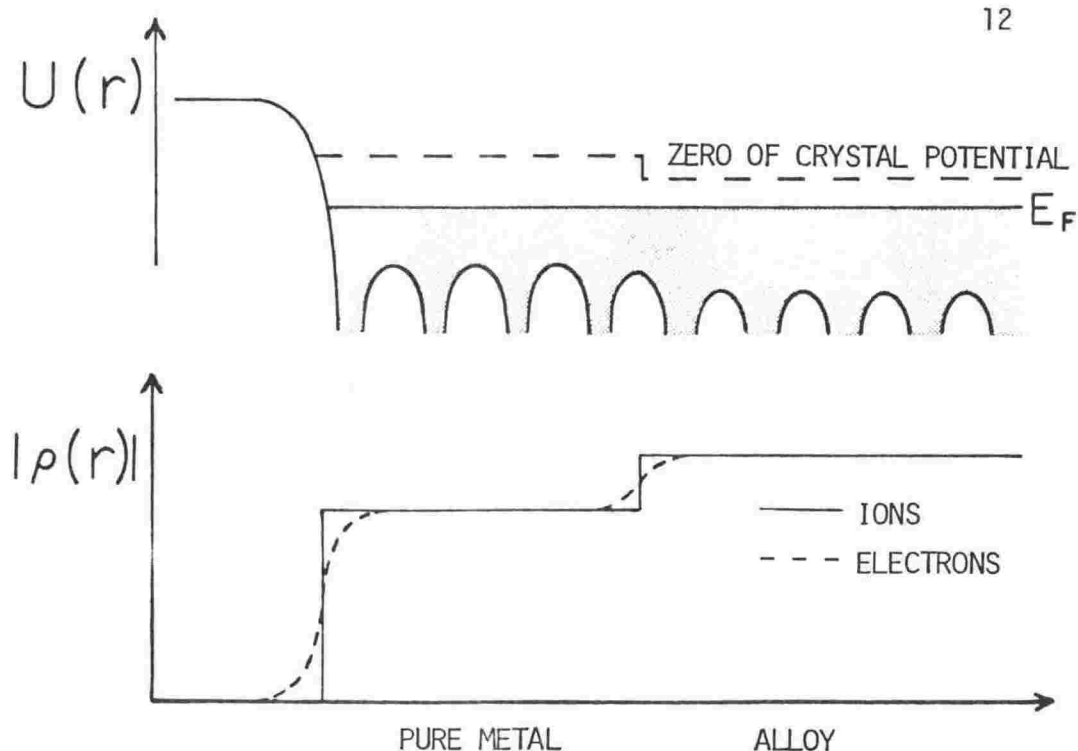


Fig.2.4 Charge transfer at the interface between pure metal and an alloy produces a dipole layer which shifts the zero of the crystal potential ( and hence the atomic energy levels ) relative to the Fermi levels.

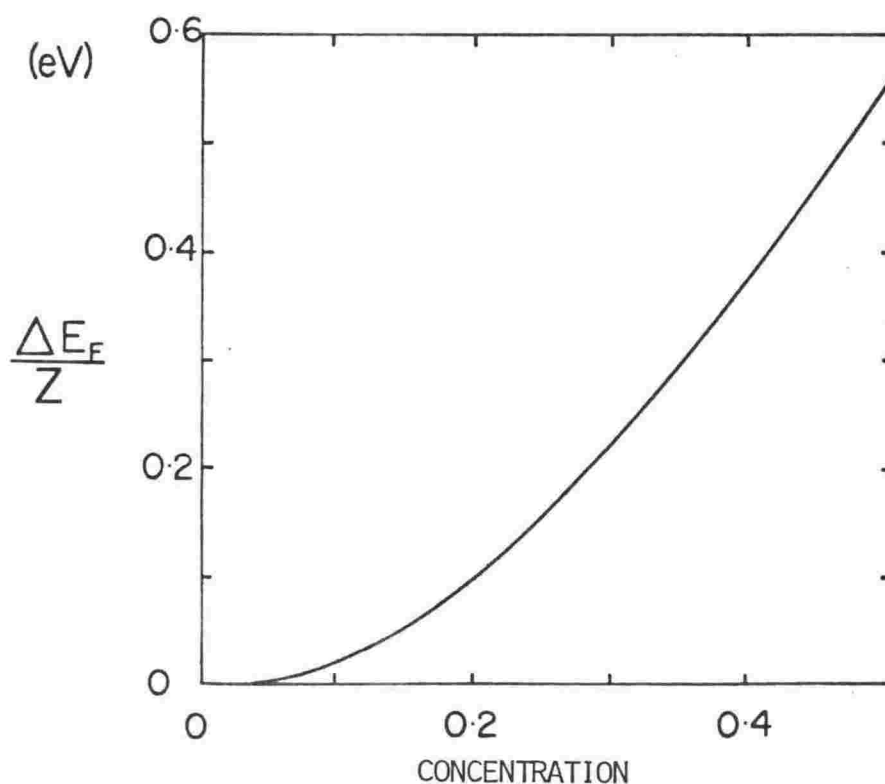


Fig.2.5 Change in the Fermi level per unit excess valence of impurity in copper according to the result of Friedel (1954) in the Thomas-Fermi approximation with  $q=1.1$ .

$$\Delta E_F = Zq/(qRCoshqR - SinhqR)$$

where  $R = r_s C^{-\frac{1}{3}}$ , (fig.2.5).

A more accurate treatment of screening should not qualitatively modify this dependence because the shift is dominated by the screening charge overlap around impurities which are nearest neighbours, where oscillations in the charge density overlap are not evident. The more localised many-body screening at nearest neighbours suggests that the Fermi level should rise less rapidly than the Thomas-Fermi prediction. Thus the variation in the Fermi level at finite concentrations can give information about the charge density close to an impurity complementary to that obtained from nuclear magnetic resonance experiments.

#### Localised states

If the impurity potential is sufficiently attractive (i.e.  $Z$  large and positive) it will split off a localised state from the bottom of the host conduction band (Koster & Slater, 1954). Zeller and Dederichs (1979), calculating the local density of states at impurity sites, find that Ga and Ge impurities in Cu have localised 4s states. This implies that the effective excess valence of the impurity will be reduced accordingly. In contradiction, the observed scaling of alloy phase boundaries with the ordinary excess valence (see Chapter 1) seems to preclude the subtraction of localised states from the conduction band up to at least  $Z = 4$ .

#### Band structure of alloys

The absence of perfect periodicity in disordered alloys calls into question the validity of  $k$  as a quantum number. According to Stern (1968), the eigenstate in the pure metal is transformed in a dilute alloy to an alloy eigenstate with energy  $E$ , comprising a coherent part with a complex wavevector  $K$  and an incoherent part - a mixture of waves with a range of wavevectors - associated with the screening distribution, as depicted in fig.2.6.

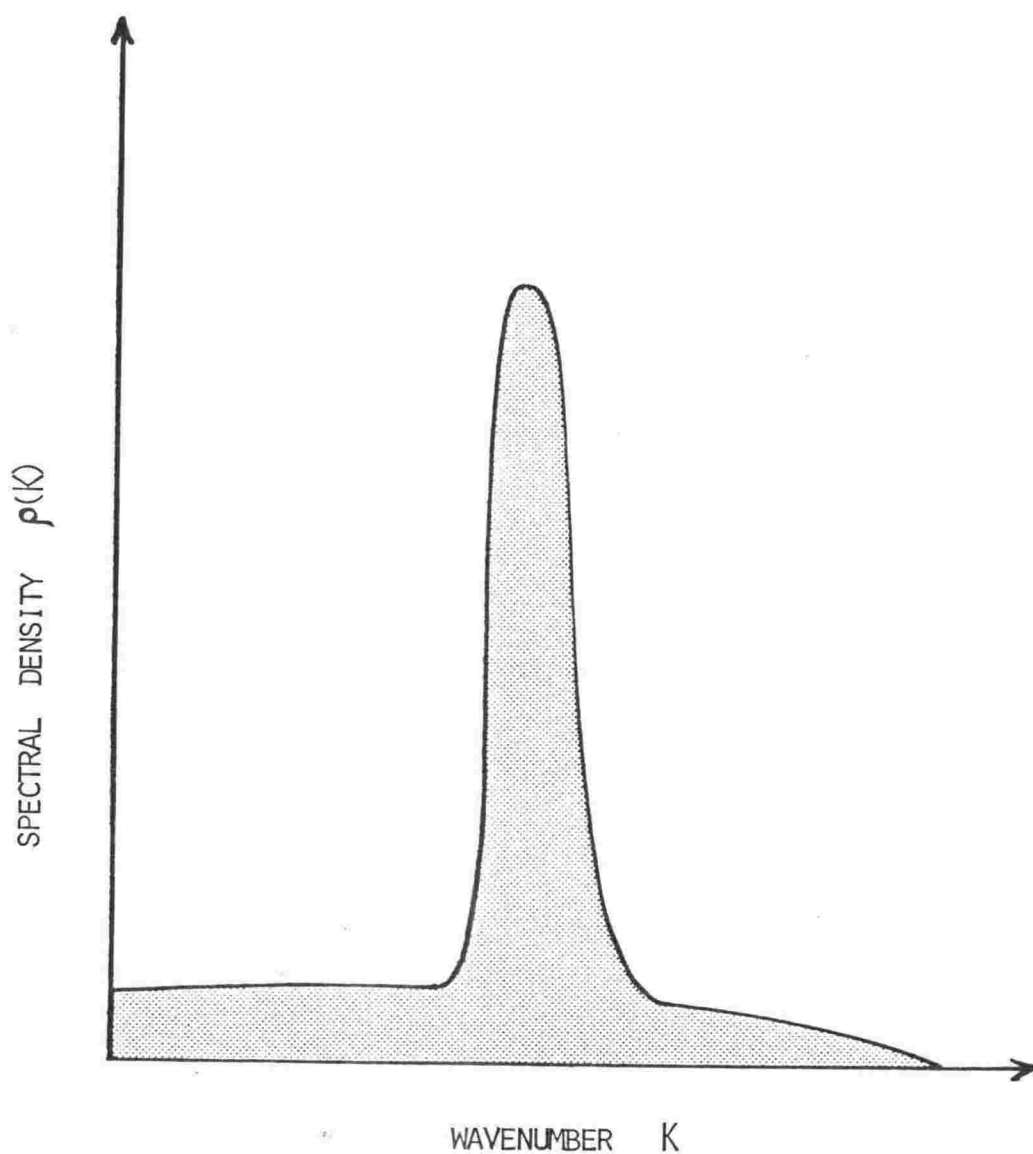


Fig.2.6 Distribution of wavenumber in an eigenstate of a dilute alloy. The width of the peak and the height of the broad incoherent background are proportional to the strength of scattering of eigenstates of the pure material from the impurity.

The width of the coherent peak and the height of the broad background distribution are proportional to the impurity concentration. The coherent part of the wavefunction is renormalised because the background subtracts some weight from the area under the peak.

A correspondence exists between the alloy eigenstates and band states with wavevector  $k$  and complex energy  $E + iE'$ , which implies their decay by scattering since they are not eigenstates of the alloy. The coherent alloy wavevector and band wavevector are related by

$$k^2 = K^2 + \frac{4\pi n c}{k} \sum_{\ell} (2\ell + 1) (\phi_{\ell} - \exp(i\phi_{\ell}) \sin \phi_{\ell})$$

where  $\phi_{\ell}$  is the phase shift for the  $\ell$ th partial wave scattering from the impurity potential, satisfying the Friedel sum rule (Friedel, 1954)

$$Z = \frac{2}{\pi} \sum_{\ell} (2\ell + 1) \phi_{\ell}(E_F) .$$

Stern thus maintains that the concept of an alloy band structure, related as described above to the actual alloy electronic structure, remains valid as long as  $E'/\Delta E \ll 1$  for the states considered, where  $\Delta E$  is the change in the energy of the band state on alloying.  $\frac{E'}{\Delta E}$  is roughly proportional to  $Z$  and is estimated to be  $\sim 1$  at the Fermi level for  $Z = 4$  impurities in Ag (Stern, 1973).

#### Perturbations of the band structure

The first order perturbation to the energy of the pure metal eigenstate  $\psi_{n\underline{k}} = u_{n\underline{k}}(\underline{r})e^{i\underline{k} \cdot \underline{r}}$  is given by

$$\Delta E = \int \psi_{n\underline{k}}^* V_p(\underline{r}) \psi_{n\underline{k}} d\tau$$

where  $V_p(\underline{r})$  is the perturbing potential - the difference between the alloy and pure metal crystal potentials - which is highly localised on impurity sites by screening. (Furthermore, according to Stern (1966) it is too strong for perturbation theory to be strictly valid unless the

excess valence of the impurity is less than the valence of the host.)

In the rigid band approximation (Mott & Jones, 1936) this shift is assumed to be a constant independent of wavevector or band (indexed by  $n$ ). The Fermi surface must expand to accommodate the  $cZ$  additional conduction electrons per atom introduced by the impurities - a fundamental requirement which might be termed "filling of states" - so that the host band structure is rigidly shifted with respect to the Fermi level by

$$\delta E = -\frac{cZ}{n_0(E_F)}$$

as shown in fig.2.7.\*

The approximation is restricted to weak impurity potentials, low concentrations, and free-electron-like bands - in dilute copper-based alloys some failings are obvious, for instance the observed almost constant position of the  $d$  bands relative to the Fermi level. However, if account is taken of the variation of the spatial character of the wavefunction with wavevector and band the perturbation approach provides at least a qualitatively correct description of the effects of alloying as follows. Since  $V_p(\underline{r})$  is localised on impurity sites, eigenstates of the pure metal which have large amplitude on such sites will be most affected. Obviously the compact Cu  $d$  wavefunctions, which only slightly overlap neighbouring sites, will be shifted in energy much less than the conduction band states,

---

\*The pure host density of states at the Fermi level,  $n_0(E_F)$ , can be estimated from specific heat data. Using data given by Lengeler et al (1977) and including a 12% correction for electron-phonon enhancement  $n_0(E_F)$  for copper is estimated to be  $0.262 \text{ eV}^{-1}$  per atom. Band structure calculations (e.g. Dalton, 1970) are in good agreement.

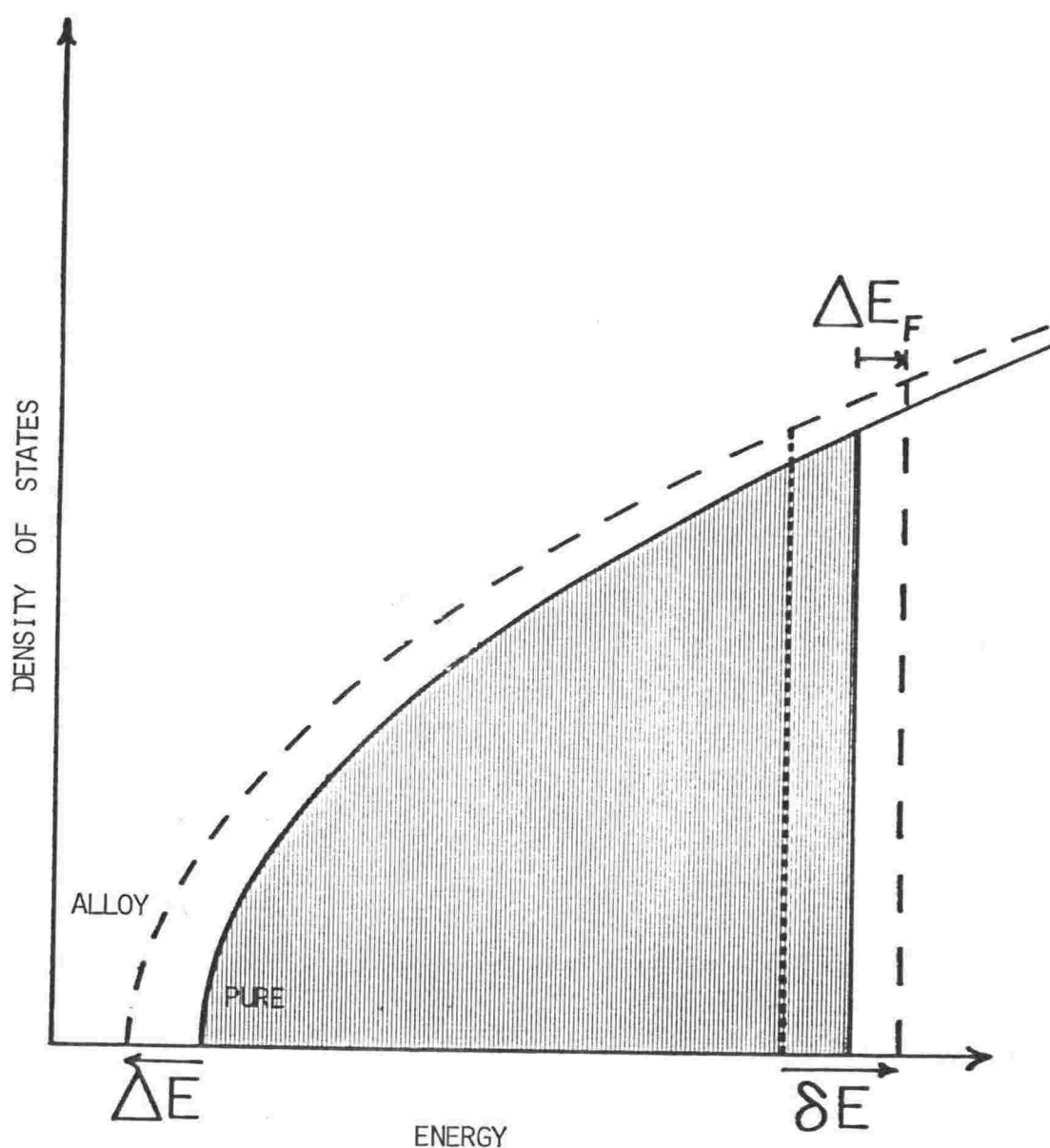


Fig.2.7 Rigid band shifts in a free-electron metal alloy.

The density of states of the pure metal (solid curve-- the occupied states are shown by hatching) shifts with no change in shape on alloying (dashed curve). If the electron per atom ratio were unchanged ( $Z=0$ ) the Fermi level would shift by the same amount  $\Delta E$ ; but to accommodate extra states it must rise relative to the density of states by  $\delta E = cZ/n_0(E_F)$ .

which have nearly uniform spatial density and sample the potential throughout the crystal. Within the d bands, bonding states (e.g.  $\Gamma_{25'}$ ) should be more affected than antibonding states because they are more extended. In the conduction band, bonding states (e.g.  $\Gamma_1$  and the states of the bottom of the band gaps:  $X_4'$  and  $L_2'$ ) should be less perturbed than antibonding states ( $X_1$ ,  $L_1$ ) because the former have large amplitudes between atoms and the latter have large amplitudes on the atoms, including impurity sites. Also, p-like states (near the Fermi surface neck in copper (Segall, 1962)) should be less affected than S-like states (around the Fermi surface belly) because they have lesser amplitude at impurity nuclei. Nevertheless, changes in the shape of the conduction band should be small; the calculations of Bansil et al (1974) show that lattice expansion on alloying causes a larger distortion of the conduction band.

The distinction made by Stern between alloy eigenstates and band states has little-appreciated implications for the filling-of-states aspect of the rigid band model. The fractional volume increase of the Fermi surface per unit impurity concentration in the dilute limit differs from the impurity valence  $Z$  by (Coleridge, 1979)

$$Z - \frac{\Delta V}{V} = \frac{2}{\pi} \sum_{\ell} (2\ell + 1) (\phi_{\ell} - \sin \phi_{\ell} \cos \phi_{\ell})$$

because only the coherent part of the alloy wavefunction contributes to the Fermi surface. It is easily shown that this Fermi surface volume defect is a minimum when

$$\phi_{\ell} = \frac{\pi Z}{18}.$$

(Phase shifts for  $\ell > 2$  are assumed to be negligible.) The table below gives the minimum possible defect for different  $Z$ .

Z:	1	2	3	4
Minimum Fermi surface volume defect (%)	1	8	17	29

A discrepancy of approximately 10% between  $\frac{\Delta v}{v}$  and Z found in de Hass-van Alphen effect measurements on Cu(Al) and Au(Ga) (Coleridge, 1979) was attributed to this effect, which reflects the fact that  $k$  is no longer a good quantum number in a disordered alloy.

#### Modern alloy theories

Alloy theories more sophisticated than the rigid band model have been devised; the virtual crystal approximation, the average  $t$ -matrix approximation, and the coherent potential approximation, all of which use band structure techniques on an effective medium with a periodic potential. The field has been reviewed by Ehrenreich and Schwartz (1976). Calculations on polyvalent solutes in the noble metals, relevant to this experimental work, have been confined to Cu-Zn - the most realistic calculation to date is the average  $t$ -matrix band structure by Bansil et al (1974). Even this work makes an empirical adjustment of charge transfer to obtain agreement with the interband threshold for optical absorption. Any complete alloy band structure theory should give complex eigenvalues and self-consistently determine the impurity potential, screening, and local deformation of the lattice. Progress in calculating a self-consistent impurity potential and local density of states within an impurity muffin-tin cell has been reported recently (Zeller & Dederichs, 1979), one awaits a fully self-consistent band structure calculation.

### 2.3 Optical Properties

#### Macroscopic description

The optical properties of a non-magnetic material medium in the absence of spatial dispersion can be described by a frequency-dependent dielectric constant.

$$\epsilon(\omega) \equiv \epsilon_1 + i\epsilon_2$$



is a complex, symmetric, second-rank tensor, reducing to a scalar for crystals of cubic symmetry such as copper which are optically isotropic. Attention is usually focused on  $\epsilon_2$ ; the classical result that the rate of energy absorption per unit volume from an electric field is given by

$$\omega \epsilon_2 |E|^2 / 4\pi$$

suggests its direct connection with elementary excitations in the medium. The real and imaginary part of the dielectric function are not independent; because of the response-function character of  $\epsilon$  they are connected by the Kramers-Kronig dispersion relations:

$$\epsilon_1(\omega) = 1 + \frac{2}{\pi} P \int_0^\infty \frac{\omega' \epsilon_2(\omega')}{(\omega')^2 - \omega^2} d\omega'$$

$$\epsilon_2(\omega) = - \frac{2}{\pi} P \int_0^\infty \frac{\epsilon_1(\omega')}{(\omega')^2 - \omega^2} d\omega'$$

(P denotes the principle part of the integral. A complete treatment may be found in, for example, Hodgson (1970) or Wooten (1972).) Thus if  $\epsilon_2$  is known throughout the entire spectrum,  $\epsilon_1$  can be deduced, and vice versa.

To obtain  $\epsilon(\omega)$  from reflectivity (R) measurements one makes use of analogous dispersion relations for the complex reflection coefficient for normal incidence  $r = \sqrt{R} e^{i\theta}$ . Specifically:

$$\theta(\omega) = \frac{1}{2\pi} \int_0^\infty \frac{d}{d\omega'} (\ln R(\omega')) \ln \left( \frac{\omega' + \omega}{\omega' - \omega} \right) d\omega'$$

and then  $\epsilon_1$  and  $\epsilon_2$  are given algebraically by:

$$\epsilon_1 = n^2 - k^2, \quad \epsilon_2 = 2nk$$

$$n = \frac{1 - R}{1 + R - 2\sqrt{R}\cos\theta}, \quad k = (n + 1) \frac{\sqrt{R}\sin\theta}{(\sqrt{R}\cos\theta - 1)}.$$

Experimental methods not utilising the dispersion relations (and thereby avoiding extrapolations outside the necessarily limited range of measurement) must involve two independent

optical measurements at each wavelength in order to specify the complex pair of optical constants.

### Microscopic description

The types of one-electron optical transitions which may occur in metals are shown in fig.2.8. Since optical photons have negligible momentum on the scale of the Brillouin zone, only vertical (or direct) interband transitions are allowed unless momentum conservation is satisfied, as it is for intraband and non-vertical (indirect) interband transitions, by interaction with phonons or crystal defects.

### Intraband transitions

Intraband absorption is described by the Drude free-electron theory which gives

$$\epsilon_2^f = \frac{\omega_p^2 \tau}{\omega(1 + \omega^2 \tau^2)}$$

where  $\omega_p$  is the plasma frequency and  $\tau$  the relaxation time characterising the scattering mechanisms necessary for a free electron to absorb energy from an electromagnetic field. For copper  $\hbar\omega_p = 9.0$  eV and  $\hbar/\tau \approx 0.04$  eV at room temperature. In the far infra-red  $\epsilon_2^f$  diverges as  $\omega^{-1}$ ; for  $\omega \gg \tau^{-1}$  it approaches zero as  $\omega^{-3}$  - in copper at the onset of interband transitions at 2 eV, it is small (see fig.2.11) and is easily subtracted.

Direct interband transitions from occupied states in lower band ( $\ell$ ) to vacant states in an upper band ( $u$ ) are described by:

$$\epsilon_2^i = \frac{1}{\pi} \left( \frac{e\hbar}{m\omega} \right)^2 \sum_{u\ell} \int_{\text{Brillouin zone}} d^3k |\hat{n} \cdot \underline{p}_{u\ell}|^2 \delta(E_u - E_\ell - \hbar\omega) f(E_{k\ell}) (1 - f(E_{ku}))$$

The integral simply counts all pairs of states in the Brillouin zone subject to the conditions: on their occupancy - given by the Fermi distribution functions, energy conservation as stipulated by the  $\delta$ -function, and  $\underline{k}$  conservation implicit in the notation, weighting them according to the transition probability given by the matrix element,

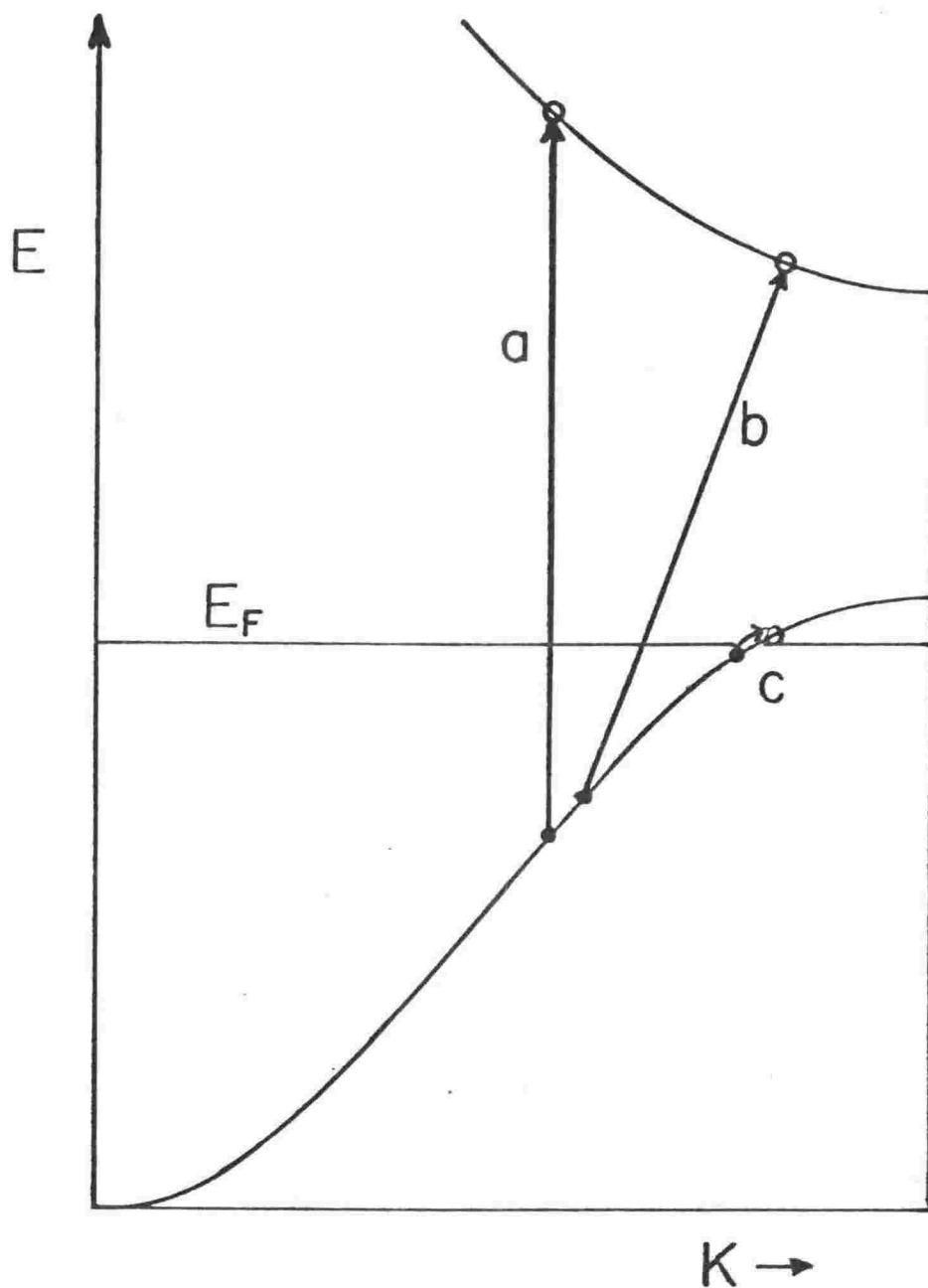


Fig.2.8 Examples of single electron optical transitions in metals : a) direct interband , b) indirect interband, c) intraband transitions. Transitions b) and c) require interactions with some form of defect.

$$\underline{P}_{u\ell}(\underline{k}) = \int \psi_{\underline{k}u}^* \nabla \psi_{\underline{k}\ell} d\tau,$$

$\underline{\hat{n}}$  is the electric field unit vector.

Considering a single band pair and assuming the matrix element is constant throughout  $\underline{k}$  space (or at least slowly varying in the region of interest):

$$\epsilon_2^{u\ell} = \left(\frac{2\pi e\hbar}{m\omega}\right)^2 |\underline{\hat{n}} \cdot \underline{P}_{u\ell}|^2 J_{u\ell}(\omega)$$

where the (partial) joint density of states is

$$J_{u\ell}(\omega) = \frac{2}{(2\pi)^3} \int d^3k \delta(E_u - E_\ell - \hbar\omega) f(E_\ell)(1 - f(E_u))$$

which alone determines the frequency variation of the interband contribution to  $(\hbar\omega)^2 \epsilon_2$ .

#### Critical points

The expression above can be transformed to an integral over surfaces of equal energy difference,  $\hbar\omega_{u\ell} = E_u - E_\ell$ ;

$$J_{u\ell}(\omega) = \frac{2}{(2\pi)^3} \omega_{u\ell} \int \frac{dS_{u\ell}}{|\nabla_k \omega_{u\ell}|} f(E_\ell)(1 - f(E_u))$$

showing that, when  $\nabla_k \omega_{u\ell} = 0$ ,  $P_{u\ell}$  will exhibit strong variation. These critical points are the Van Hove singularities. Generally they occur where two bands are parallel and level, ( $\nabla_k E_u = \nabla_k E_\ell = 0$ ), and can be predicted from symmetry, since at the boundary and centre of the B.Z., for instance, all bands must be level. To a first approximation the bands near the critical point are parabolic and the form of the critical point is determined by whether the band separation has a local maximum, minimum, or saddle point as summarised in table 2.1. At a critical point  $J_{u\ell}(\omega)$  has the form  $\pm[\pm(\omega - \omega_0)]^{1/2}$ .

A further source of structure in  $\epsilon_2$  is the truncation of  $J_{u\ell}$  by the discontinuity between occupied and vacant states at the Fermi level in metals. The threshold is especially abrupt when the onset of transitions occurs along a line on the Fermi surface rather than

Table 2.1      Properties of Van Hove singularities  
in the joint density of states .

In the vicinity of a critical point at  $\underline{k}_c$  the energy gap between upper and lower bands has the expansion

$$\omega_{ul} = \omega_c + \sum_{i=1}^3 a_i (k_i - k_{ci})^2$$

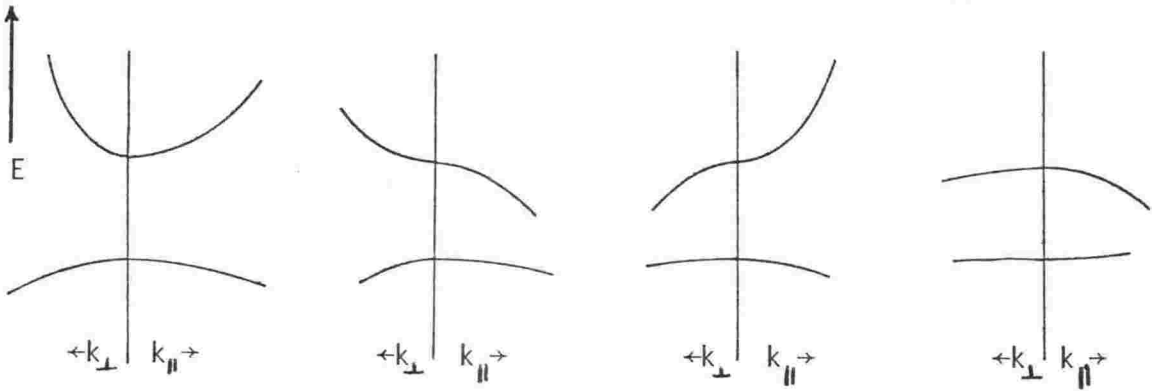
where 
$$a_i = \frac{\hbar}{2m_i} \quad \frac{1}{m_i} = \frac{1}{m_i^u} + \frac{1}{m_i^l} = \frac{d^2\omega_u}{dk_i^2} + \frac{d^2\omega_l}{dk_i^2}$$

Four types of critical point behaviour result:

Sign of the  $a_i$ :

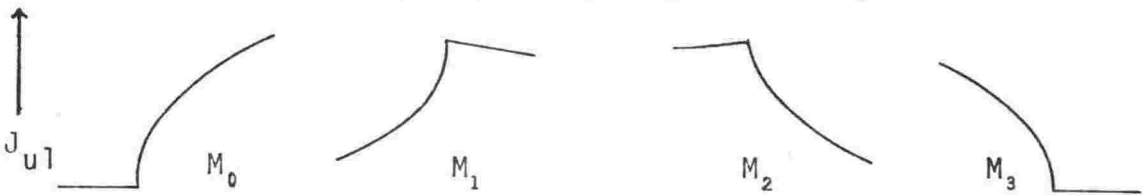
all +                      two+                      one +                      all -

Corresponding form of the band structure about  $\underline{k}_c$ :



( $k_{||}$  = direction of centre of B.Z.,  $k_{\perp}$  = two equivalent transverse directions)

Corresponding singularity in joint density of states:



at a point (Cooper et al, 1965), producing a Fermi surface singularity with  $(\omega - \omega_0)^{1/2}$  dependence which is like an  $M_0$  Van Hove singularity. A number of singularities occurring in copper in the 2-6 eV region are marked on the band structure detail of fig.2.9. The critical points are:

d band  $\rightarrow$  conduction band transitions

- a)  $E_d^U(L_3^U) \rightarrow E_F$ , the d band threshold - a Fermi surface singularity with transitions initially localised around the Fermi surface neck near L but spreading all over the Fermi surface for energies only a little above threshold because of the flatness of the upper d-band. A similar threshold occurs for transitions from the bottom of the d bands.

- b)  $X_5 \rightarrow X_4'$ ,  $M_1$  Van Hove singularity.

conduction band  $\rightarrow$  conduction band transitions

- c)  $E_F \rightarrow Q_+(L_1^U)$ , the interconduction band threshold: a Fermi surface singularity around the neck.
- d)  $L_2' \rightarrow L_1$ ,  $M_2$  Van Hove singularity.

The contribution of individual band pairs to  $\epsilon_2$  according to the 2-parameter band structure calculation of Janak et al (1975) is shown in fig.2.10 compared to a typical experimental spectrum. The critical point structure in the experimental  $\epsilon_2$  spectrum is not dramatic, and broadening and overlap makes it less so in alloys. However, any perturbation of the band structure produces a large change in the joint density of states in the vicinity of a critical point, as discussed in the following section. This provides the motivation for the use of modulation spectroscopy and explains the importance of critical points in this context.

Indirect transitions

These are transitions in which the  $k$ -vector of the initial and final states can differ because momentum conservation is satisfied by scattering from a phonon, impurity, or defect. Fig.2.11 illustrates such transitions in a context relevant to copper. While direct

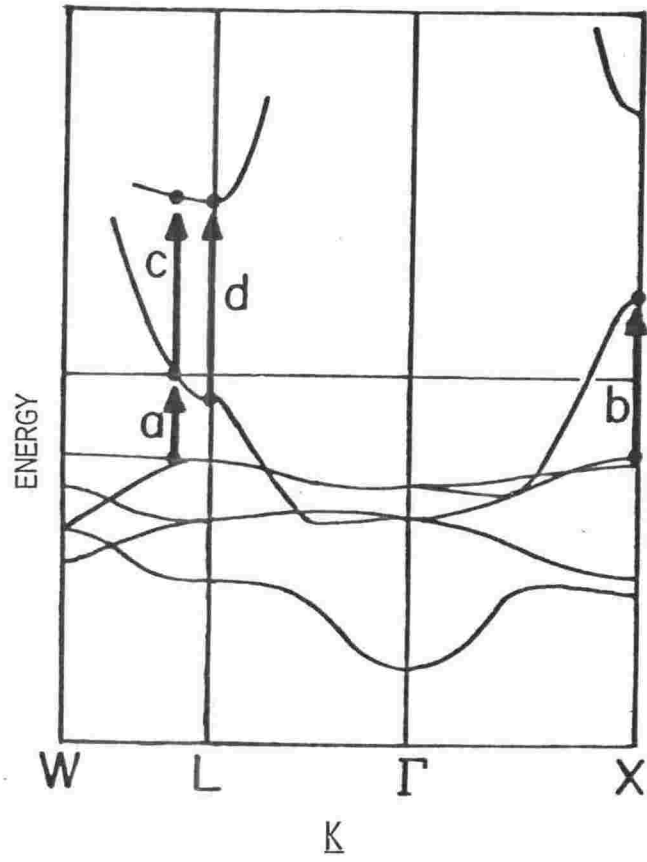


Fig.2.9 Important critical point transitions in copper:

- a)  $E_d^U(L_3) \rightarrow E_F$  d band threshold
- b)  $X_5 \rightarrow X_4'$
- c)  $E_F \rightarrow Q_+(L_1^U)$  interconduction band threshold
- d)  $L_2' \rightarrow L_1^U$

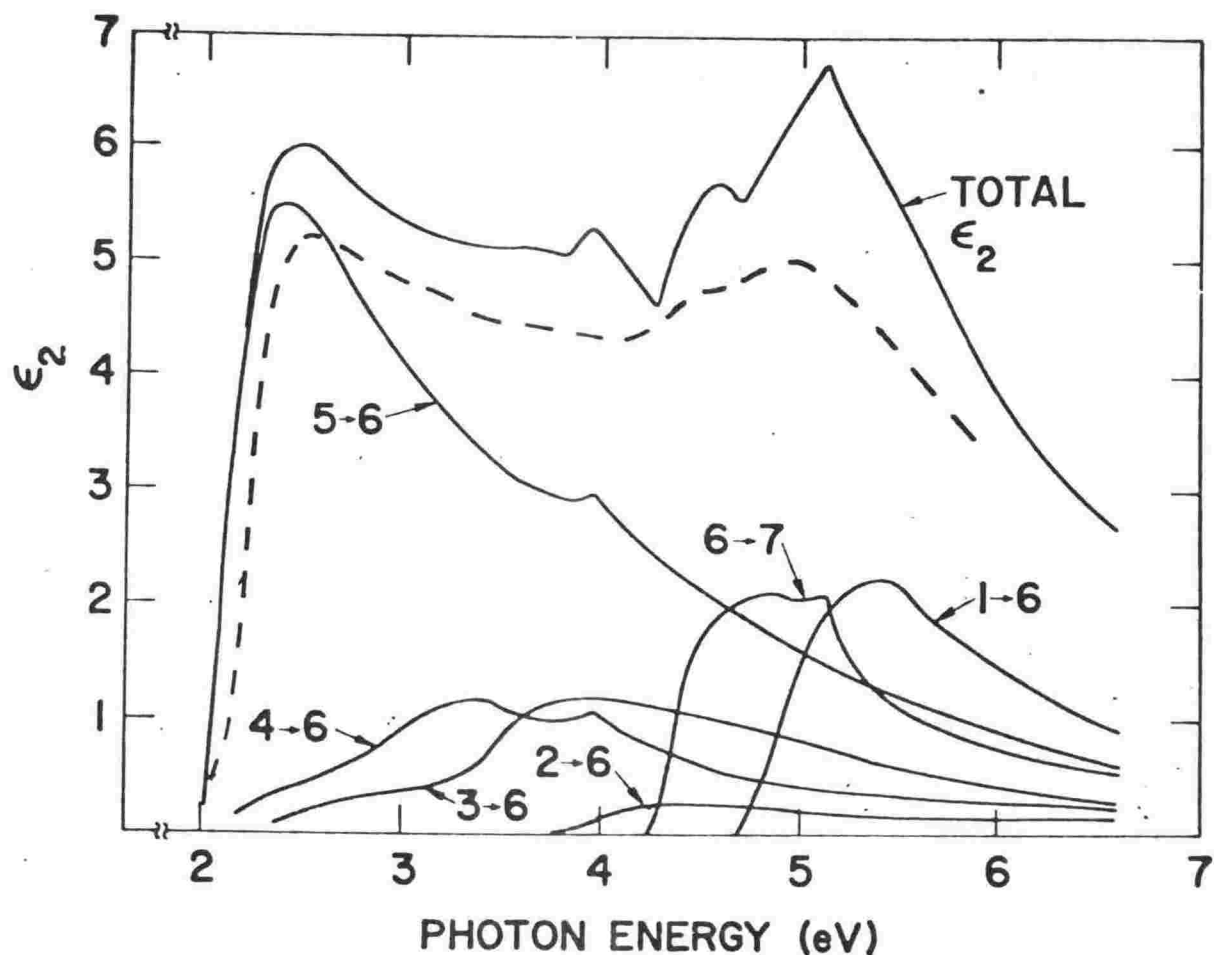


Fig.2.10 Interband  $\epsilon_2$  spectra for copper: experimental result from present study (dashed line) compared with theoretical result of Janak et al (1975) showing contributions from each pair of bands.



transitions set in with a  $(\omega - \omega_d)^{\frac{1}{2}}$  dependence, indirect transitions from the Fermi level to a band minimum go as  $(\omega - \omega_i)^{\frac{3}{2}}$ . Phonon assisted indirect transitions have been studied in semiconductors (Harbeke, 1972) where their effect, two or three orders of magnitude weaker than direct transitions, is often apparent below the direct gap. In pure metals there is no definite evidence of indirect transitions - intraband absorption easily masks weak structure - and, given the success of the direct transition model (fig.2.10), it is unlikely they are significant. In copper-based alloys, it has been suggested (De Reggi and Rea, 1973) that, at a critical impurity concentration, the indirect threshold quite abruptly supplants the direct interconduction band threshold which lies about 0.3 eV higher in energy (fig.2.11). Since the subtle changes in  $\epsilon_2$  involved might otherwise be attributed to overlapping background absorption or non-linear charges in band gaps, the point has some bearing on the accuracy of determination of alloy band gaps.

Indirect transitions involve a direct virtual transition followed by scattering to the final state (Bassani & Parravicini, 1975). Assuming that the matrix element for direct transitions from the Fermi surface to band 7\* is constant throughout the Brillouin zone one can show

$$\omega^2 \epsilon_2^{6 \rightarrow 7}(\text{indirect}) = A c \left( \frac{V_{kk'}}{\Delta E} \right)^2 J_i$$

compared with

$$\omega^2 \epsilon_2^{6 \rightarrow 7}(\text{direct}) = A J_d$$

where  $J_i$  and  $J_d$  are the indirect and direct joint density of states and the scattering matrix element

$$V_{kk'} \approx \frac{Z}{n(E_F)} \approx 4Z \text{ eV}$$

---

\*The bands are labelled in order of increasing energy as for fig.2.10.

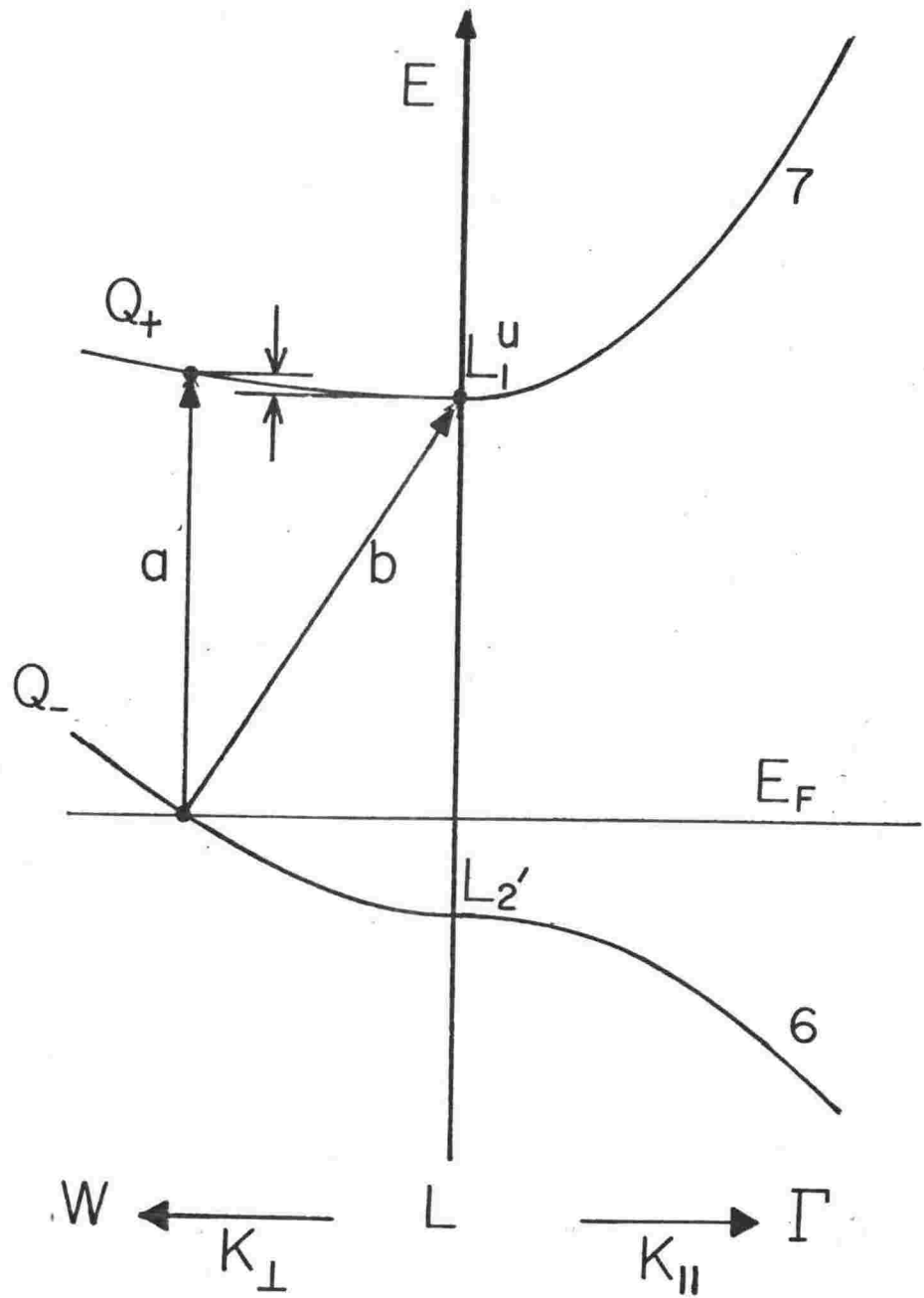


Fig.2.11 Direct and indirect thresholds for interconduction band transitions near L.

a) Direct transition threshold at energy  $Q_+(L_1^u) - E_F$

b) Indirect transition threshold  $L_1^u - E_F$

The difference in energy of the final states is

$$Q_+ - L_1^u = (E_F - L_2') m_u / m_l$$

in copper (Ziman, 1960). (Note that the concentration is incorrectly included in the matrix element in Ziman's calculation.)  $\Delta E$  is the difference in energy between the final state and the intermediate virtual state - inspection of band structure diagrams show that band 7 states are not more than 4 eV above  $L_1$  anywhere on the Fermi surface - thus the bracketed factor is of order unity (or greater) even for  $Z = 1$ . An estimate of the relative strengths of direct and indirect transition can be made as follows. Assuming for argument's sake that  $\Delta E \sim 4$  eV and neglecting common factors in the indirect and direct joint densities of states, one obtains

$$\omega^2 \epsilon_2(\text{indirect}) \sim \frac{2}{3} m_i^{\frac{3}{2}} n(E_F) (\hbar\omega - E_i)^{\frac{3}{2}} c Z^2$$

$$\omega^2 \epsilon_2(\text{direct}) \sim m_d^{\frac{3}{2}} (\hbar\omega - E_d)^{\frac{1}{2}}$$

where the effective masses, using the notation of Cooper et al (1965) and masses obtained from band structure calculations (Janak et al, 1975), are

$$m_i^{\frac{3}{2}} = m_{\perp u} m_{\parallel u}^{\frac{1}{2}} \sim 1.8 m_0^{\frac{3}{2}}, m_d^{\frac{3}{2}} = \left( \frac{1}{m_{\perp l}} - \frac{1}{m_{\perp u}} \right)^{-1} \left( \frac{1}{m_{\parallel l}} + \frac{1}{m_{\parallel u}} \right)^{\frac{1}{2}} \sim 0.15 m_0^{\frac{3}{2}}.$$

The indirect contribution will exceed the direct contribution at all energies when

$$C > (\sqrt{3} \left( \frac{m_i}{m_d} \right)^{\frac{3}{2}} n(E_F) (E_d - E_i) Z^2)^{-1}$$

which, for  $E_d - E_i = 0.2$  eV,  $n(E_F) = 0.26$  eV<sup>-1</sup> atom<sup>-1</sup>, corresponds to about 10 at% for  $Z = 3$ , 23 at% for  $Z = 2$ , 93 at% for  $Z = 1$ . This rough calculation shows at least that indirect transitions could well produce significant absorption in substitutional alloys.

## 2.4 Strain-Optic Response

### Macroscopic description

The effect of strain on the optical properties of materials is described by a complex fourth rank piezo-optic tensor  $W$  defined by:

$$\Delta \epsilon_{ij} = W_{ijkl} e_{kl}.$$

Much of the following discussion refers implicitly to only the imaginary part of  $W_{ijkl}$ .

Thermodynamics and crystal symmetry reduce the number of independent components so that, in analogy to the generalised Hooke's law (Nye, 1957), the tensor can be reduced to a  $6 \times 6$  matrix relating two pseudo-vectors, with only three independent  $W_{ijkl}$  in the case of copper and other materials of cubic symmetry. The pseudotensor then has the form:

$$W_{ij} = \begin{pmatrix} W_{11} & W_{12} & W_{12} & & & \\ W_{12} & W_{11} & W_{12} & & & \\ W_{12} & W_{12} & W_{11} & & & \\ & & & W_{44} & & \\ & & & & W_{44} & \\ & & & & & W_{44} \end{pmatrix}$$

with zeroes in all unspecified components.

With the proper choice of strain directions and crystal faces (Garfinkel et al, 1966) optical measurements with polarised light on single crystals will yield these piezo-optic "constants".

The combination of crystal symmetry and strain symmetry gives rise to selection rules which, for shear strain of particular symmetry, require that there is no shift in energy (apart from splitting of orbital and spin degeneracies), and hence no piezo-optic response from states along certain directions in  $k$ -space. A tetragonal shear strain does not affect the degeneracy of the body diagonals of a cube and thus does not perturb states with  $\underline{k}$  directed along  $L$ . Likewise face centres and states along  $X$  are unaffected by trigonal strain. Table 2.2 summarises the selection rules and tensor definitions.

#### Microscopic description

The intraband response is mainly of interest as a guide to the extrapolation of piezoreflectance data in the infrared. For  $\frac{1}{\tau} \ll \omega \ll \omega_p$  (effectively from  $\sim 0.05$  eV to the interband threshold) the absorption due to intraband transitions is  $1 - R \sim \frac{2}{\omega p \tau} \ll 1$  so

Table 2.2      Piezo-optic tensor definitions  
and selection rules.

<u>Type of strain</u>	<u>Strain tensor</u>	<u>Corresponding piezo-optic components</u>
Hydrostatic	$\begin{pmatrix} 1 & 0 & 0 \\ 0 & 1 & 0 \\ 0 & 0 & 1 \end{pmatrix} e/3$	$W_{\text{hyd}} = W_{11} + 2W_{12}$
Trigonal	$\begin{pmatrix} 0 & 1 & 1 \\ 1 & 0 & 1 \\ 1 & 1 & 0 \end{pmatrix} e_{yz}$	$W_{\text{trig}} = W_{44}$
Tetragonal	$\begin{pmatrix} -\frac{1}{2} & 0 & 0 \\ 0 & -\frac{1}{2} & 0 \\ 0 & 0 & 1 \end{pmatrix} e_{zz}$	$W_{\text{tet}} = W_{11} - W_{12}$

Symmetry rules

$W_{44} \neq 0$	$W_{11} - W_{12} = 0$	$\Lambda$ or L transitions
$W_{44} = 0$	$W_{11} - W_{12} \neq 0$	$\Delta$ or X transitions
$W_{44} \neq 0$	$W_{11} - W_{12} \neq 0$	All transitions except $\Lambda, L, \Delta, X.$

that

$$\frac{\Delta R}{R} \sim (1 - R) \left( \frac{\Delta \omega_p}{\omega_p} + \frac{\Delta \tau}{\tau} \right)$$

Only the response to hydrostatic strain is significant. Since

$$\omega_p = (4\pi n e^2 / m^*)^{1/2}$$

and the dc resistivity

$$\rho = m^* / n e^2 \tau ,$$

$$\frac{\Delta \omega_p}{\omega_p} = \frac{1}{2} \frac{\Delta v}{v} \text{ and } \frac{\Delta \tau}{\tau} = \frac{\Delta v}{v} - \frac{\Delta \rho}{\rho} \sim -2 \frac{\Delta v}{v} ,$$

using data given by Garfinkel et al (1966) for the volume dependence of the resistivity of copper. The infrared piezoreflectance response for copper is then

$$\frac{\Delta R}{R} / e_{\text{hyd}} \sim -0.03 .$$

Strain affects the interband contribution to  $\epsilon_2^{ul}$  by perturbing both the transition matrix and joint density of states. The effect on  $J_{ul}(\omega)$  in the vicinity of a critical point is separable into a change in shape, due to altered band curvatures, and a change in the critical energy  $E_c$ , due to relative motion of the bands. The latter contribution dominates strikingly:

$$\begin{aligned} (\hbar\omega)^2 \Delta \epsilon_2^{ul} &\sim \frac{\delta J_{ul}}{\delta E_c} \frac{\delta E_c}{\delta e} e \\ &\sim (\hbar\omega - E_c)^{-1/2} \frac{\delta E_c}{\delta e} e \end{aligned}$$

because the square root threshold, in contrast to indirect threshold which all have exponents greater than unity, produces a one-sided infinite discontinuity at  $E_c$ , reduced when lifetime-broadening is taken into account to a finite response of the form (Batz, 1967)

$$\frac{\delta J}{\delta E_c} = -\frac{1}{\hbar} \frac{\delta J}{\delta \omega} \sim (2\eta)^{-1/2} F\left(\frac{\hbar\omega - E_c}{\eta}\right) .$$

The function  $F(X)$ , shown in fig.2.12, has the form

$$(X^2 + 1)^{-\frac{1}{2}} ((X^2 + 1)^{\frac{1}{2}} + X)^{\frac{1}{2}} .$$

The broadening parameter  $\eta$  is inversely proportional to the lifetime of the state.

The strength and sense of the reponse is also determined by the deformation potential  $\frac{\delta E_c}{\delta e}$ . A transition with weak associated structure in  $\epsilon_2$  may be enhanced relative to other transitions if it is more "sensitive", i.e. has larger  $\frac{\delta E_c}{\delta e}$ . Deformation potentials for energy gaps of interest in copper, according to calculations by Davis et al (1968) and Juras and Segall (1973), are given in table 2.3. Pure shear strain produces only a splitting of degenerate states with no overall shift.

The predicted piezo-optic response of the critical points in copper is summarised in table 2.4. Note that, for  $X_5 \rightarrow X_4'$  transitions (d-like states, transforming as xy and xz  $\rightarrow$  p-like state, transforming as x), the matrix element is non-zero only for the light polarised perpendicular to the  $k$ -vector of the states. This means (Gerhardt, 1967) that the joint density of states  $M_1$  critical point at  $X_4' - X_5$  increases in energy for positive  $e_{zz}$ .

Fig.2.13 shows the results from Gerhardt's (1967) measurements on single crystals of copper, which exhibits all these features. This work, and the subsequent linefitting of the inter-conduction band trigonal response (Chen & Segall, 1976) clarified our understanding of the optical properties of copper, providing accurate assignments of the transitions listed below.

Table 2.3

Critical point transition energies and deformation potentials

	Transition energy (eV)	Deformation potential (eV)	
		Piezoreflectance	Theory
$E_F - L_3^U$	$2.1 \pm 0.1$	D: $-1.1 \pm 0.1$	- 0.85
$X_4' - X_5$	$4.0 \pm 0.1$	$D_{zz}$ :	-22
$Q^+ - E_F$	$4.26 \pm 0.02$	( D: $-9.6 \pm 1.5$ $(D_{yz}$ : $-72 \pm 12$	- 5.0 -43
$L_1 - L_2'$	$5.04 \pm 0.04$	( D: $(D_{yz}$ :	- 8.4 -10.8

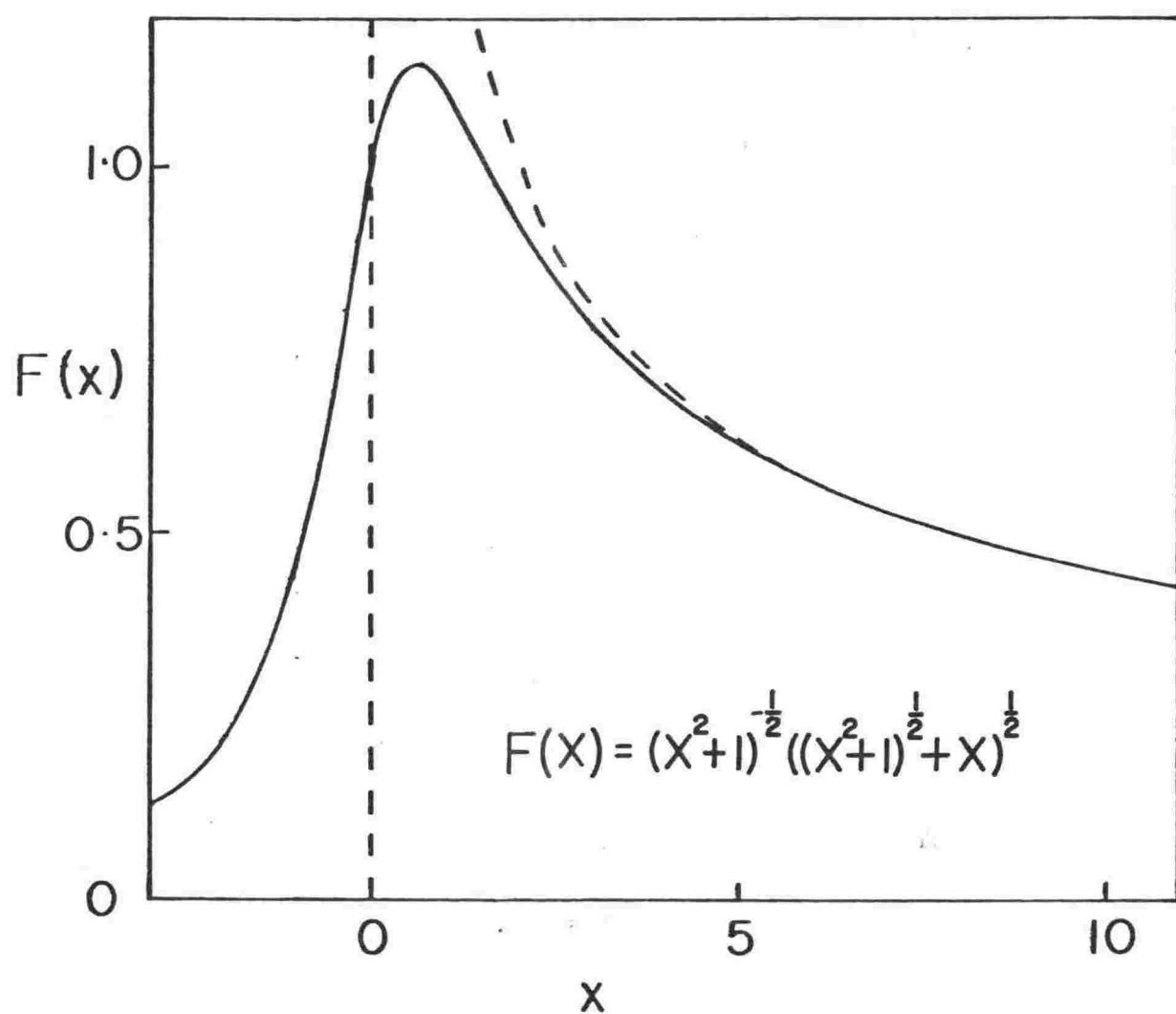
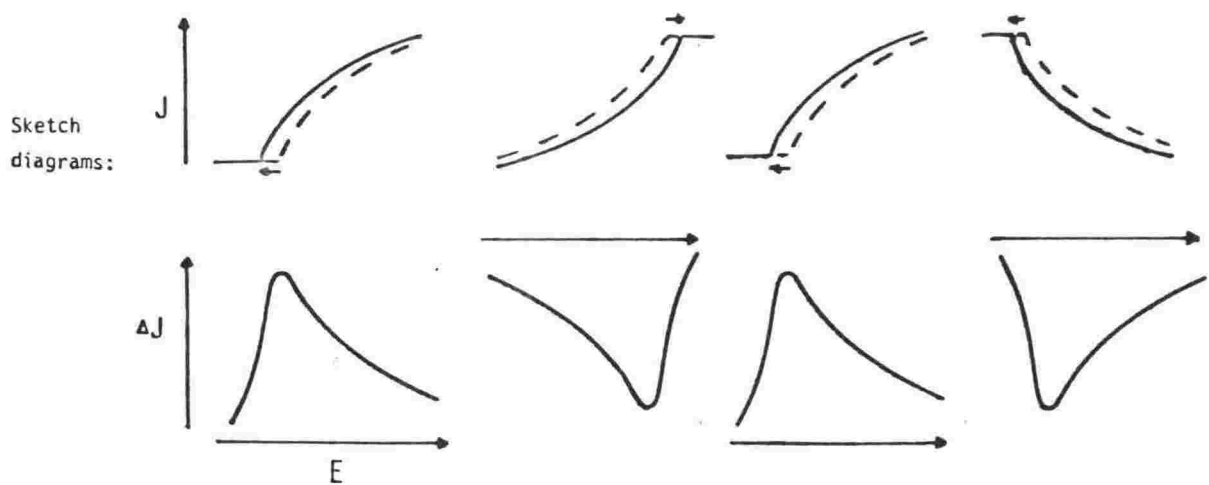


Fig .2.12 Derivative lineshape for copper from the experimental measurements of Gerhardt (1968).The change in the imaginary part of the dielectric constant per unit strain for hydrostatic, trigonal and tetragonal strain is given.



Band pair:	d band + conduction band (5 + 6)		interconduction band (6 + 7)	
	a	b	c	d
Singularity:	$M_0$ Fermi surface	$M_1$ Van Hove	$M_0$ Fermi surface	$M_2$ Van Hove
Energy:	$E_F - L_3^u$	$X_4^e - X_5^2$	$Q_+(L_1^u) - E_F$	$L_1 - L_2'$
Dominant deformation potential and sign:	Hydrostatic, negative	Tetragonal, positive	Hydrostatic, Trigonal, negative	Hydrostatic, Trigonal, negative
Piezo-optic signature:	$F(x)$	$-F(-x)$	$F(x)$	$-F(x)$
Sketch diagrams:				

1) Actually distorted because the contributing transitions are not localised in  $k$ -space.

2) Band 4 is degenerate with 5 at  $X_5$  and also contributes to  $J_{u1}$ .

Table 2.4 Piezo-optic response signatures of singularities in the joint density of states of copper.

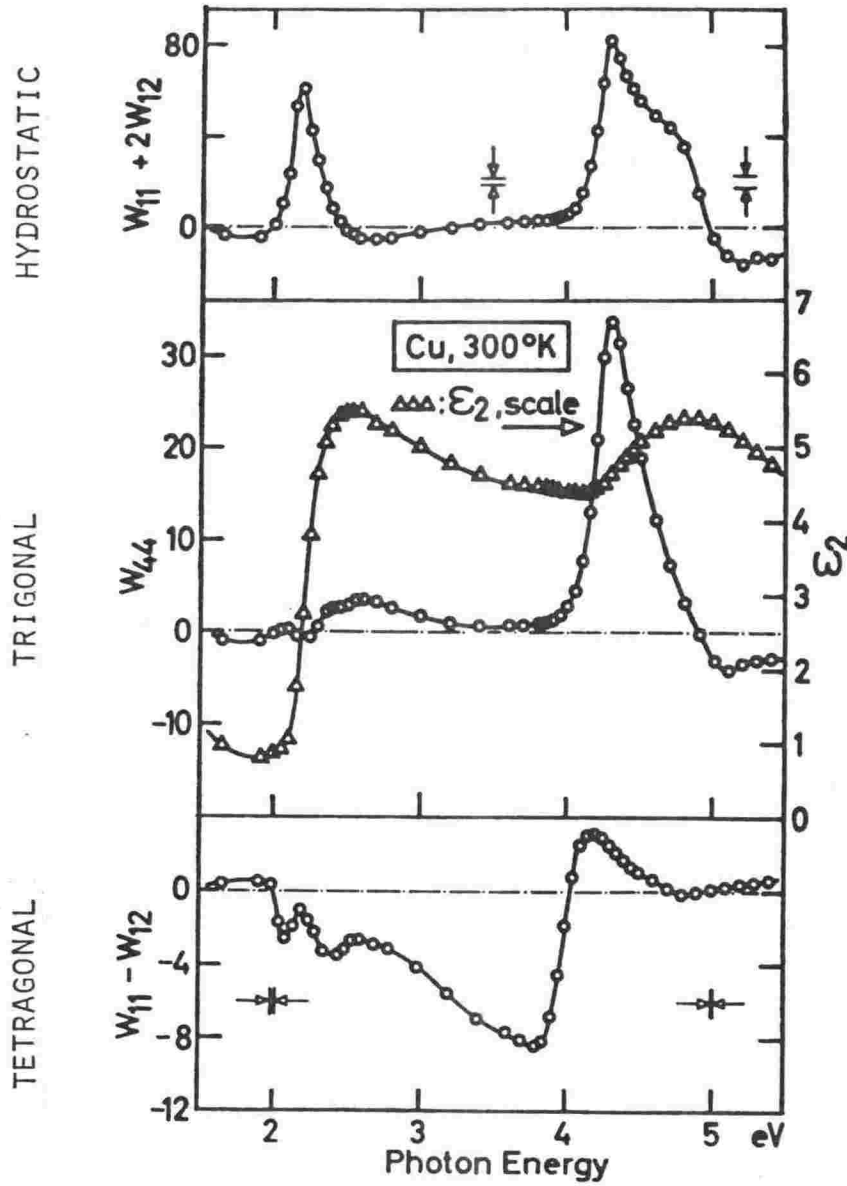


Fig.2.13 Piezo-optic constants for copper from the experimental measurements of Gerhardt (1968). The changes in the imaginary part of the dielectric constant per unit strain for hydrostatic, trigonal, and tetragonal strain are shown.

### Strain-optic properties of thin films

The structure of annealed evaporated films is not usually isotropic; on an amorphous substrate such as glass, typical crystallites have a lattice vector of low order oriented normal to the substrate plane, but are randomly oriented about this axis. Commonly, in the noble metal films the (111) and (to a lesser extent) the (100) normal orientations are preferred, as confirmed by X-ray diffraction studies reported on in Chapter 3.

The response measured in a piezoreflectance experiment on a polycrystalline sample must necessarily be comprised of a linear combination of the independent piezo-optic co-efficients (conventionally the hydrostatic, tetragonal and trigonal combinations of  $W_{ij}$  for cubic materials) the details of which depend on the degree of orientation ('texture') of the crystallites in the sample. A calculation of the linear combination of the single crystal co-efficients expected in the response from films comprised entirely of (001) or (111) oriented crystallites was made (see Appendices) for comparison with the experimental piezoreflectance spectra in conjunction with information about film texture obtained by X-ray diffraction. The poor correlation found (see Chapter 4) indicates that the inversion of piezoreflectance measurements on films to obtain the single crystal co-efficients would involve an impractical amount of effort, requiring further independent piezoreflectance measurements at oblique incidence or using torsional strain transducers and precise characterisation of the structure and elastic properties of the films. However, a partial separation of the contributing components is readily made; because the hydrostatic component is isotropic the differences between piezoreflectance responses measured with different polarisation must consist of a linear combination of the two single crystal shear co-efficients only.

### 3 SAMPLE PREPARATION AND CHARACTERISATION

#### 3.1 Sample Preparation

The samples used in these investigations were opaque films between 2000 and 3000 Å thick. Films were used in preference to bulk samples because of the convenience of preparation and the high quality surfaces which are readily obtained on glass substrates. The thickness of the films and the average crystallite size (both several thousand angstroms) were larger than the penetration depth for light and the electron mean free path (both less than several hundred angstroms) so that the results are representative of bulk properties. The penetration depth is large enough (many atomic layers) that light probes the electronic structure of the bulk material rather than the surface layer.

##### Multiple sample preparation

The alloys were prepared by simultaneous vacuum evaporation from separate solvent and impurity sources. This method had two advantages over evaporation from a single alloy source: several alloys could be produced at once and the concentration could be directly controlled. The position of the sources was exploited to produce simultaneously three sets of alloys of different concentrations and a pure sample. This saves materials and time. Further, any anomalies in the properties of the samples due to preparation conditions are likely to be common to all four samples and would thus not be erroneously attributed to the effects of alloying.

The intrinsic directional variation of the flux from usual sources is insufficient to produce sizeable differences in concentration given the constraints on placement of substrate and sources in the vacuum system. Instead meshes interposed between the impurity source and the substrates were used in the configuration shown in fig.3.1.

All sample positions were exposed to the solvent source, and the substrates' positions were curved as shown to reduce the variation in thickness of the samples due to angular variation of the solvent flux. For dilute alloys the alloy samples in the central positions were about 50% thicker than the pure sample. The pure position was masked from

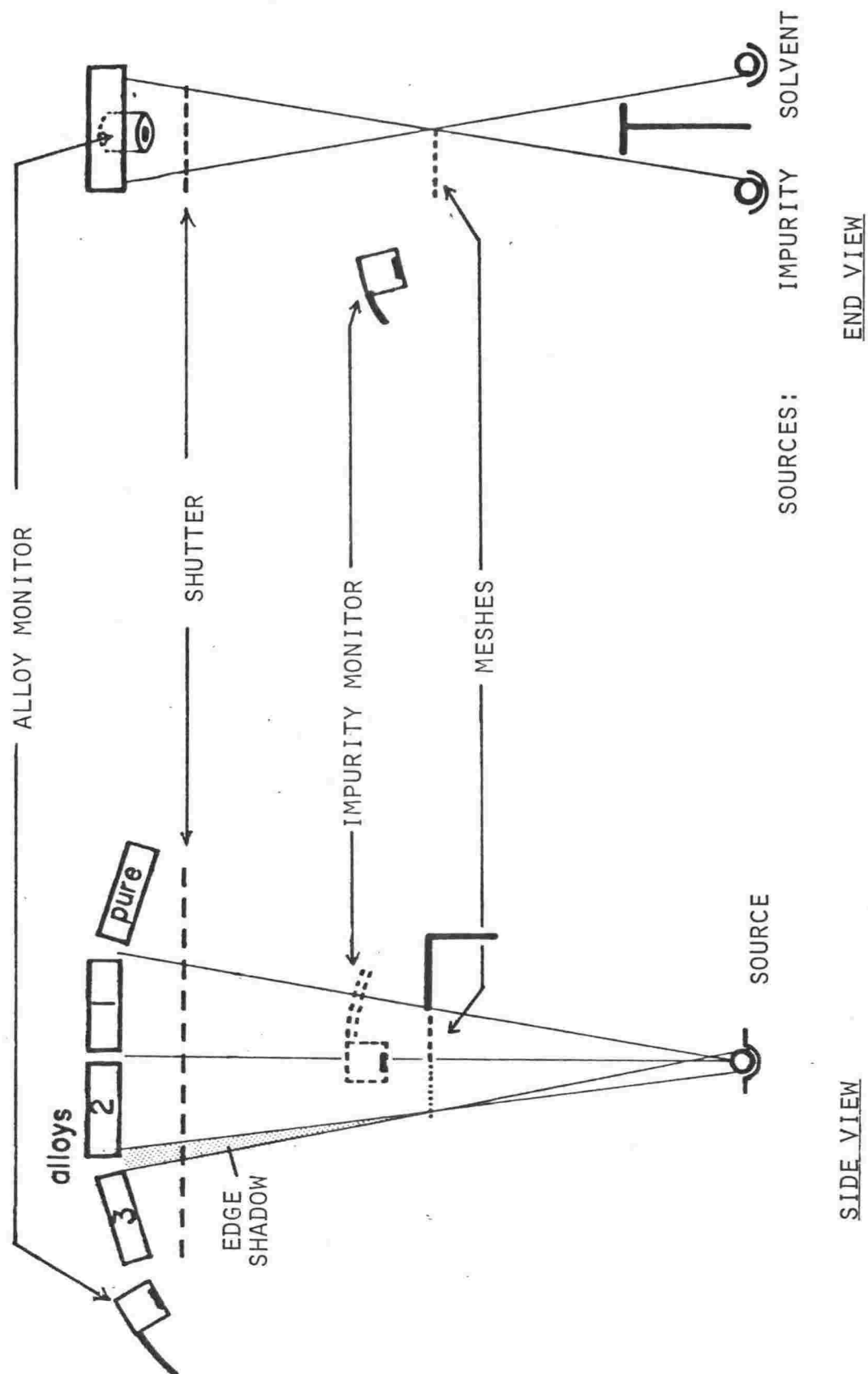


Fig.3.1 Placement of components in vacuum system for multiple sample deposition. The shading shows the area of non-uniform deposition caused by the shadow cast by the finite area of the source. (Shown for only one edge of a mesh for simplicity.)

the impurity source; positions 1 and 2 were shadowed by sections of mesh of different transmission; and position 3 was exposed. The sources, mesh and substrates were positioned by sighting the sources from the substrates. The microbalance sensors were sighted with a mirror from the source positions to confirm that the shutter and masks did not obstruct them.

The meshes had to be fine enough to avoid a speckled pattern of impurity deposition at the substrates. A check made by counting squares on graph paper for meshes of the appropriate transmission showed, for instance, that the maximum fluctuations are less than 2% if the source diameter is more than 14x the mesh spacing. A typical source diameter was 4 mm; larger sources produced a large shadowing overlap (see diagram) limiting the area of uniform deposition. In fact the impurity source boat had to be selected with this overlap problem in mind. Aluminium, for instance, tended to wet the boat and form an extended source. In contrast, the larger the solvent source the better for uniformity of evaporation. Copper mesh was used with a line spacing of 0.2 mm. The effects of speckling are thus unimportant especially since (a) all measurements are averaged over an area of the sample (20 x 7.5 mm for differential reflectance, 1 x 7.5 mm for piezoreflectance) producing at most only a broadening of the optical results, and (b) vibration of the mesh holder caused by pumps in the laboratory had an amplitude at least as large as the mesh spacing.

To obtain a good range of concentrations at one evaporation the ideal transmissions of the two sections of mesh are about 30 and 60%. All available commercial meshes had transmissions in the 35 - 28% range. The high transparency section was obtained by etching in dilute nitric acid. The mesh was mounted in the frame in which it was to be fixed in the vacuum system with all but the section to be thinned protected by dipping in a wax resist. The progress of the etching was checked by measuring the optical transmission. About 60% transmission was attainable.

#### Deposition monitors

The rates of evaporation were monitored by crystal microbalances (Sloan Technology Corporation). This is a

commonly used technique in vacuum deposition (Glang, 1970). The microbalance sensors were disc-shaped quartz crystals which oscillated at about 5 MHz in a thickness shear mode. One face was exposed to the source so that evaporated material condensed on it. The change in the period of oscillation (denoted by  $\Delta$ ) is proportional to the mass deposited. In this case one microbalance - the alloy monitor - was exposed to both solvent and impurity sources, and another - the impurity monitor - to the impurity source only. The system was calibrated at each alloy evaporation as follows. (1) The solvent only was evaporated. The ratio  $\Delta_i/\Delta_a$  ( $i$  = impurity,  $a$  = alloy) established how well the impurity monitor was masked from the solvent source. This was always  $< 10^{-3}$  so that corrections were unnecessary. (2) The impurity only was evaporated. The ratio  $A = \Delta_i/\Delta_a$  for this deposition allows one to deduce the mass deposited at the alloy monitor from that measured at the impurity monitor. The constancy of  $A$  depends on the stability of the configuration of the impurity source, so it was measured immediately before and after an alloy deposition. The impurity monitor is mounted closer to the source than the substrates or alloy monitor in order to improve the sensitivity of the rate measurement - especially for dilute alloys and light impurities such as aluminium. The ratio  $A$  was usually about 2.2.

The concentration is given from the changes in period measured during the evaporation by  $c = \Delta_i(Ar\Delta_a + (1 - r)\Delta_i)^{-1}$  where  $r$  is the ratio of the impurity atomic weight to the solvent atomic weight. The concentration so obtained is least reliable for the middle samples (alloys 1 and 2 in the figure) because the transmission of the meshes and the angular variation of the impurity flux (a variety of evaporation boats and charge configurations were necessarily used) were difficult to estimate.

#### Substrates

The substrates were two 1" diameter discs and one 3 x 3 x 42 mm rod which were mounted for deposition at each of the four sample stages.

The discs were of various materials: polished Vycor

(high silica glass), BAK 50 optical glass and ordinary float glass. The latter substrates were not polished but were certainly smooth enough to give good quality films. The rods were extruded fused silica polished on one long face.

The cleaning of the substrates was most important - if they were not clean a flawed, non-uniform deposit resulted. A variety of substrate cleaning methods was used. The simplest of methods (breathing on the glass and polishing with a tissue) often gave good results and the most stringent methods occasionally failed! The basic procedure used was:

- 1 Swab with acetone, transfer to glass racks (substrates mounted so they drain freely).
- 2 Immerse in hot Decon solution, use ultrasonic bath (~ 10 min.).
- 3 Thoroughly rinse in hot water using ultrasonic bath.
- 4 Place in isopropyl alcohol vapour degreaser (leaves no drying marks).
- 5 Inspect under a strong light against a dark background. If necessary wipe with tissues and repeat degreasing.

#### Vacuum system

The vacuum system was a Varian FC-12E 12" bell-jar system with five 40 li/sec ion pumps, a titanium sublimation pump, liquid nitrogen cryoarray, rough pumped by two sorption pumps.

The substrates were mounted on sample stages about 25 cm above the sources. Each consisted of a 4 x 6 cm copper plate, to which the substrates were fixed, backed by an aluminium shield enclosing an annealing heater - a 240 w quartz halogen projector lamp with bars prong connectors (no ceramics to outgas). Iron-constantan thermocouples monitored the temperature of the pure and middle alloy stages.

A shutter was used to cover the substrates during outgassing and establishment of the correct rates and to end deposition on the substrates when the required thickness was obtained. It was a trapdoor type, counterbalanced to keep it either open or shut, and switched by a one-second current impulse through a solenoid.

#### Sources

The sources were heated by two methods: a 2 kw electron gun and joule-heated tungsten boats of various designs. The



electron gun was used for the higher temperature sources and was preferred for the solvent because it performed best with a large charge of material. To obtain high rates of evaporation with copper in the electron gun the charge was thermally insulated from the hearth by a 6 mm circle of tantalum sheet. Evaporation boats were usually conditioned in a diffusion-pumped vacuum system to allow the charge to stabilise and to check the angular variation of the evaporation rate. Enclosed boats with small apertures were used in some cases to limit effective source size so that the meshes could be properly aligned. Some information about the sources used is summarised in table 3.1.

### Deposition

Automatic control of the evaporations was possible using Sloan digital deposition controllers which could be programmed to maintain the required rates of deposition, measured by the rate of change of microbalance oscillator period, by feedback control of the electron gun and boat currents. These worked well with the electron gun but the limited range of feedback loop gains meant that it was difficult to avoid unstable evaporation from the boats. In most cases it was better to control the boat current manually. A chart recorder trace of the impurity and alloy rates during the evaporation was made as a check on the variation of composition with depth.

A typical pump-down/evaporation procedure was as follows. From atmospheric pressure one sorption pump was used with the valve only partly opened and was closed off immediately the streaming phase of pumping was finished to prevent noble gases, which are not retained in the sorption pump, from diffusing back into the system. The second sorption pump was used for several hours while annealing heaters, boat and a heater winding around the vacuum chamber were heated gently and then allowed to cool to thoroughly outgas the chamber. On opening the poppet valve to the pumping chamber the pressure dropped immediately to about  $5.10^{-7}$  torr as measured by the ion pump current.

Three hours' use of the titanium sublimation pump - with the current and duty cycle adjusted to give maximum pumping rate, with the least possible heating and titanium consumption, with the help of a chart recorder output of the pressure - reduced

Table 3.1      Vacuum evaporation sources

<u>Material</u>	<u>Source</u>	<u>Te<sup>+</sup></u>	<u>Comments</u>
Cu	electron gun	1017	thermal insulation pad
	tungsten boat with alumina border S35B-A0*		alumina border prevents migration of charge to ends of boat
Zn	slotted tantalum tube modified S17B	250	sublimes
Al	Tungsten boat with lid S26	1010	wets and alloys with tungsten, attacks alumina
Ga	alumina coated molybdenum boat S9A-A0	907	
In	"	742	
Ge	electron gun	1167	

+Temperature in °C at which vapour pressure  $\sim 10^{-4}$  torr.

\*Catalogue numbers of RD Mathis Co., Long Beach, California.

the pressure to about  $5 \cdot 10^{-9}$  torr. During the latter part of pumping boat and electron gun charges were melted and outgassed, and the cryoarray filled with liquid nitrogen. The calibration evaporations were performed followed by the alloy deposition with the pressure typically in the  $10^{-7}$  -  $10^{-6}$  torr range and the rate of deposition usually about  $10 \text{ \AA}/\text{sec}$ . The substrates were at room temperature or slightly above.

### Annealing

Immediately after deposition the samples were annealed with the intent of:

- 1 Improving the perfection of the film by removing defects and promoting crystal growth. The crystallites increase in size from  $\sim 100$  to  $\sim 1000 \text{ \AA}$  in size.
- 2 Slowing deterioration of the film in atmosphere by presenting a less porous medium for the diffusion of oxygen.
- 3 Homogenizing the alloys.

Variations in the rate of evaporation from the two sources during the evaporation caused variations in the concentration of the alloy with depth. It was important that the surface layer sampled by light had an effective concentration close to the average concentration of the sample. The microbalance rate records suggested that in all but one evaporation, the surface composition differed by only a few percent from the bulk composition. Appropriate annealing should reduce this difference to a negligible level, but annealing at too high a temperature will cause surface roughening making the sample useless for optical measurements. As an example, for Ga in Cu ( $D_0 = 0.55 \text{ cm}^2 \text{ s}^{-1}$ ,  $\Delta H = 46 \text{ kcal mole}^{-1}$ ) one estimates the diffusion length  $\sqrt{Dt}$  (see e.g. Shewmon, 1963) on annealing at  $375^\circ$  for 15 minutes is about  $40 \text{ \AA}$ . The actual distance is certainly larger because the finite concentration and high defect and grain boundary density in the samples act to accelerate inter-diffusion. The temperature beyond which roughening occurs is quite unpredictable and depends sensitively on the surface condition of the substrate, judging from experience in the laboratory.

Resistivity measurements are a common method of monitoring annealing as the residual resistivity drops as vacancies and

grain boundaries migrate and interdiffusion occurs. Four-point resistance measurements in vacuo were inconvenient so annealing temperatures found to be suitable in other studies in the laboratory and elsewhere were used (Chopra et al, 1977). The standard annealing was 20 minutes at 200°C for copper and 350-400° for alloys. The Cu-In samples, which possibly exceeded the equilibrium solubility limit of In in Cu (~ 1 at% at room temperature, 11 at% at 575°C: Hansen, 1958), were not annealed in order to retain the extended solubility range commonly associated with vapour quenched films. The Cu-In piezoreflectance measurements were repeated after annealing.

As a check on their homogeneity, samples with suspected variation of composition with depth were re-annealed at 500°C ( $\sqrt{Dt}$  for Ga ~ 700 Å) and showed negligible shifts in the piezo-optical structure most sensitive to alloy concentration.

### 3.2 Sample Characterisation

For our present purpose - basically the determination of various energy gaps as a function of alloy concentration - an accurate knowledge of the concentration of the samples is equally as important as obtaining reliable optical measurements. The methods used for determining the concentration of the films were restricted by the small amount of sample available - typically  $10^{-3}$ g. The techniques used were resistivity measurements, X-ray diffraction measurements of the alloy lattice constants, and X-ray fluorescence. These are described in turn and the results for all methods presented in summary.

Structural information about the samples was also relevant to the piezo-optical studies and this was mainly obtained by X-ray diffraction.

#### Resistivity

In dilute binary solid solutions the relationship  $\rho_{\text{alloy}} = \rho_{\text{pure}} + \rho_{\text{impurity}} + \rho_{\text{defects}}$  is found to hold, where the residual resistivity due to the impurity is related to the concentration by  $\rho_{\text{impurity}} = c\delta\rho_i + c^2\delta^2\rho_i + \dots$ . Data for bulk pure copper and alloys are given in table 3.2.

Four-point resistance measurements were made on the films on piezoreflectance substrates using a frame with voltage contacts

20 mm apart which could be moved along the edge of the film. Resistances were in the 0.5-3.5  $\Omega$  range and were reproducible to better than 1%. The main difficulty was in determining the sample thickness. The most accurate direct method available in the laboratory for films in this thickness range was multiple beam interferometry - a Sloan A-scope was used. Accuracy better than  $\pm 100 \text{ \AA}$  was difficult to obtain however. A few film thicknesses were measured in this way but a more convenient indirect method was to estimate relative film thicknesses from X-ray fluorescence measurements of the copper concentration, normalising resistances and thicknesses to those of the pure samples (see Appendices). The fluorescence measurements are described in a later section. They gave an average thickness at a single measurement, with molybdenum masks defining an appropriate section of sample, and were capable of precision better than 1%. In the dilute range the uncertainty in composition was between 0.5 and 1 at% Zn and proportionately less for the other impurities with higher residual resistivities. The resistivities of the various annealed pure films (thicknesses inferred from A-scope measurements) were all larger than the bulk value and varied over a considerable range (2.05-2.65  $\mu\Omega \text{ cm}$ ) despite their similar histories. This excess resistivity may arise from size effects - scattering at surfaces and grain boundaries - and from vacancies, other defects, and gas adsorption. The size effects should be proportional to the ratio of electron mean free path (about 300  $\text{\AA}$  in pure copper at 300°K) to film thickness or grain size, amounting to  $\frac{3}{8} \frac{1}{t} \rho_{\text{bulk}}$  for diffusely scattering surfaces (see Chopra, 1969). This implies about a maximum 5% surface scattering correction in a typical pure sample - not enough to account for all the excess resistivity. Defect residual resistivity in alloy films tends to increase with impurity concentration and may amount to 2-3  $\mu\Omega \text{ cm}$  (Chopra et al, 1977). There is no guarantee that the defect residual resistivity is removed by annealing to the same extent in all samples. A defect contribution to the residual resistivity larger in the alloys than in the pure sample would produce an over-estimate of the concentration.

Further, the results at concentrations beyond about 5 at%

Table 3.2      Residual resistivity reference data for  
copper based alloys

<u>Solute</u>	<u><math>\delta\rho(\mu\Omega\text{cm at}\%^{-1})</math></u>	<u><math>-\delta'\rho/\delta\rho(\text{at}\%^{-1})</math></u>	<u>Ref.</u>
Zn	0.25	0.023	1, 5
Al	1.10, 0.95	-	2, 3
Ga	1.25	0.032	1
In	1.06	0.024	4
Ge	3.8	0.032	1

Resistivity of pure Cu at 18°C = 1.67  $\mu\Omega\text{cm}$

- 1                      Crisp and Henry (1978)  
 2                      Coleridge (1975) (dilute limit only)  
 3                      Blatt (1968)  
 4                      Linde (1932)  
 5                      Biondi and Rayne (1959)  
N.B.                      Linde's values for Zn and Ga are respectively  
 28 and 14% higher than found in more recent studies

Table 3.3      Lattice constant reference data for copper  
based alloys (from Pearson, 1968)

<u>Solute</u>	<u>Lattice constant change</u>	<u>(111) line shift</u>
	<u><math>\frac{da}{dc} (10^{-3}\text{\AA}/\text{at}\%)</math></u>	<u><math>\frac{2d\theta}{dc} (\text{deg}/\text{at}\%)</math></u>
Zn	2.15	0.027
Al	2.41	0.030
Ga	2.88	0.036
In	9.45	0.119
Ge	3.36	0.042

Uncertainty in  $\frac{da}{dc} \sim \pm 0.05$ . Pure Cu lattice constant at 20°C:  
 3.6147  $\text{\AA}$ . Quadratic terms negligible except for Zn for which  
 $\frac{d^2a}{dc^2} \sim 0.003 \frac{da}{dc} \text{at}\%^{-1}$ .

may be affected by ordering effects which are known to occur in the  $\alpha$ -phase of several of these alloy systems (Hansen, 1958).

#### Lattice constants

In all the alloys studied the impurity causes expansion of the copper lattice. The literature data (for annealed bulk filings) is summarised in table 3.3. The lattice constants of the films were determined by X-ray diffraction using a Philips diffractometer with a curved crystal graphite monochromator, copper  $K_{\alpha}$  radiation, and proportional counter. In a diffractometer the detector and sample surface are maintained in a reflection-like geometry so that diffracted radiation is detected at an angle equal to the angle of incidence of the X-rays on the sample. Thus the only crystal planes contributing to the measurement are those lying parallel to the plane of the substrate, and the angular position of the line determines the lattice dimension normal to the substrate. All of the sample films had a (111) texture - the crystallites were preferentially oriented with the close-packed (111) planes parallel to the substrate. Thus the (111) diffraction lines were much stronger than the (200) and other lines and they alone were used for determining lattice constants. Substrates were held in a three-point mount clamped on the diffractometer spindle. Only the substrates, and not the holder, were shifted between measurements to avoid altering the alignment. The diffractometer was programmed to make point-by-point counts, 10 seconds per point, over a range of  $2^{\circ}$  centred on the peak at intervals of  $0.01^{\circ}$  over the peak. Angle, counts and time were output on paper tape. A programme was written for the PDP-15 computer to display the line profile for a visual check, subtract a linear background and calculate the centroid of the line-shape which was taken as the most reliable measure of angular position (Vassamillet & King, 1967). Typical results are shown in fig.3.2a. For most of the samples reproducibility was limited to about  $0.006^{\circ} 2\theta$  by unavoidable variations in mounting the substrate in the holder but for samples with weaker (111) lines counting uncertainties limited precision to about  $0.01^{\circ} 2\theta$ . A calibration of the diffractometer was not attempted - shifts were all measured relative to the peak position for the

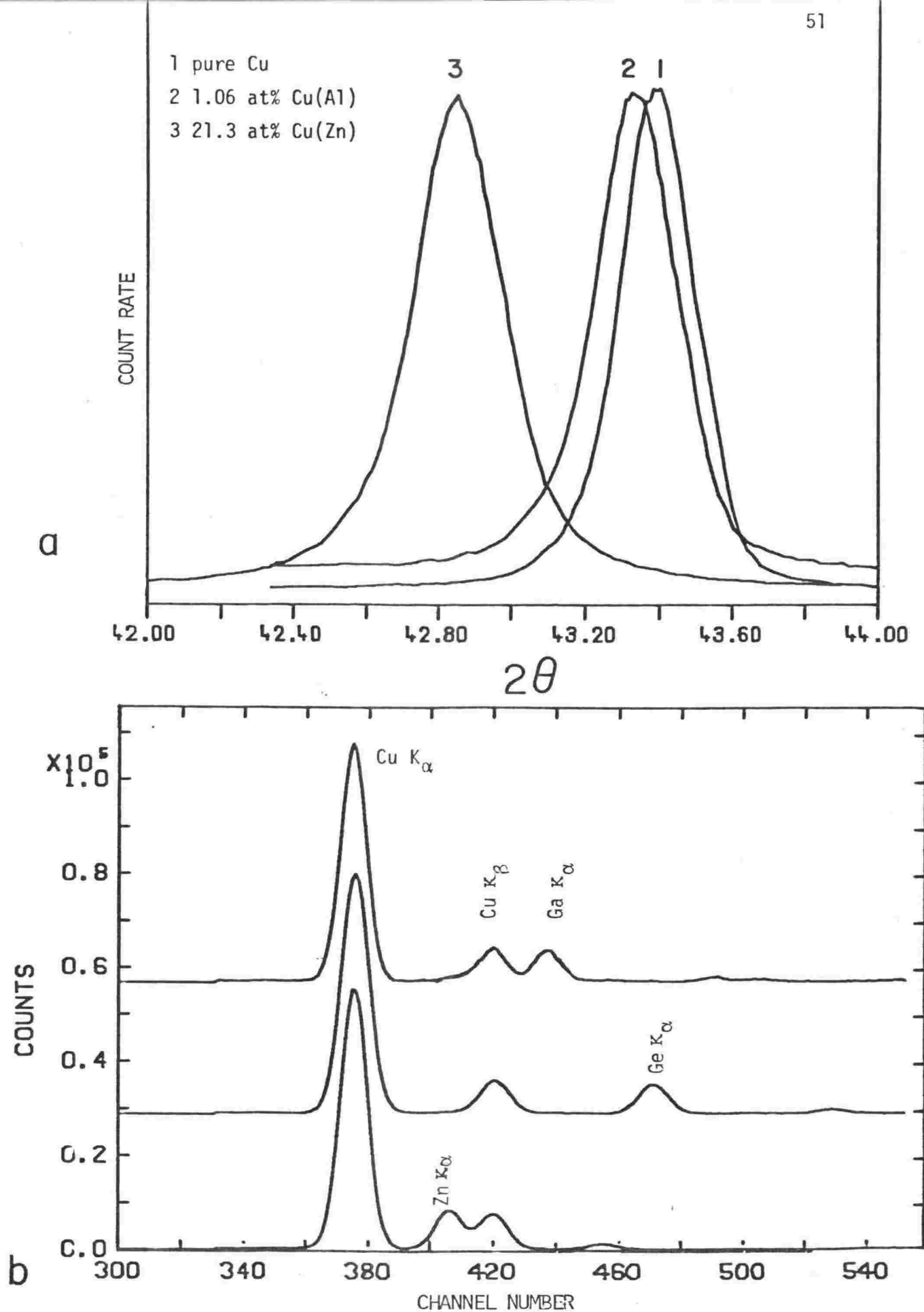


Fig. 3.2 Typical measurements for composition analysis:

(a) X-ray diffraction line shapes

(b) X-ray fluorescence spectra.



pure copper films. This has the advantage that any change in lattice constant due to strain in the films is likely to be similar in pure and alloy samples and so will be cancelled out. The possibility of strains large enough to significantly affect the results cannot be discounted however. Comparison of X-ray diffraction measurements on some alloy films immediately after deposition and after annealing showed a shift of the (111) line to larger  $2\theta$  angles by up to  $0.1^\circ$  - this is equivalent to the effect of several at% of impurity. Differences between pure and alloy samples in any residual strain after annealing will produce an error.

#### X-ray fluorescence

When an atom is excited by absorbing an X-ray it may return to its ground state by emitting fluorescent radiation at an energy characteristic of the element. The intensity of the fluorescent radiation gives a direct measure of the concentration of the element provided account is taken of the effects of absorption of the exciting and fluorescent radiation. In the case of thin film samples, these corrections may be small. An X-ray fluorescent system with monoenergetic exciting radiation was used so that the dependence on atomic number of the efficiency of excitation and detection of fluorescent radiation was amenable to calculation (Giaque et al, 1973). Some thin film standards of known concentration were also prepared for comparison. The system utilised molybdenum  $K_\alpha$  and  $K_\beta$  exciting radiation with sample incidence and emergence angles of about  $45^\circ$ . An Ortec Si (Li) detector and 6240A multichannel pulse-height analyser were used.

The concentration is obtained from the relative intensities of the  $K_\alpha$  lines for copper and the impurity;

$$C = \frac{I_i}{k_i I_{Cu} + I_i}$$

where  $k_i$  gives the excitation and detection efficiency per mole for the impurity relative to copper, obtained by interpolation from data given by Giaque et al (1973),

and from measurement on standards of known concentration.

Element:	Cu	Zn	Ga	Ge
$k_i$ Interpolated:	1.00	1.23	1.46	1.70
Standards:			1.49±0.03	1.91±0.02
$K_\alpha$ energy (kev)	8.04	8.63	9.24	9.87
$K_\beta$ energy (kev)	8.90	9.57	10.26	10.97

Data for the aluminium  $K_\alpha$  fluorescence at 1.49 kev and indium  $L_\alpha$  fluorescence lines around 3.3 kev could not be obtained. In both cases the efficiency of excitation is low, absorption effects are large, and no measurable solute fluorescence was detected in the samples. The zinc and gallium  $K_\alpha$  lines overlapped the copper  $K_\beta$  line (representative spectra are shown in fig.3.2b). The  $K_\beta$  contribution was removed by subtracting a pure copper  $K_\beta$  profile normalised to the  $K_\alpha$  intensity. Corrections for the absorption of the Ga and Ge fluorescent radiation by copper V were significant, amounting to up to 5% in the thicker Cu Ga alloys. Mass absorption coefficients were obtained from Jenkins and de Vries (1967). The production of the thin film standards represents a new application of the crystal microbalance: a layer of copper and of the impurity each ~ 500 Å thick were deposited on the sensor crystals with the mass measurable to a precision of a few parts in  $10^3$  - and the film on the crystal used as a standard. Because Zn condenses erratically at room temperature a Cu-Zn standard could not be prepared.

#### Summary of results

It is important to recall the limitations of each of the methods before comparing results. Resistivity measurements may be affected by defect residual resistivity. Lattice constant measurements may be affected by strains in the films. X-ray fluorescence was not applicable to Al and In and relied on interpolated data for absolute Zn concentrations. The concentrations according to the crystal microbalance (see discussion of vacuum system) should have approximated those of the most concentrated

alloy prepared at each evaporation but, apparently due to the rapid decrease of flux from the electron gun at oblique angles, gave concentrations 30-60% larger than the other methods.

The results may be summarised as follows. For the Zn and Ge alloys all three methods were used. The X-ray fluorescence and diffraction measurements were in good agreement, with 0.6 at% Zn and 0.3 at% Ge standard deviation between the results obtained by the different methods. This is consistent with a combination of  $0.01^\circ$  uncertainty in diffraction line position and fluorescence counting errors and establishes the accuracy of the diffraction method for well annealed films. Resistivity measurements for alloys of less than 5 at% were in agreement with the results of the other methods to within experimental errors, with the exception of Cu-In. The departures for higher concentrations are attributable to residual resistivity, due to defects not removed by annealing, of less than  $1 \mu\Omega \text{ cm}$  or to deviations from the simple quadratic dependence of the impurity resistivity.

The resistivity results for the three Cu-In alloys suggested concentrations uniformly three times larger than the lattice constant results. Apart from the possibility of an error in the bulk resistivity data it is possible that segregation of the alloys had occurred. The solubility of In in Cu has a maximum of about 10.5 at% at  $575^\circ\text{C}$  decreasing to about 1 at% at  $100^\circ\text{C}$  (Hansen, 1958). The most concentrated sample was 1.25 and 3.8 at% according to lattice constant and resistivity measurements respectively. The microbalance, with allowance for overestimate, suggested 2.0 at%. These results might be explained by a 2 at% alloy with less than 3% of its volume composed of the  $\delta$ -phase  $\text{Cu}_9\text{In}_4$ . Such a precipitate was not evident in X-ray or electron diffraction, but this is not surprising considering the small proportion postulated, hardly enough to affect the optical results. In either case, the lattice constant composition is

likely to be most appropriate.

In summary, the compositions given for the alloys in all following discussion are those from X-ray fluorescence measurements for Zn, Ga and Ge and from X-ray diffraction for Al and In. The uncertainty in concentration ranges from 0.2 to 0.5 at% - the uncertainty in the relative concentrations for a given system are, in some cases, significantly less.

#### Film structure

The structure of a film - by which one means the distribution of crystallite size, shape, and crystallographic orientation with respect to the substrate (texture) - has some bearing on its optical properties. The static optical properties of cubic materials are affected only in the limit of small grain size and high defect concentration by broadening and regions of weak anomalous absorption (Hunderi, 1979). The texture of the samples has no influence.

The piezo-optical properties are dependent on crystal orientation and hence on film texture. This was evident in the variation in piezoreflectance spectra for different pure copper samples and in changes produced in alloy samples by annealing. One of the difficulties in interpreting piezoreflectance measurements on polycrystalline samples is the possible confusion between changes due solely to alloying and changes due to variation in the texture of the samples. The correlation of film structure, as measured by X-ray diffraction, with piezoreflectance results can provide information to assist in distinguishing between the two effects.

The width of an X-ray diffraction line is related to the average grain size of the sample. The line broadening  $\beta$  in excess of instrumental broadening produced by a crystallite of size  $D$  (measured normal to the substrate in the diffractometer configuration) diffracting radiation of wavelength  $\lambda$  by an angle  $2\theta$  is  $\beta = \frac{K\lambda}{D\cos\theta}$ . The Scherrer constant  $K$  is close to unity. A broadening of the (111) line by  $0.1^\circ$  corresponds to  $D \sim 1000 \text{ \AA}$ .

In some alloy films measured before annealing,  $D$  was typically 200 Å, less in alloys of higher concentration. In annealed pure copper films and most of the alloys  $D$  was measured to be close to the thickness of the film. In a few of the more concentrated alloys after annealing at 375°C  $D$  remained as low as 300 Å.

The relative strength of the  $(hkl)$  diffraction line, normalised to a standard sample thickness, gives a measure of the fraction of the sample in crystallites with  $(hkl)$  planes parallel to the substrate. In a sample with no texture the line strengths should be in the ratio  $(111):(200):(220) = 100:46:20$  (Powder Diffraction File). A check on a powder sample gave 100:38:19, in fair agreement, given the difficulty of preparing an unoriented powder sample.

The measurements showed primarily that film texture is a highly variable property. To begin with, the alloy samples of a given composition on the disc and rob substrates, prepared simultaneously under identical conditions, differed in texture, as measured by the  $(200):(111)$  ratio, by up to a factor of two. Over all the samples measured the strength of the  $(111)$  line normalised to sample thickness, varied by a factor of about 30. Samples produced at the same evaporation showed much less variation - up to three-fold. The  $(200):(111)$  ratio was typically about 0.15, i.e. compared with an untextured sample the  $(111)$  orientation was relatively about 300% more abundant than the  $(200)$  orientation. The ratio ranged from 0.3 to 0.01 - in some cases this was due to a weak  $(200)$  line, in others to a very strong  $(111)$  texture. The  $(200)$  line was even weaker, often escaping detection. The definite order of orientation preference:  $(111)$ ,  $(200)$ ,  $(220)$  was invariable. Generally the texture was least in films with smaller average grain size.

Some specific cases of correlation of this structural information with piezoreflectance are discussed in the following chapter.

## 4 OPTICAL MEASUREMENTS

The object of the experimental work has been to obtain  $(\hbar\omega)^2\Delta\epsilon_2$  spectra from piezoreflectance measurements on a number of alloy samples of accurately known concentration.

The basic optical data required are the reflectivity  $R$  and piezoreflectance  $\frac{\Delta R}{R}$  spectra for each alloy. In this work the alloy reflectivity has been derived from the reflectivity of a pure sample and the quantity

$$\alpha = \frac{(R_{\text{pure}} - R_{\text{alloy}})}{(R_{\text{pure}} + R_{\text{alloy}})}$$

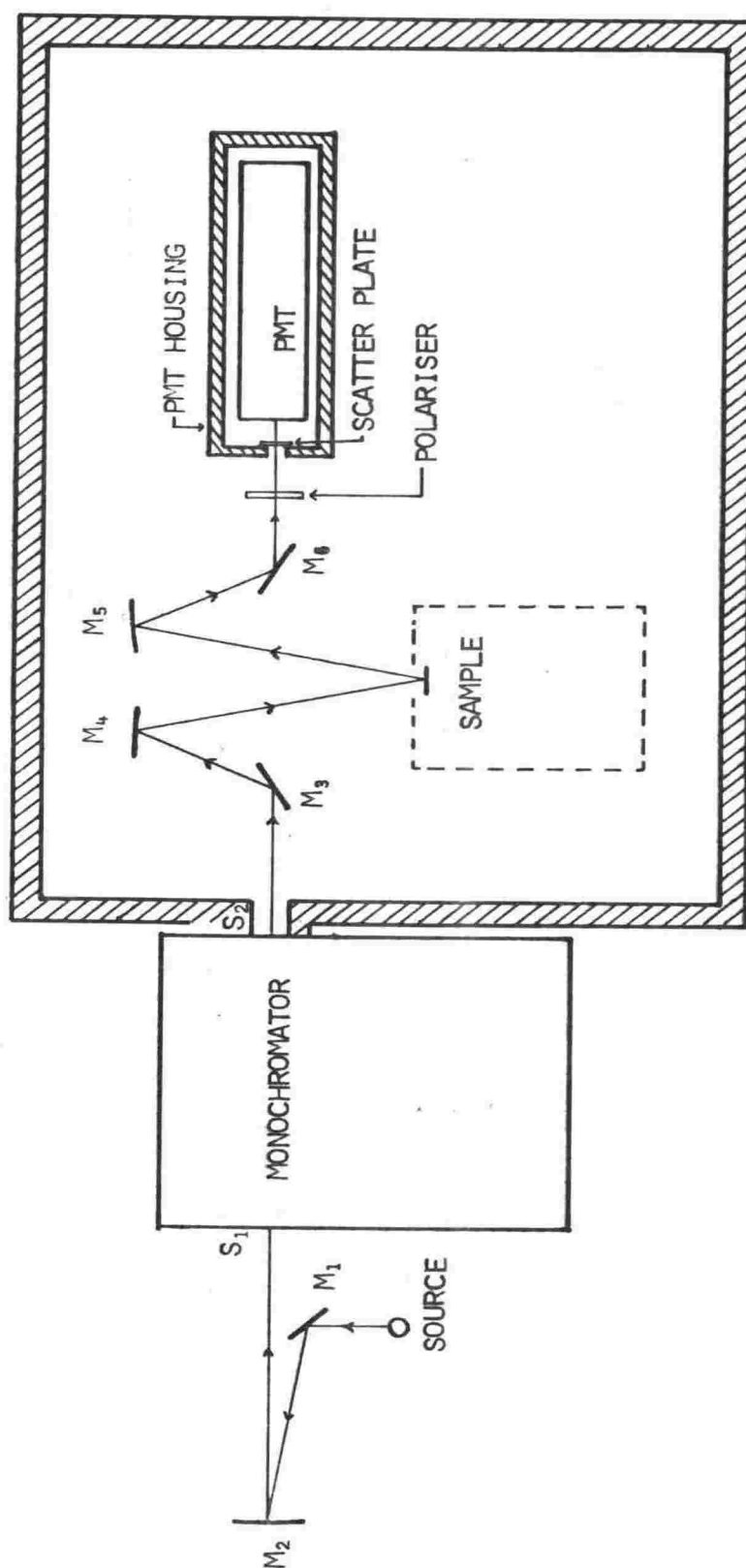
which is directly measured using a differential reflectometer (Beaglehole, 1968). The reasons for using this procedure rather than a direct measurement of the alloy reflectivity will be made clear in the discussion of the reflectometer in the following sections. Also, an appropriate choice of extrapolation for the  $R$  data in the Kramers-Kronig transform (see 2.3) at high energies is guided by independent measurements of the optical constants. An angle-of-incidence modulation technique (Hunderi, 1972) was used to obtain these. The three systems constructed to perform these measurements are described in this chapter. Some details of possible interest to future users of the systems are left to the appendices.

Finally, it is emphasised that the optical measurements are to be used to determine transition energies; systematic errors can be tolerated so long as they do not appreciably shift the apparent transition energies.

### 4.1 Piezoreflectance

#### Optical system

The optical system is shown in fig.4.1. This simple configuration is common to many modulated reflectance systems. Light from the source is focused in turn on monochromator slits, sample, and detector.



$M_1, M_3, M_6$  plane mirrors  
 $M_2$  spherical mirror  
 $M_4, M_5$  toroidal mirrors  
 $S_1, S_2$  monochromator slits  
 PMT photomultiplier tube

Fig.4.1 Piezoreflectance optical system schematic diagram.

The source was a 75-watt high pressure xenon short arc lamp in fused quartz envelope. Its output is a continuum with some broad lines extending from the near IR to 240 nm. The monochromator was a Spex 1670 Minimate. Its f.4 optics allow a large solid angle of the lamp output to be condensed on the entrance slit. The slits used were 1.25 mm wide giving a resolution (full width at half maximum of a narrow spectral lamp line) of about 4.5 nm, which corresponds to almost 0.02 eV at 2.25 eV.

All mirrors in the system had vacuum evaporated front surface coatings of aluminium. The angle of incidence at the sample was  $10^\circ$ .

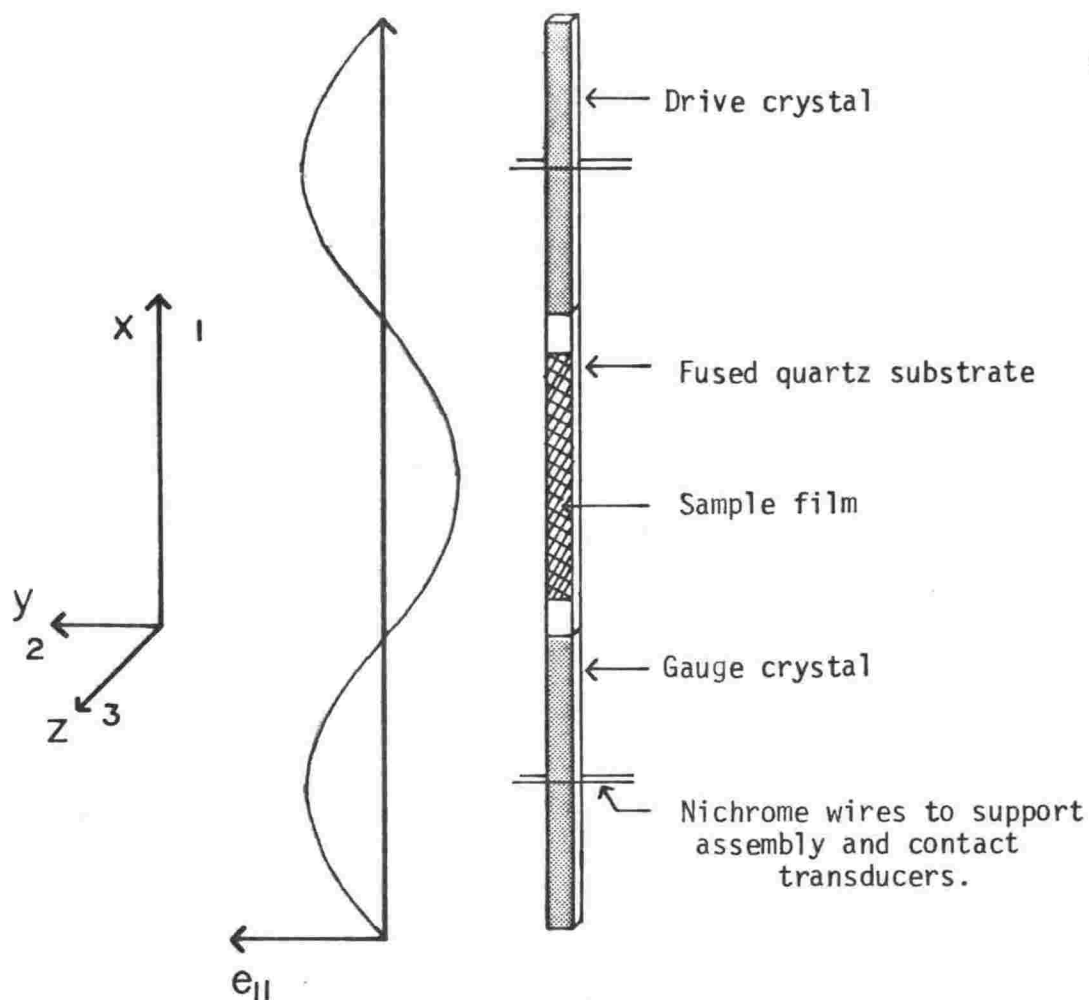
The polariser was Polacoat 105 UV polarised coating (3M Optical Products Division) on a  $\frac{1}{16}$ " thick quartz substrate. Its polarising properties are given in the appendices. Correction for the low extinction ratio from 3.5-4.5 eV is considered later.

The detector was an EMI 9558Q photomultiplier tube with S-20 response characteristic. Whereas the source limited the useful ultraviolet range to  $\sim 250$  nm the low quantum efficiency of the photomultiplier imposed a limit at about 800 nm in the infrared. A scatterplate was used to give diffuse illumination of the detector to minimise error signals caused by any motion of the light beam combined with spatial variation in the sensitivity of the detector. Such inhomogeneities may be due to variation in the sensitivity of the photocathode or to light transmitted through the photocathode being scattered from the dynodes within (Gerhardt, 1967). The scatterplate was 1 mm thick fused quartz lightly ground on both surfaces with 800 mesh silicon carbide powder. It reduced the detected intensity by about 50%.

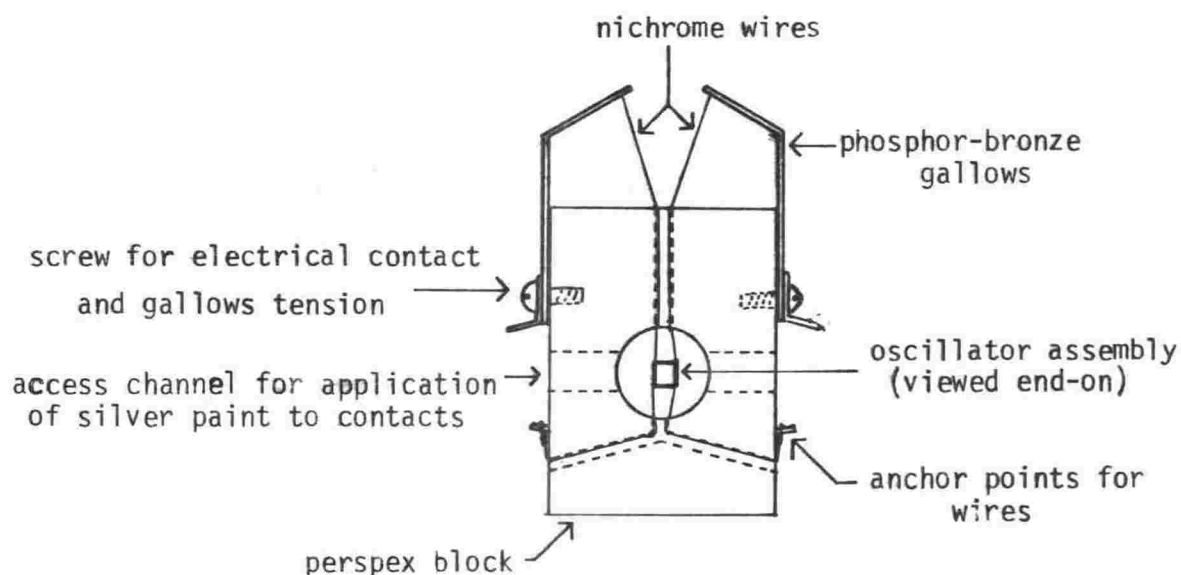
### Strain transducer

The strain transducer (fig.4.2) was a composite oscillator driven at resonance, formed by two piezoelectric quartz crystals ( $-18.5^\circ$  x-cut  $\alpha$  quartz, dimensions 3 x 3 x 38 mm) sandwiching the sample substrate, which was a fused quartz rod (3 x 3 x 42 mm) with the sample





Composite crystal oscillator - showing longitudinal strain distribution in assembly.



End-on view of gallows used to support the composite assembly.

Fig.4.2 Piezoreflectance strain transducer.

film deposited on one face. The composite oscillator had several advantages over transducers used previously with evaporated films (Garfinkel et al, 1966) which contribute to reducing systematic errors. The substrate had a high quality optical finish and could be demounted for cleaning and sample preparation. The high resonant frequency ( $\sim 68$  kHz) and symmetry of the assembly (at the support points there is no lateral displacement) minimised vibration of the sample and optical components.

The components were cemented with a quick-setting cyanoacrylate adhesive. The point could be broken by flexing over an edge when demounting. Electrodes of conductive silver paint on the transducers were contacted by fine wire supports kept under tension by phosphor bronze "gallows". One of the crystals - the "drive" crystal - had an a.c. voltage applied by an oscillator circuit and from the voltage developed across the other - the "gauge" crystal - the strain developed in the assembly could be calculated. The gauge crystal also provided a frequency reference for synchronous detection and the feedback voltage for the drive oscillator (closed loop crystal driver, manufactured by Solid State Equipment Ltd., Lower Hutt, NZ) which varies the drive voltage to maintain the gauge voltage at a constant level. The strain in the transducer is a standing wave with the longitudinal strain amplitude in the substrate given by (Robinson & Edgar, 1974)

$$e_{11} \sim 3.10^{-5} V_g$$

where  $V_g$  is the rms gauge voltage and the numerical factor involves the dimensions and properties of the components (see Appendices for details). The transverse strains are related to the longitudinal strain by Poisson's ratio:

$$e_{22} = e_{33} = -\nu e_{11} \quad (\nu = 0.17 \text{ for fused quartz}).$$

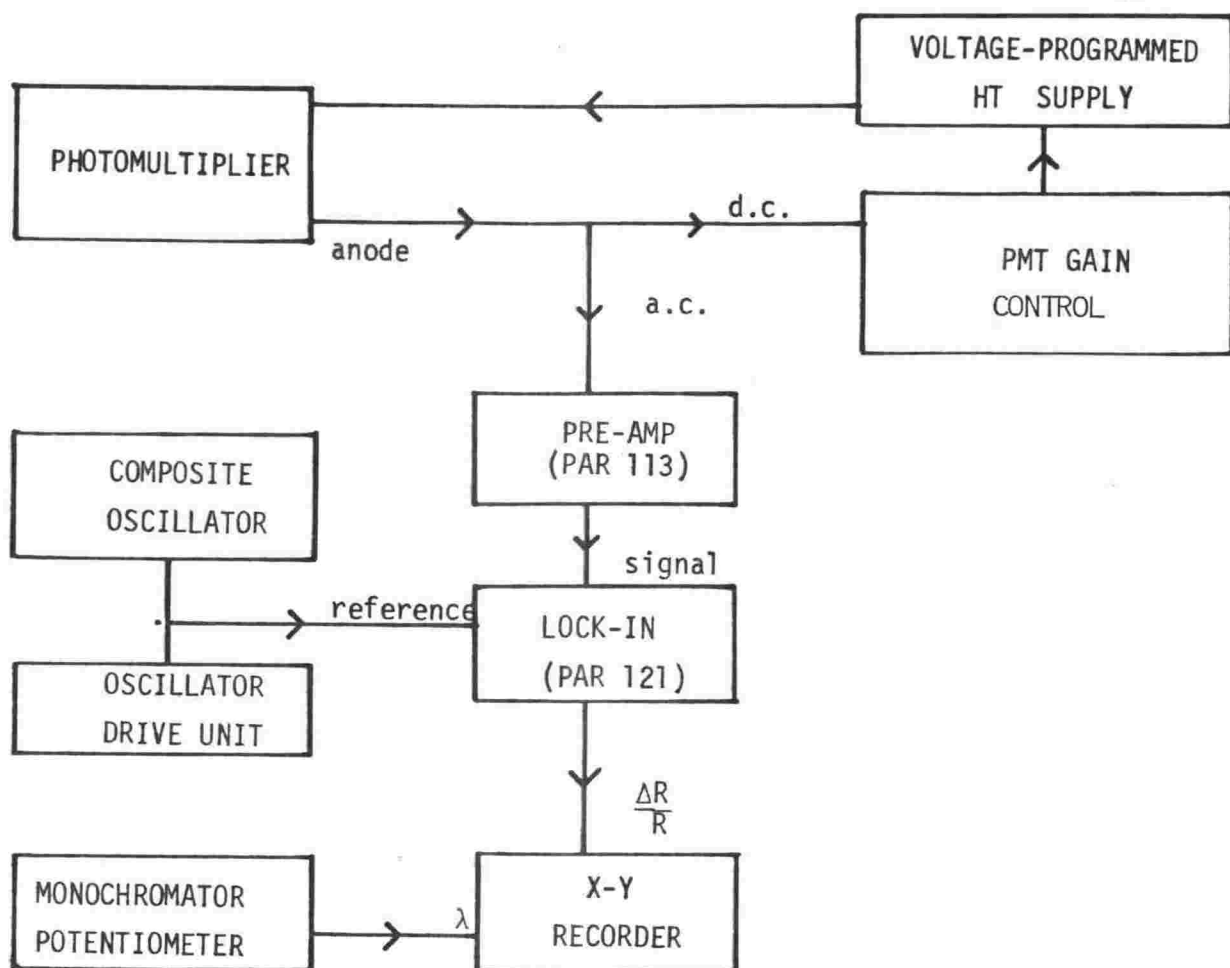
Shear strains are negligible for transducers of this cut and dimensions. A typical experimental strain was about

$3 \cdot 10^{-4}$ . At strains exceeding  $10^{-3}$  the transducers are liable to shatter.

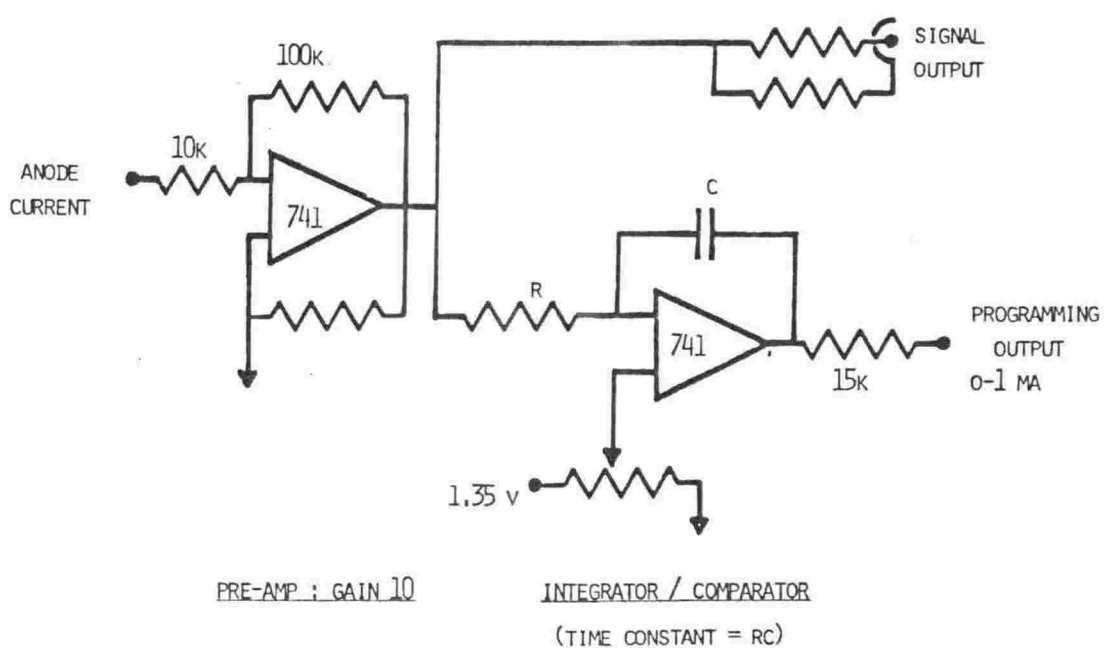
The spatial variation of the strain and finite image size imply that the effective strain sampled by the beam is smaller than the maximum. For the dimensions here the reduction is 1%.

### Electronics

Fig.4.3 shows the electronic instrumentation schematically. Strain induced modulation of the reflectance of amplitude  $\frac{\Delta R}{R}$  produces a corresponding fractional variation  $\frac{\Delta I}{I}$  of the photomultiplier anode current. In this experiment the average current  $I$  was held constant so that the a.c. current synchronous with the strain modulation, detected using a lock-in amplifier, gave  $\frac{\Delta R}{R}$  directly. Lock-in amplifiers operate by multiplying the input voltage by a square wave at the reference frequency, obtained in this case from the gauge crystal. Only that part of the input coherent with the reference contributes to the d.c. part of the output and so an RC integrating filter on the output can produce a very narrow effective band pass. The average anode current was held at  $10 \mu A$  to better than  $10^{-3}$  precision by a feedback circuit comprising an error amplifier and programmable high voltage supply which provided automatic control of the photomultiplier gain. The gain control time constant was  $10^{-3}$  sec so that the 68 kHz modulation was not attenuated. The absolute precision, excluding noise, of the strain normalised fractional reflectance change  $\frac{1}{\epsilon} \frac{\Delta R}{R}$ , i.e. the calibration of the system, was of the order of a few percent. The spectrum was scanned continuously and the data recorded on an X-Y recorder with the X input derived from a potentiometer meshed with the monochromator drive shaft. Since data was read directly from the graph paper at a resolution of 20 nm/inch care was taken to ensure that the scale was linear and free from drift. The recorder variable gain was insufficiently sensitive for range adjustments so external potentiometers were used for this. To record a 600 nm spectral range for both polarisations took almost two hours with optimum time constants (see Appendices).



System block diagram



Basic photomultiplier gain control circuit

Fig.4.3 Piezoreflectance system electronics.

### Accuracy

**Noise:** A typical experimental trace is shown in fig.4.4. The shot noise of the photoelectron current from the photomultiplier imposed a limit on the precision of the piezoreflectance measurements, as was obvious from the increased noise at wavelengths where the intensity was low. The ratio of rms noise to d.c. photomultiplier current ranged from about  $2 \cdot 10^{-6}$  to  $2 \cdot 10^{-5}$  for a 3 sec time constant (0.08 Hz bandwidth).

**Stray light:** As the ultraviolet limit of the lamp spectrum is approached a significant fraction of the light intensity is contributed by stray light scattered from the grating with a spectral distribution similar to that of the source. It was a constant background throughout the ultraviolet as far as could be ascertained using long pass filters at the monochromator entrance slit to block the 'true' light and, of course, that part of the scattered light originating outside the filter pass band. Dark current was negligible. Corrections were made as detailed in the appendices. The corrections were quite large in the ultraviolet - up to 50% at 4.5 eV increasing rapidly towards 5 eV. An independent check on their accuracy was made with point-by-point measurements using a deuterium arc source with a lock-in time constant of 30 sec. This source gave little stray light in the ultraviolet but was not suitable for routine use because its low intensity led to unacceptable noise levels. The deuterium arc and corrected xenon arc results agreed to within the 5% experimental uncertainty.

**Polarisation:** Corrections for imperfect polarisation can be made (see Appendices) provided that  $k_2/k_1$  - the ratio of polariser transmittance for light polarised perpendicular and parallel to the polariser axis and  $I_{\perp}/I_{\parallel}$  - the ratio of the intensities of each polarisation - are known. ( $I_{\perp}/I_{\parallel}$  varies markedly through the spectrum because of the polarising properties of the monochromator grating.) The corrections, illustrated later in this chapter, were significant only for transverse polarisation (light polarised perpendicular to the longitudinal strain axis) over a limited spectral range and, in fact, were not generally applied to the spectra

**Spurious modulation:** Variation in the light intensity

caused by motion of the sample, optical components or light beam synchronous with the strain modulation will produce an error signal. Any response at energies well below the inter-band threshold in copper is clearly due to such errors since an insignificant response is expected in the infrared,  $< 5.10^{-3}$  of the magnitude of the threshold feature - see Chapter 2.4. The measurements of Garfinkel et al (1966) on copper show a wavelength-dependent error signal of the same magnitude as the threshold feature.

As mentioned earlier, the use of the composite oscillator strain transducer and the scatterplate were features of the present experiment which acted to reduce error signals by minimising vibration of the apparatus and sample surface, and their effect at the detector. Nevertheless a small error signal was observable with most samples. The signal at wavelengths longer than about 600 nm was constant but non-zero. Its magnitude was less than 1% of the largest features in the spectrum in almost all cases. Its dependence on sample condition and on alignment suggested it was caused by a combination of lateral and tilting motions of the sample and that it was largely independent of wavelength. The procedure was adopted of subtracting the constant required to adjust the infrared signal to zero from each spectrum. Because of the smallness of the offset the effect on the results is insignificant.

#### 4.2 Differential Reflectance

The reflectometer devised by Beaglehole (1968) has several modes of operation and was constructed and used in this work to measure  $\frac{R_1 - R_2}{R_1 + R_2}$  and  $\frac{1 - R}{1 + R}$  where  $R$  is the reflectivity and the subscripts denote different samples ( $p \sim$  pure,  $a \sim$  alloy).

For these alloy studies  $\frac{1 - R_p}{1 + R_p}$  was measured and  $R_{\text{alloy}}$  obtained from  $\frac{R_p - R_a}{R_p + R_a}$  measurements. The reasons for this indirect determination of the alloy reflectivity were as follows:

- (a) Convenience: Measurements of  $\frac{1 - R}{1 + R}$  were subject to greater systematic errors, the reduction of which was time-consuming and exacting.
- (b) Precision: The  $\frac{R_p - R_a}{R_p + R_a}$  technique can measure directly

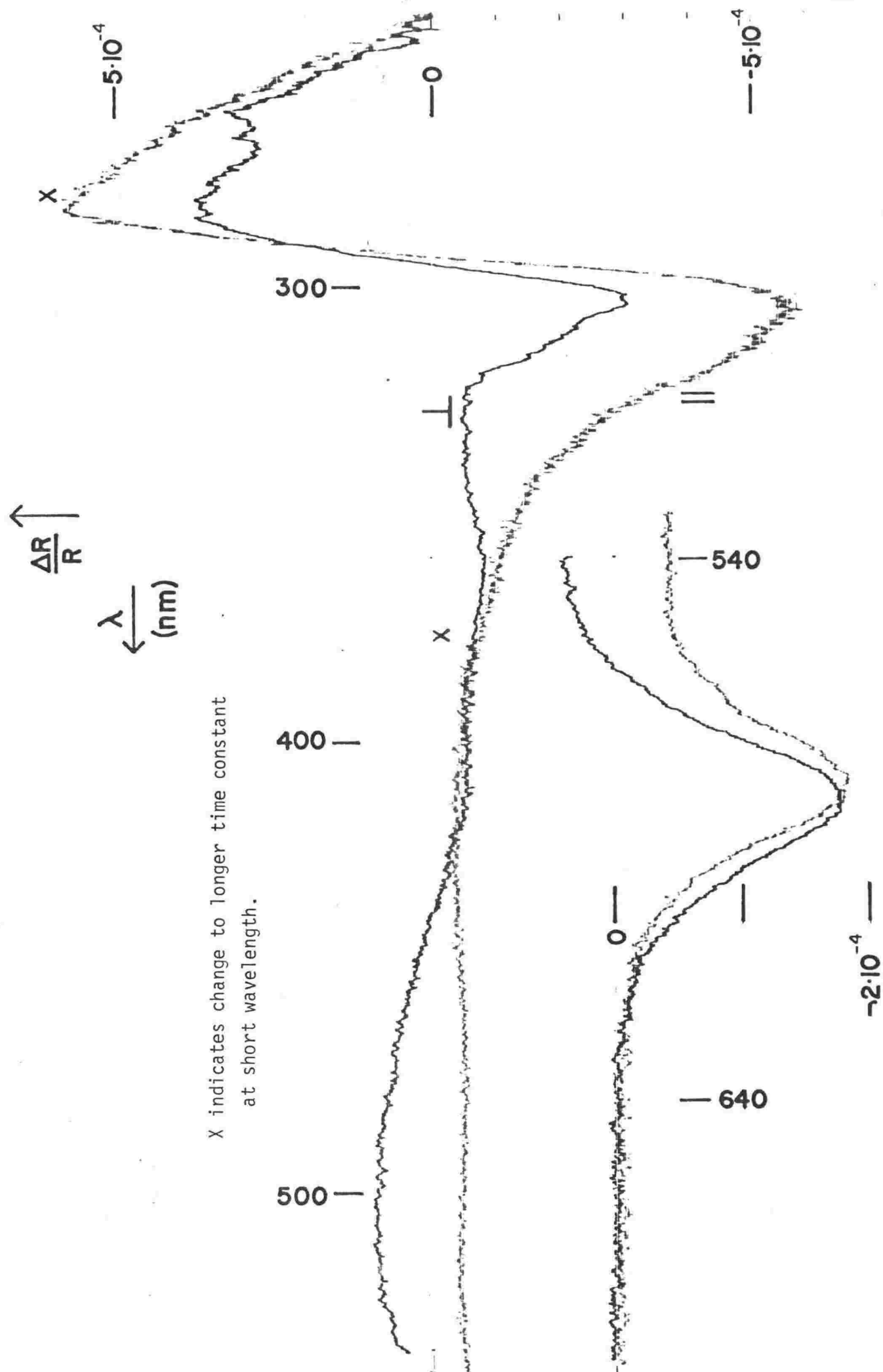


Fig.4.4 Typical experimental piezoreflectance trace for pure copper film.

and with little scope for systematic error the changes in the reflectance spectra caused by alloying. The 'background' reflectance common to both samples is subtracted and the significant information - the changes - is accentuated.

The operation of the instrument is described with reference to fig.4.5. A pair of samples (say 1 and 2) are mounted in apertures in a blackened disc rotating in the light path. The detector output is a succession of pulses originating from light reflected from each of the samples in turn. The component of the detector output at the frequency of rotation of the disc is proportional to the difference in the reflectivity of the samples. The d.c. (average) component is proportional to the sum of the reflectivities, and by holding this constant by controlling the photomultiplier gain, and detecting the difference signal with a lock-in amplifier, the ratio  $\frac{R_1 - R_2}{R_1 + R_2}$  is directly measured. To operate in the other mode, one of the samples is removed and the unobstructed aperture simulates a perfect reflector so that  $\frac{1 - R}{1 + R}$  is measured provided  $R_{m5} R_{m6} S = R'_{m5} R'_{m6} S'$  where  $S$  is the detector sensitivity and the prime denotes the transmitted path. Calibration is particularly simple - a blank aperture backed by an absorbing card simulates zero reflectance so that the lock-in output then corresponds to unity.

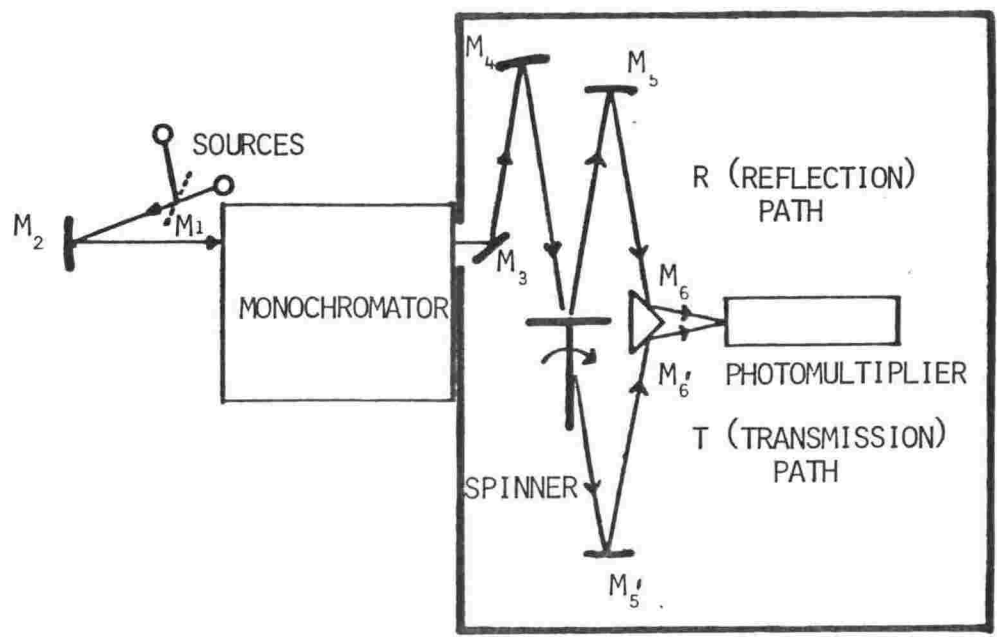
#### Optical system

Two sources were used. A 55-watt tungsten filament quartz halogen lamp covered the range 800-400 nm and a deuterium arc lamp from 450-210 nm. Sources could be quickly changed by shifting the mirror  $M_1$ .

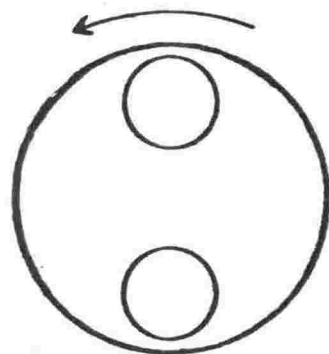
The monochromator was a Jarrell-Ash 82-405 Minichromator. The beam was focused at the entrance and exit of the monochromator and at the sample and detector.

All mirrors were vacuum deposited aluminium coatings.  $M_5$  and  $M_5'$  and  $M_6$  and  $M_6'$  (on the faces of a 45° prism) were coated simultaneously in order to match the reflected and transmitted paths. The angle of incidence on the sample was 9.5°. The photomultiplier and scatterplate were similar

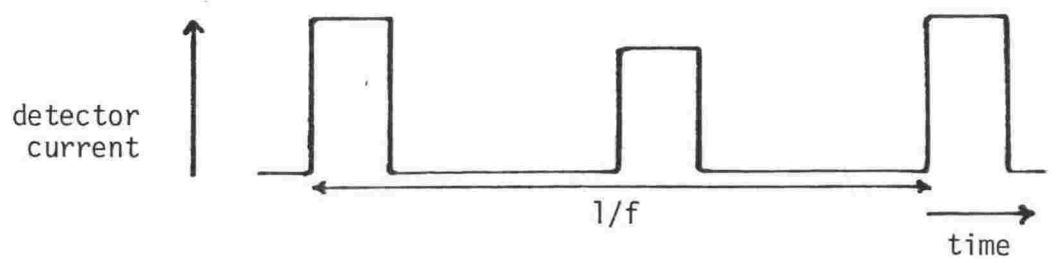




Differential reflectance optical system



Spinner disc showing apertures



Sketch of detector output

Fig.4.5 Differential reflectometer : layout of optical system, spinner disc, detector output.

to those in the piezoreflectance system.

The samples, on 1" diameter substrates, were mounted on the sample rotating disc or spinner in independently adjustable inserts. These were aligned so that rotation of the spinner produced no perceptible motion of the reflected beam at  $M_5$ . The spinner was rotated at 23.0 Hz by a synchronous motor. The lock-in reference was provided by a lamp and photo-voltaic cell interrupted by a chopper on the spinner shaft.

The electronics (fig.4.6) were quite similar to the piezoreflectance set-up. With optimum time constants (see Appendices) scans were made at about 100 nm/minute.

#### Sample interchange and precision

$\frac{R_p - R_a}{R_p + R_a}$  mode: The salient feature of the differential reflectometer is the possibility of interchanging the samples in the spinner apertures so that when the difference between the two signals obtained is taken, all error signals which do not change sign on sample interchange are cancelled. Residual errors produced by misalignment and differences in aperture size were of the order of  $10^{-3}$  of the signal magnitude. Errors due to stray light evident in the region of overlap of the different sources and filters were typically less than  $10^{-3}$ .

$\frac{1 - R}{1 + R}$ : The major sources of error in this mode are the differences in reflectivities of pairs of mirrors, beam inversion by the extra reflection of the R beam, and the R and T beams reaching the detector from different directions. The former errors of order  $3 \cdot 10^{-3}$  could be partially cancelled by interchanging mirrors. The latter error was more serious, becoming evident in the sensitivity of  $\frac{1 - R}{1 + R}$  to the positioning of the detector when R approaches unity in the infrared. The effect was reduced by rotating the photomultiplier about its cylindrical axis until the orientation which minimised the sensitivity of the output to its longitudinal position was found. This orientation was, unfortunately, not independent of wavelength so the error could not be eliminated. The difference between effective apertures

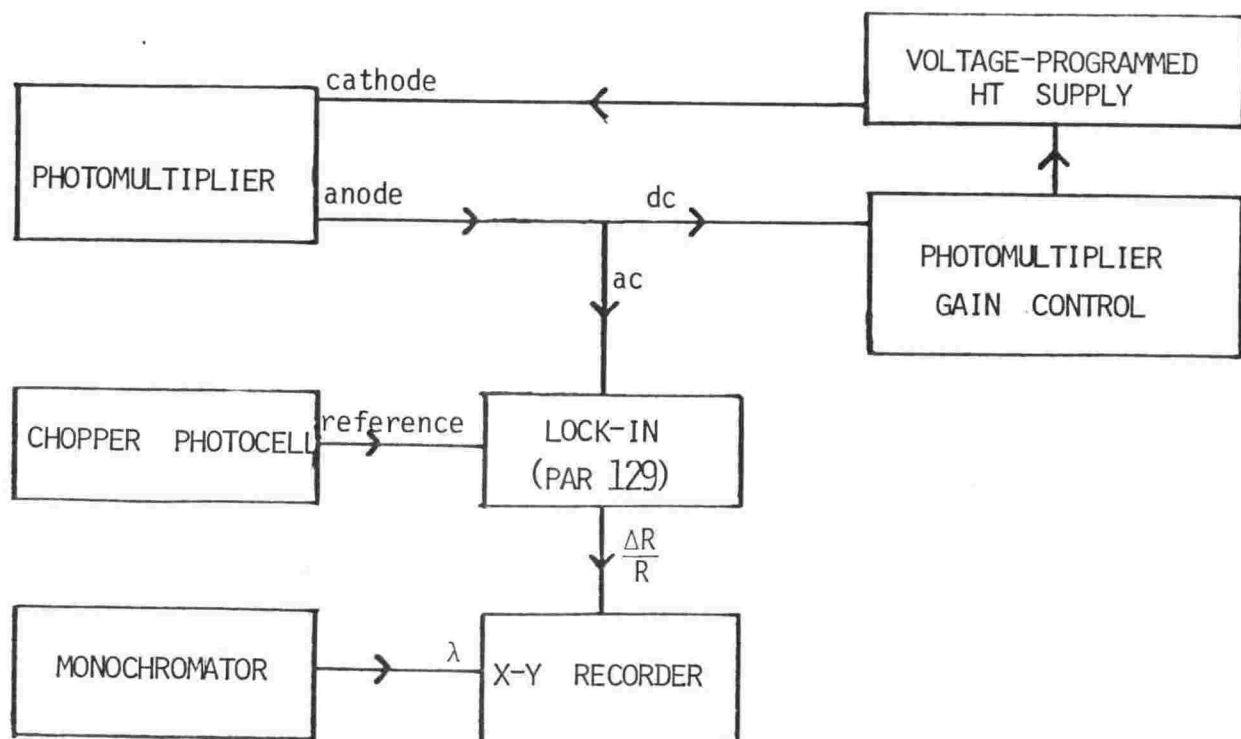


Fig.4.6 Differential reflectance system electronics.

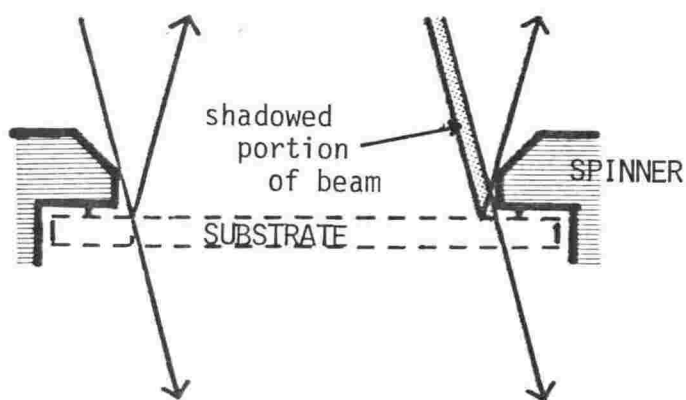


Fig.4.7 Difference between effective aperture sizes of differential reflectance spinner for reflected and transmitted beams. Shadowing by the lip of the aperture blocks the reflected beams path to the detector fractionally earlier than the transmitted beam.

for the R and T beams (fig.4.7) was measured at  $5.10^{-3}$  with an oscilloscope by comparing the duration of the detector pulses from an empty aperture and a highly reflecting sample, and corrections made. The absolute accuracy of R was estimated to be about  $5.10^{-3}$ . The reflectivity at 750 nm of a gold sample agreed with independent measurements to within this limit.

#### 4.3 Angle of Incidence Modulation System

In this technique the fractional change in reflectance per unit change in angle of incidence was measured. Discussion will be brief since the method is fully discussed by Hunderi (1972). He measured

$$G(\theta) = \frac{1}{R_s} \frac{dR_s}{d\theta} - \frac{1}{R_p} \frac{dR_p}{d\theta}$$

at a single angle of incidence and the normal incidence reflectivity and numerically solved for  $\epsilon_1$  and  $\epsilon_2$ . (s and p refer to light polarised respectively perpendicular and parallel to the plane of incidence.) Alternatively  $G(\theta)$  can be measured at two angles of incidence and accurate numerical solutions can be obtained provided that the two families of curves of constant G are well spaced and do not run parallel in the region of interest in the  $\epsilon_1, \epsilon_2$  plane.

In this work, G was measured at two angles (usually  $45^\circ$  and  $60^\circ$ ) and at three wavelengths (436, 460 and 500 nm) to obtain  $\epsilon_1$  and  $\epsilon_2$ . The reproducibility of the G measurements was  $\sim 5.10^{-3}$  implying uncertainty of  $\sim 0.04$  in  $\epsilon_2$ . The form of the ultraviolet extrapolation of the reflectivity data was varied to give best agreement between the  $\epsilon_2$  obtained from Kramers-Kronig inversion and the experimental  $\epsilon_2$  values. The most reliable guide to the extrapolation is given by  $\epsilon_2$ ; compared to  $\epsilon_1$  it has about 40% lower uncertainty and the Kramers-Kronig  $\epsilon_2$  results are about twice as sensitive as  $\epsilon_1$  to adjustment of the extrapolation. The extrapolation procedure and the effects of errors in the  $\epsilon_2$  values are considered in the appendices.

Oxide surface films can seriously affect the results.

Computations were made to investigate the effect of assuming a  $\text{Cu}_2\text{O}$  surface film of refractive index  $n = 2.9$  (Nikitine, 1969) - moderate absorption in the oxide does not much affect the results. For thin oxide films the reflectance of pure copper at 460 nm is reduced by about  $0.025 \text{ nm}^{-1}$  of oxide film thickness and  $\epsilon_1$  and  $\epsilon_2$  obtained from  $45^\circ/60^\circ\text{G}$  measurements are both reduced by  $0.5 \text{ nm}^{-1}$ . Roberts, (1960) estimates a 1 nm oxide layer forms in under an hour, 2 nm in less than 24 hours. The ellipsometric measurements of Pells and Shiga (1969) found  $\epsilon_2 \sim 7$  at 460 nm for samples annealed and measured under vacuum reduced to an apparent  $\epsilon_2 \sim 4$  in air. In our case the  $\epsilon_2$  values at 460 nm deduced from G measurements varied from  $\sim 4$  in aged films to 5.0 in freshly evaporated films.

The angle of incidence system may also be used as an accurate infrared reflectometer as mentioned by Hunderi. In the limit

$$|\epsilon_1| \gg \epsilon_2 > 0, \epsilon_1 < 0$$

$G(\theta)$  is given by  $1 - R$  multiplied by a function of  $\theta$ , i.e. in this region of the  $\epsilon_1, \epsilon_2$  plane the contours of constant  $R$  and  $G$  run parallel. However, for the noble metals at wavelengths shorter than 800 nm the approximation is not good. Nevertheless, reflectance values calculated from the  $\epsilon_1, \epsilon_2$  values obtained by the normal method were quite reproducible, much more so than the  $\epsilon_1, \epsilon_2$  values. By this means the reflectance at 750 nm of an annealed gold film, for which oxide effects should be minimal, was measured to be  $0.972 \pm 0.002$  (the value given in the AIP handbook is 0.971) providing a reflectivity standard for the differential reflectometer.

#### 4.4 Results

##### Data processing

The foremost object of the data processing was to obtain spectra of strain-induced  $(\hbar\omega)^2 \Delta\epsilon_2(\omega)/e$  for parallel and transverse polarisations which, to recall Chapter 2.4,

is directly related to the strain modulation of the joint density of states. Static  $\epsilon_2$  spectra give supplementary information.

The piezoreflectance and differential reflectance spectra were visually smoothed and digitised to give files of 150-200 point length. A description of the computer programmes which performed stray light and polarisation corrections, Kramers-Kronig integration, plotting of the spectra and line-fitting is given in the appendices along with a summary of the extrapolation procedure and any errors it may introduce in the spectra.

#### Pure copper results

Reflectance data for a fresh copper film are shown in Fig.4.8. (The reflectance of aged films was lower by several percent in the interband absorption region.) The  $\epsilon_2$  spectrum obtained by Kramers-Kronig transform from this reflectance data is shown below it.

A typical piezoreflectance spectrum for polarisation parallel and perpendicular to the strain axis denoted by  $\parallel$  and  $\perp$  is shown in Fig.4.9. Note that the size of the dip at the threshold near 2.2 eV is almost identical for each polarisation but for perpendicular polarisation the feature is centred about 0.01 eV lower in energy.

Comparison was made with Gerhardt's (1967) single crystal  $\frac{\Delta R}{R}/e(Q_{ij})$  spectra, shown in Fig.4.10. This gives a check on the compatibility of our results, but also aids in the interpretation of the alloy results by identifying the dominant  $Q_{ij}$  contributing to the film response.

As remarked in Chapter 2.4 the results of any piezoreflectance experiment in polycrystalline samples should be a linear combination of the single crystal coefficients. We have attempted to find combinations of Gerhardt's  $Q_{ij}$  which match our  $\parallel$  and  $\perp$   $\frac{\Delta R}{R}$  spectra. The best fit to a typical pair of piezoreflectance spectra is shown in Fig.4.10b; the combinations of  $Q_{ij}$  shown by the squares are listed below along with those from the calculation of the piezo-optic response of films of pure (001) and (111) textures reported in the appendices.

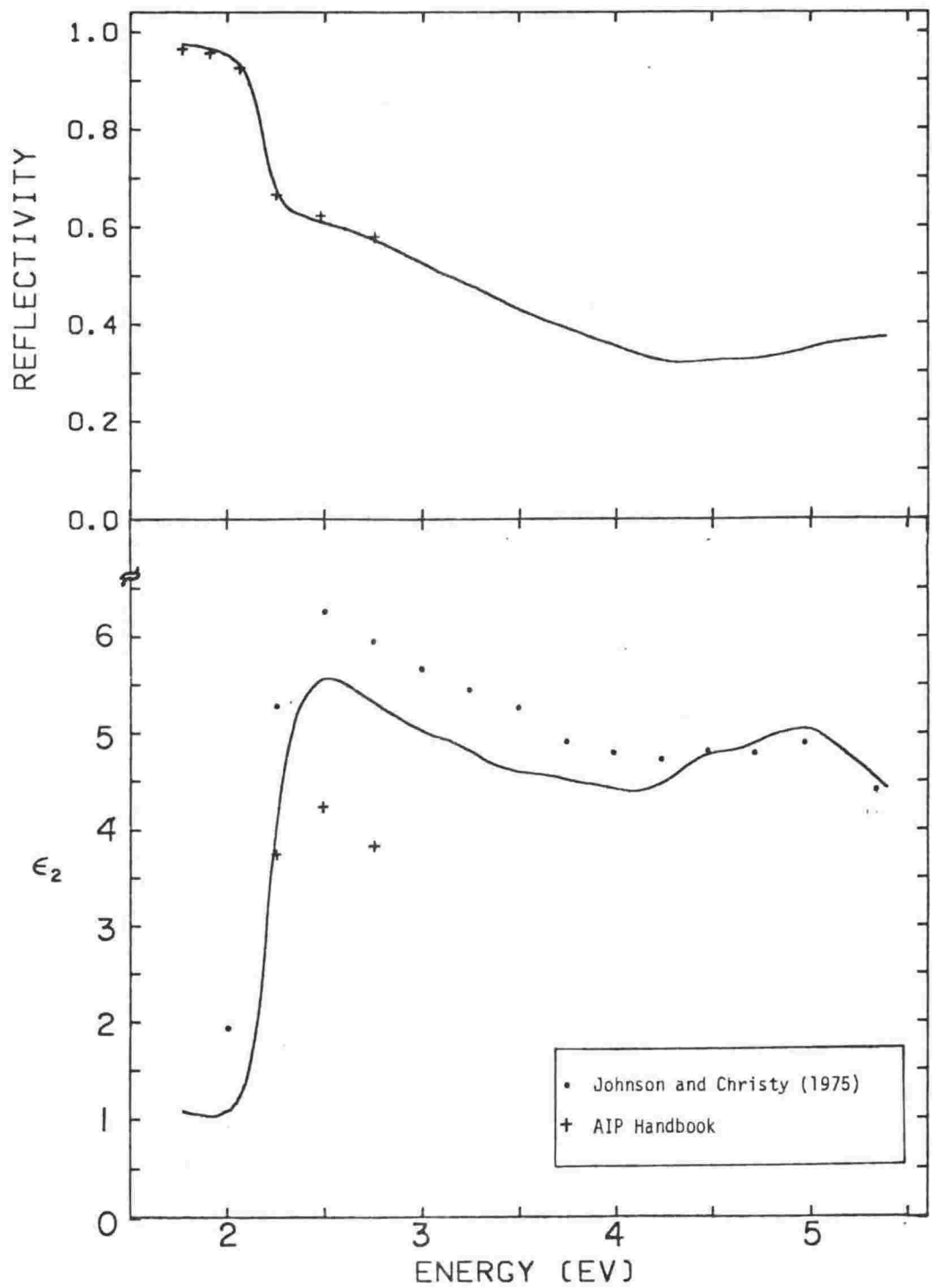


Fig. 4.8 Measured reflectance and  $\epsilon_2$  spectra from Kramers-Kronig integration for a pure copper film. Some data from the literature is shown for comparison.

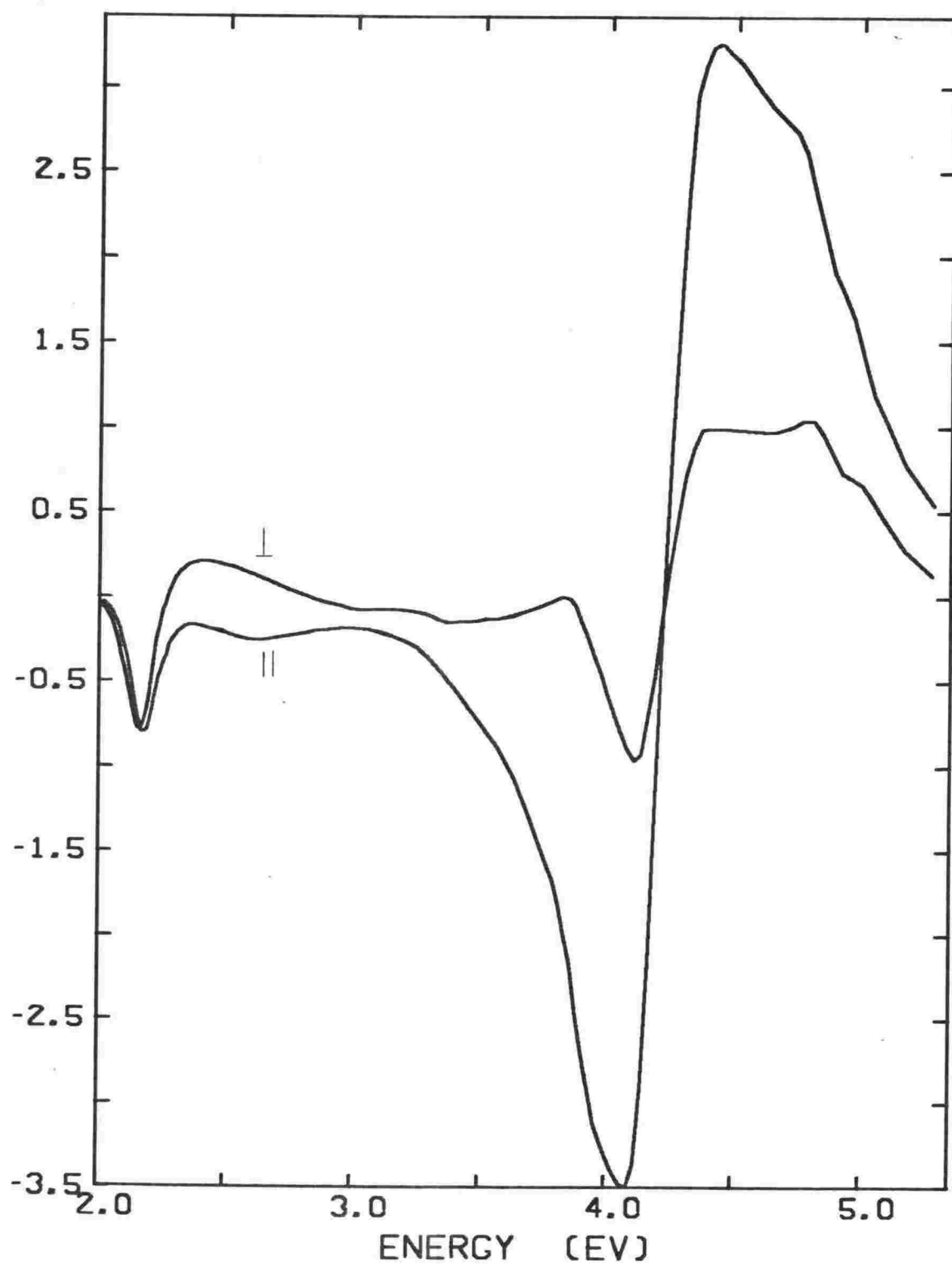


Fig.4.9 Strain normalised piezoreflectance spectra for a pure copper film for light polarised  $\parallel$  and  $\perp$  to the strain axis.



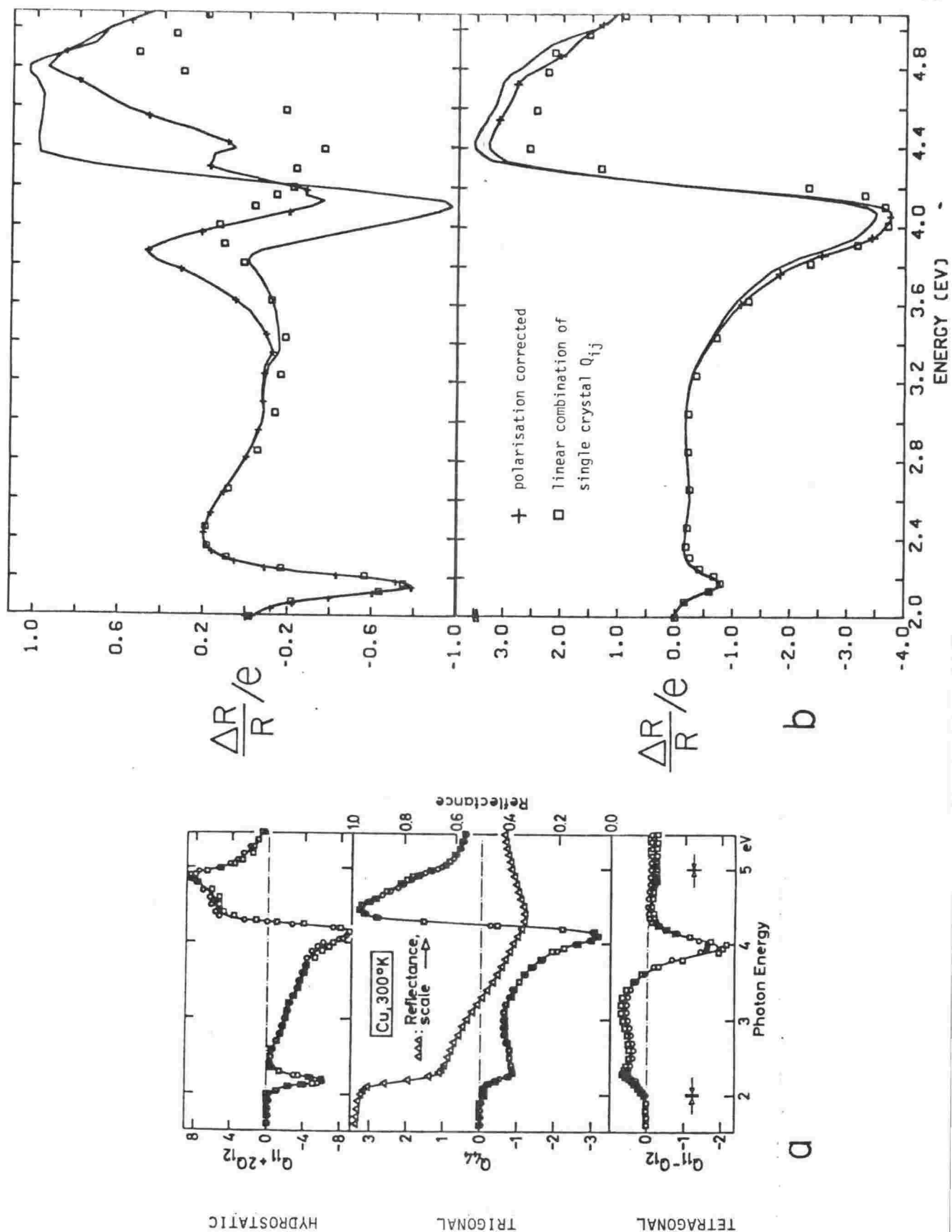


Fig. 4.10 Comparison between single crystal piezoreflectance results and present results for vacuum-deposited pure copper film.

(a) Single crystal symmetry combination of  $Q_{ij}$  components (Gerhardt, 1968).

(b) Film piezoreflectance results with and without polarisation correction compared with the linear combination of single crystal  $Q_{ij}$  referred to in the text.

		<u>Q<sub>hydrostatic</sub></u>	<u>Q<sub>trigonal</sub></u>	<u>Q<sub>tetragonal</sub></u>
$\frac{\Delta R}{R} \parallel$	Experiment:	0.135	0.55	0.60
	(001) :	0.075	0.15	0.63
	(111) :	0.17	0.24	0.12
$\frac{\Delta R}{R} \perp$	Experiment:	0.135	-0.38	0.17
	(001) :	0.075	-0.15	0.048
	(111) :	0.17	-0.001	-0.12

The fit in Fig.4.10b is good for the parallel spectrum except above 4.3 eV but poor for the perpendicular spectrum, whether polarisation - corrected or not, in the ultraviolet. This is probably due to a combination of inaccuracy in the data required for the polarisation correction and errors in the  $Q_{ij}$  data read from Gerhardt's figures being accentuated in subtraction. The point is not of much importance since it emerged, in any case, that very little information about transitions in the ultraviolet could be obtained from the perpendicular polarisation spectra for the alloys, because of the degree of cancellation of the hydrostatic and trigonal strain responses. Because the polarisation correction did not help either to resolve the incompatibility of the  $Q_{ij}$  and the  $\perp$  spectrum in the ultraviolet or to extract further information from the alloy spectra it was decided not to apply it - this did not affect the precision with which transition energies could be determined.

For different pure copper samples the coefficient for the hydrostatic contribution ranged from 0.11 to 0.14 and the shear contributions varied over a similar range. There seemed to be no correlation with variations in the relative (111) texture of the samples measured by X-ray diffraction. Comparison with the results of the calculation of the response of films of pure (001) and (111) texture shows some points of agreement: the magnitude of the experimental hydrostatic component is intermediate between the two pure textures and the signs of the shear responses are consistent with experiment. (Positive for parallel polarisa-

ation, negative or small for perpendicular polarisation.) However the magnitude of the experimental trigonal component is larger than that expected from a mixture of the two pure textures. This might be due to crystallites of orientation other than (001) or (111) or to the assumption of constant strain in the film being invalid. It appears that aspects of film structure not explored by the X-ray measurements - for example, the relative abundance of higher order crystallite orientations - may be important in determining the piezo-optic response.

The strain normalised  $(\hbar\omega)^2\Delta\epsilon_2$  spectra obtained by Kramers-Kronig transformation of the piezo-reflectance data of Fig.4.9 is shown in Fig.4.11. The origin of the major spectral features has been fully discussed in Chapter 2, Sections 3 and 4, and summarised in Table 2.4. Three features will figure prominently in the following discussion:

- 1) The d band threshold - the peak in both spectra at about 2.2 eV which is mainly a response to hydrostatic strain. (Denoted by  $E_d^U \rightarrow E_F$ .)
- 2) The interconduction band threshold - the peak at 4.2 eV most prominent in the parallel polarisation spectrum due largely to trigonal shear response. ( $E_F \rightarrow Q_+$ )
- 3) The interconduction band  $M_2$  singularity - the negative peak at 5.0 eV. ( $L_2' \rightarrow L_1^U$ )

Also evident is a negative contribution in the parallel polarisation spectrum between 3 and 4 eV contributed by the tetragonal shear response of the  $X_4'-X_5$   $M_1$  critical point.

#### Line fitting

Combinations of lineshapes of the functional form  $F(X)$  introduced in 2.4 (page 33) were fitted to the pure Cu and alloy  $(\hbar\omega)^2\Delta\epsilon_2$  data to determine the energies of the critical points. A fit to the interconduction band structure for a pure Cu sample using the expression

$$(\hbar\omega)^2\Delta\epsilon_2/e = AF\left(\frac{\hbar\omega - E_t}{\Gamma_t}\right) - BF\left(\frac{\hbar\omega - E_s}{\Gamma_s}\right)$$

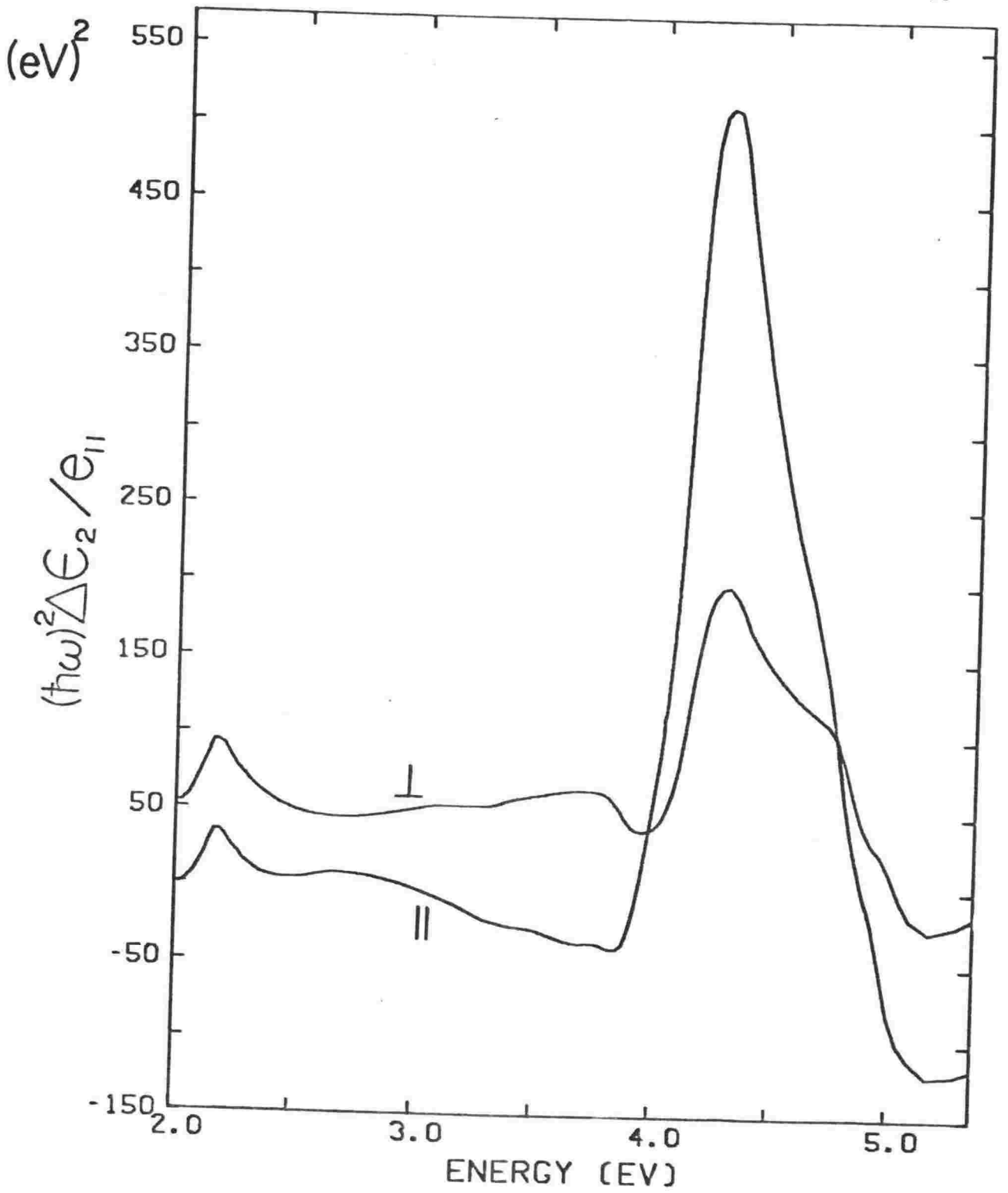


Fig.4.11  $(\hbar\omega)^2 \Delta\epsilon_2 / e$  spectra for pure copper film. The spectrum for light polarised  $\perp$  to the strain axis is displaced upwards by one division.

is shown in Fig.4.12. The singular energies obtained for pure Cu were:

$$E_t = Q_+ - E_F = 4.22 \pm 0.02 \text{ eV}$$

$$E_s = L_1^U - L_2' = 5.05 \pm 0.1 \text{ eV}$$

$$(\Gamma_t \sim 0.13 \text{ eV}, \Gamma_s \sim 0.25 \text{ eV})$$

The uncertainty quoted for the threshold value is the range of values found for different pure copper samples, the fitting uncertainty was closer to  $\pm 0.01$  eV. It should be compared with Chen and Segall's (1976) estimate of  $4.26 \pm 0.02$  eV obtained by a linefitting of the single crystal trigonal spectrum. The discrepancy is unlikely to be due to competition from the trigonal or hydrostatic responses in the film spectrum - a fit to the difference spectrum  $(\hbar\omega)^2(\Delta\epsilon_2^{\parallel} - \Delta\epsilon_2^{\perp})$  - in which the hydrostatic component should be cancelled gave an identical value.

The poor fit below 4 eV is due to the  $M_1$  critical point at X. The poor fit between about 4.4 and 5.0 eV was also found by Chen and Segall who attributed it to a change in the curvature of the conduction band across the Fermi surface neck which causes the joint density of states to begin to level off above the threshold - uncertainty on this point limits the precision with which  $L_1^U - L_2'$  can be determined. If a theoretically based parametrised description of the K-dependence of the conduction band curvature at L was available the fit might be improved and additional band structure information inferred from the results.

The d band threshold was fitted (Fig.4.13) by a variation on the expression used for the interconduction band threshold:  $(\hbar\omega)^2\Delta\epsilon_2/e = CF(X) - DG(X)$ .

$$G(X) = [(X^2 + 1)^{\frac{1}{2}} + X]^{\frac{1}{2}},$$

a broadened square root singularity, approximates the response expected from strain modulation of the effective band mass rather than the energy gap and may also simulate the effect of K-dependence of the effective mass. Because

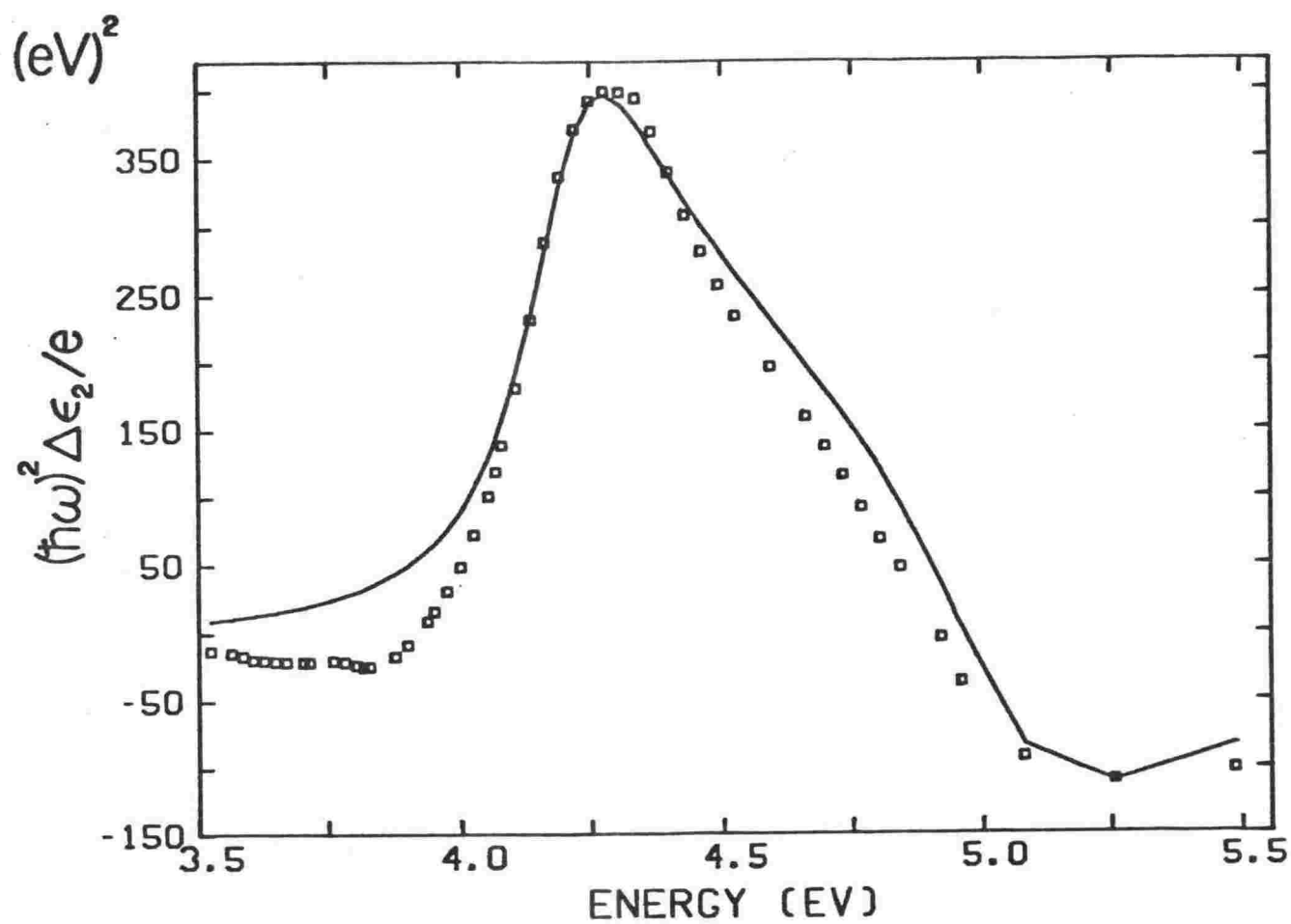


Fig.4.12 Line fit to interconduction band piezo-optic structure for a pure copper film. Solid line: theoretical lineshape, squares: experimental data.

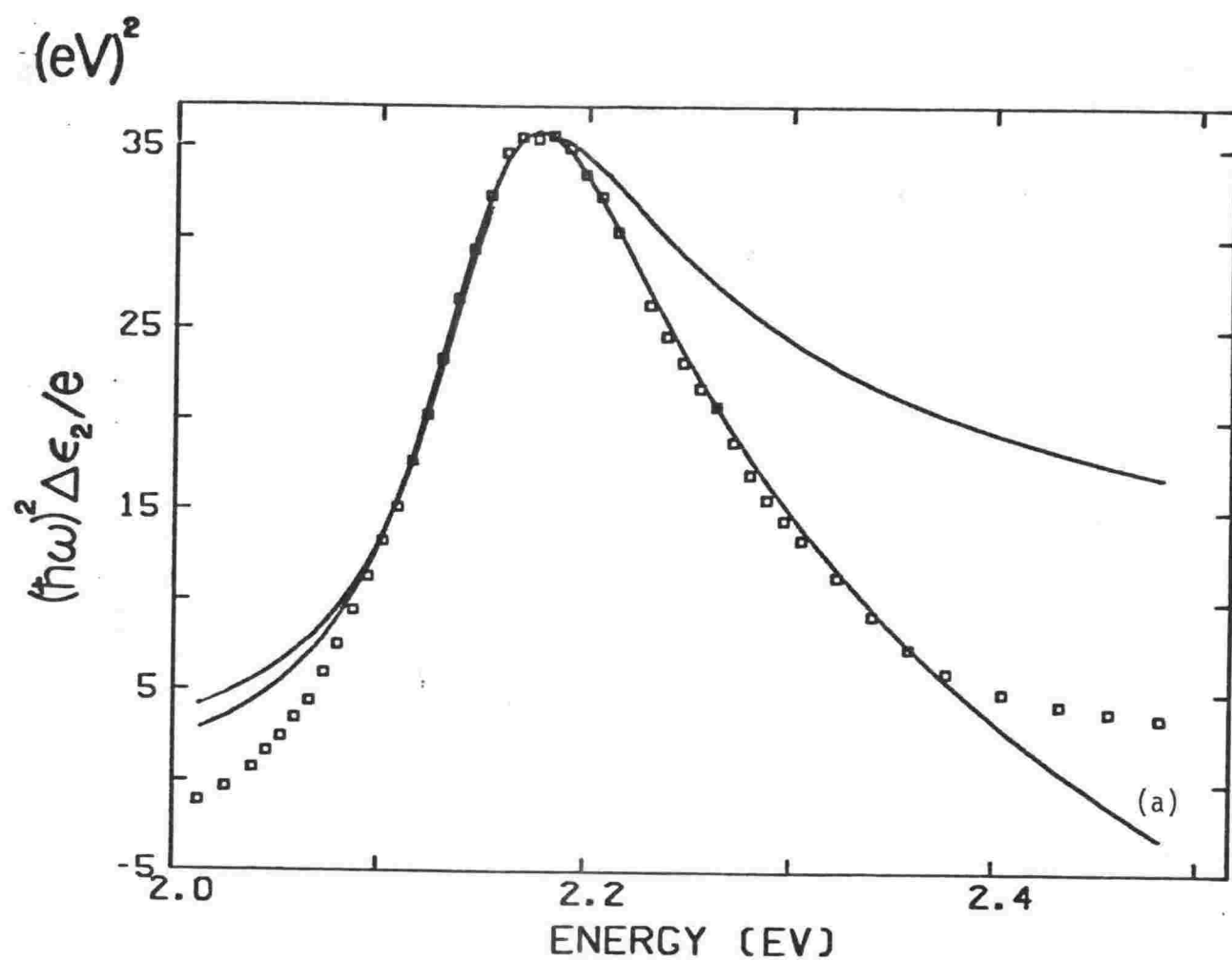


Fig.4.13 Line fit to d band threshold piezo-optic structure for a pure copper film. Solid line: theoretical lineshape, squares: experimental data. Lineshape (a) includes a square root contribution ( see text ).

the d band  $\rightarrow$  Fermi level threshold transitions are not localised in  $\underline{k}$ -space, there is no reason for confidence in the theoretical expression but the fit is actually remarkably good. The singular energies obtained were 2.152 eV for parallel polarisation and 2.141 eV for perpendicular polarisation with uncertainty about  $\pm 0.003$  eV.

#### Alloy results

Representative strain normalised  $\frac{\Delta R}{R}$  and  $(\hbar\omega)^2\Delta\epsilon_2$  spectra for alloys of copper with Zn, Ga, Al, In and Ge are presented in Figs. 4.14 (a - e). The general trend is that the d band threshold feature shifts slowly to higher energy and the interconduction band structure shifts rapidly to lower energy. Despite the broadening and general reduction in the magnitude of the response (particularly evident in the interconduction band feature) the structure is sufficiently like its counterpart in the pure copper spectra that the assignment of critical energies is in most cases straightforward.

The  $\perp$  spectrum is used to determine the d band threshold energy because the partial cancellation of the hydrostatic and trigonal responses to transitions near L for this polarisation means that the problem of overlapping by the interconduction band response in concentrated alloys is less severe. Compare, for example, the  $\parallel$  and  $\perp$   $(\hbar\omega)^2\Delta\epsilon_2$  spectra for the 31.2 at% Zn alloy where the d band threshold response can still be plainly seen superimposed on the high energy side of the interconduction band threshold response. Because the d band threshold features in the  $\parallel$  and  $\perp$  spectra contain shear strain contributions of opposite sign the threshold energy for pure hydrostatic strain would be intermediate between the apparent threshold energies for  $\parallel$  and  $\perp$  polarisation. Nonetheless the results from low concentration alloys (in which overlap does not occur) show that the  $\parallel$  and  $\perp$  threshold energies maintain a constant separation of just 0.01 eV as the threshold energy rises so the  $\perp$  spectrum does give a valid measure of shifts in the threshold energy.

The  $X_5 \rightarrow X_4'$  feature visible in the pure copper



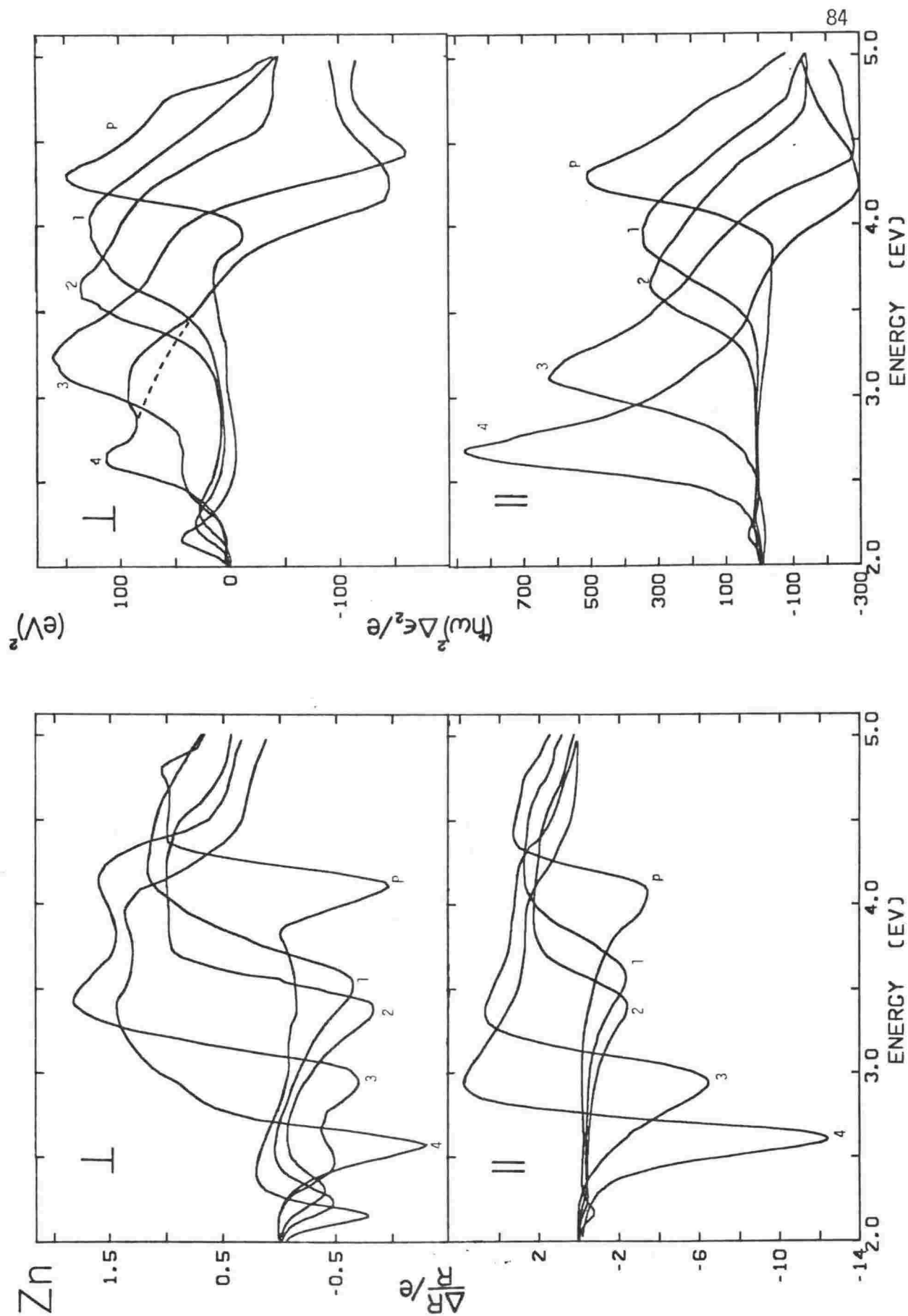


Fig.4.14a Piezoreflectance results for Cu(Zn) alloys.

p: pure Cu, 1: 10.07 at%, 2: 14.0 at%, 3: 21.3 at%, 4: 31.2 at%

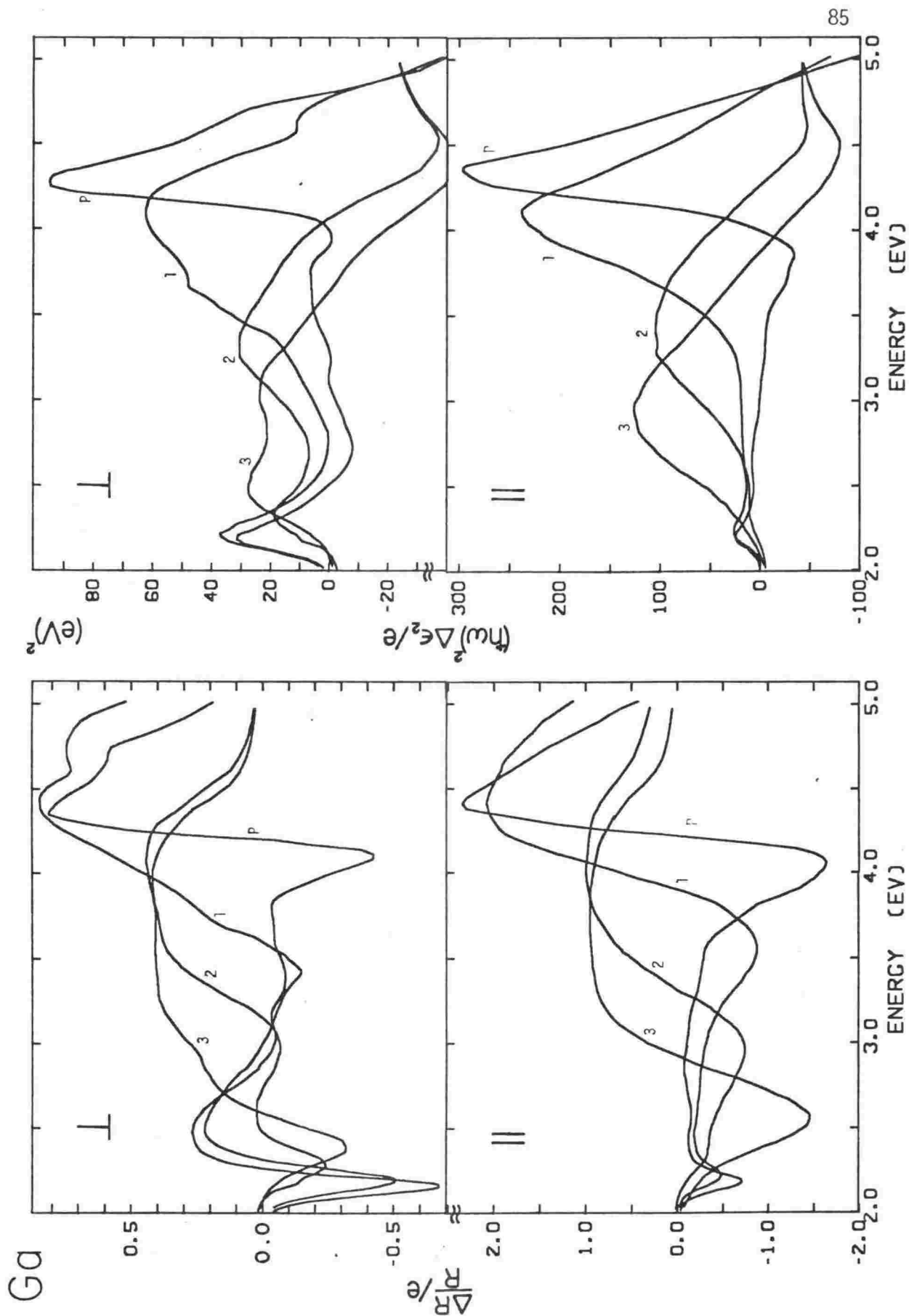


Fig.4.14b Piezoreflectance results for Cu(Ga) alloys.

p: pure Cu, 1: 2.31 at%, 2: 7.43 at%, 3: 12.65 at%

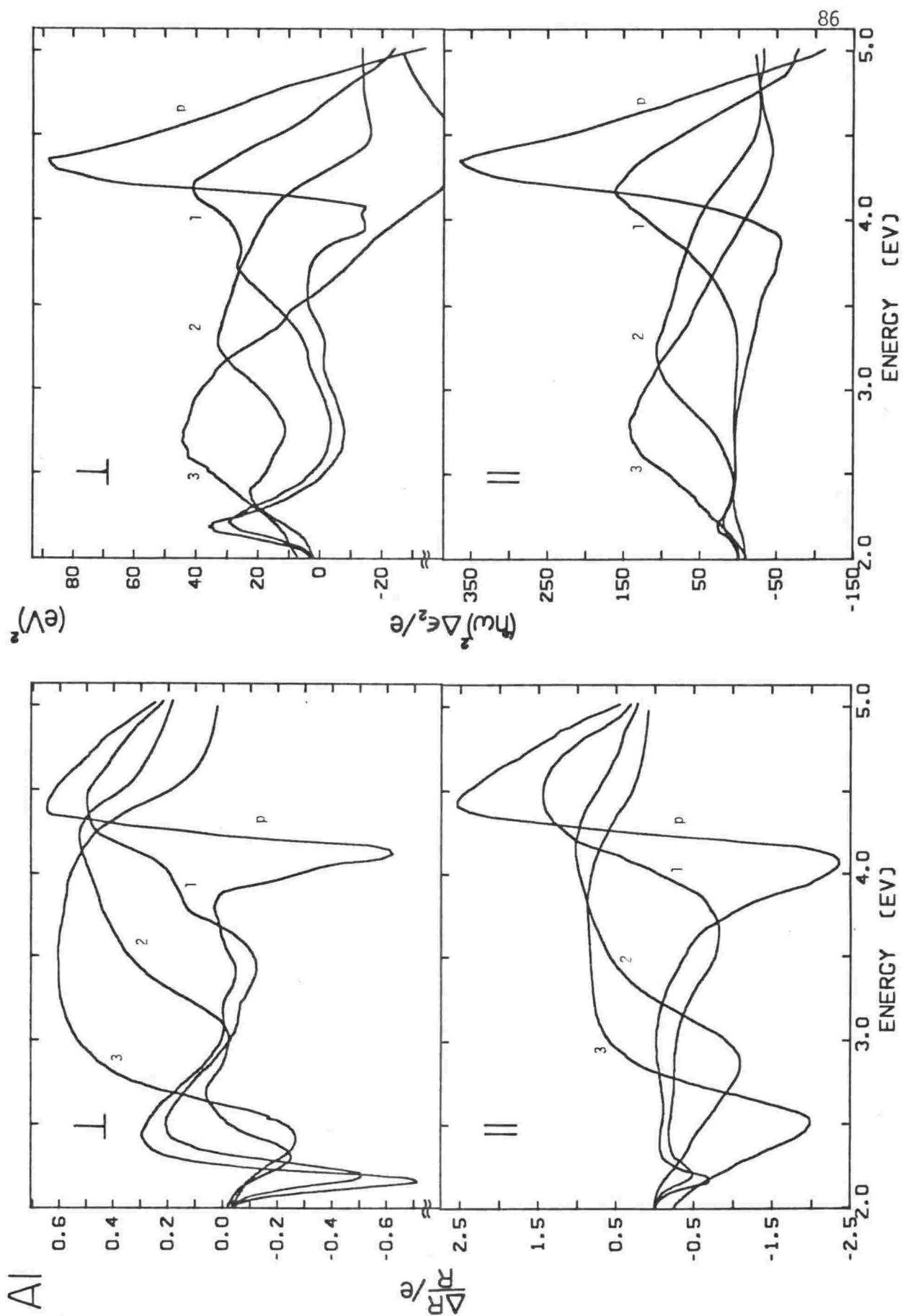


Fig.4.14c Piezoreflectance results for Cu(Al) alloys.

p: pure Cu, 1: 1.35 at%, 2: 6.65 at%, 3: 13.55 at%

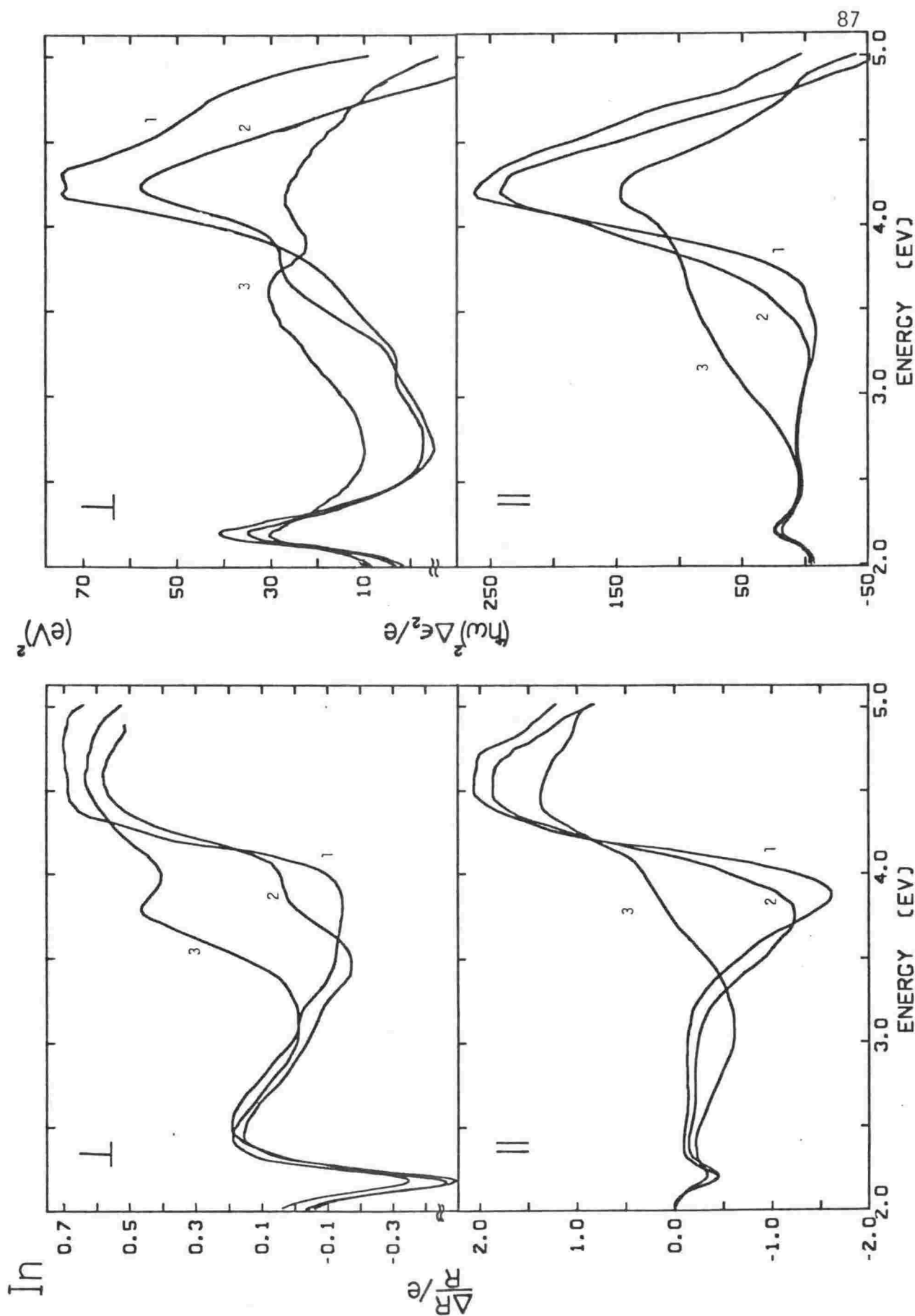


Fig.4-14d Piezoreflectance results for Cu(In) alloys.

p: pure, 1: 0.4 at%, 2: 0.8 at%, 3: 1.25 at%

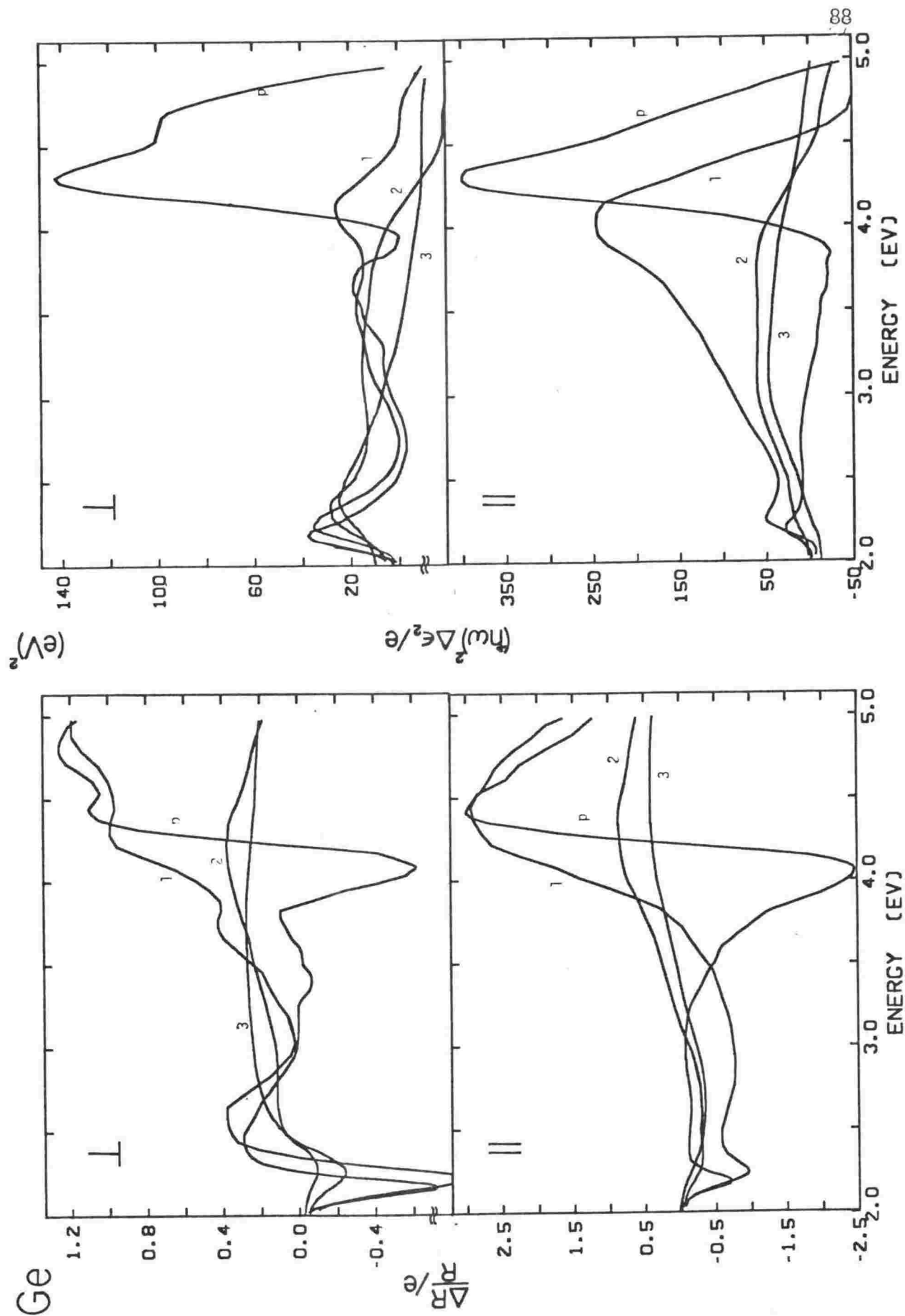


Fig.4.14e Piezoreflectance results for Cu(Ge) alloys.

p: pure Cu, 1: 3.42 at%, 2: 6.1 at%, 3: 9.1 at%

$\perp$  spectrum is rapidly obscured in the alloys; it is believed that the change in the spectra for dilute alloys ( $< 3$  at%), in particular a bulge which appears to develop at about 3.8 eV in  $\frac{\Delta R}{R} \perp$  and is very evident in the In alloys, simply reflects a change in the extent to which the single crystal components cancel as the positions of the features change. Its size was slightly reduced by annealing. A similar broad feature at about 3 eV seen in only the 1.25 at% In and 3.95 at% Al samples (which prevented accurate determination of the inter-conduction band threshold for these two alloys) appears to be an anomaly associated with very disordered unannealed films.

The most concentrated Zn samples showed a remarkable sensitivity to annealing - the main structure in  $\frac{\Delta R}{R} \parallel$  increased in the 31.2 at% alloy (initially annealed at 380°C) by some 300% following a second anneal (~480°C) which increased the crystal size determined by X-ray diffraction from about 400 to 1000 Å and doubled the (111) line intensity. The 21.3 at% alloy showed lesser increases. There was no shift in the threshold energy.

The interconduction band threshold in the Ge spectra is so rapidly damped that the critical energy could only be determined for the 3.4 at% alloy. This is in agreement with the rapid smearing of optical structure reported by Pells and Montgomery (1970) and Beaglehole and Wihl (1973).

Some examples of linefitting of the  $(\hbar\omega)^2 \Delta\epsilon_2$  spectra are shown in Fig.4.15. The inadequacy of parabolic modelling of the bands is particularly evident for the 31.2 at% Zn alloy where the  $M_0$  and  $M_2$  singularities have been fitted separately. In this case, of course, the Fermi surface neck has expanded somewhat so that the parabolic expansion is being extended to a greater distance from L.

The critical energies determined from the spectra are listed in Table 4.1. Blank entries indicate that the energy could not be determined because of

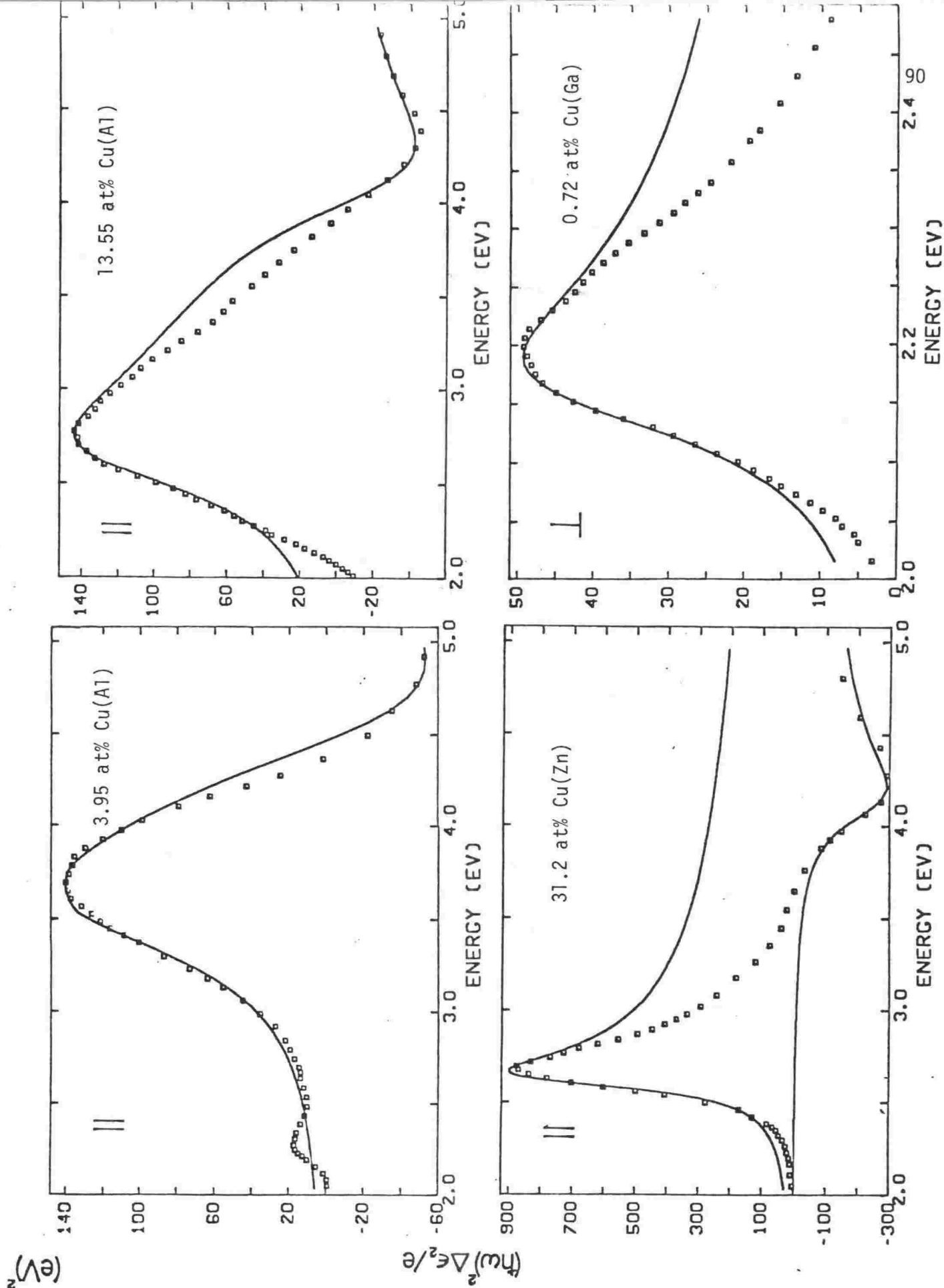


Fig.4.15 Examples of linefitting piezo-optic structure in alloys. Solid lines are the lineshape expressions on pages 78 and 80, squares are experimental data. The two interconduction band critical energies are fitted separately in the 31.2 at% Cu(Zn) alloy.

Table 4.1

## Alloy critical energies (eV)

	Concentration (at%)	Interband threshold $E_F - E_d^u$	Interconduction band threshold	$L_1^u - L_2'$
			$Q_+ - E_F$	
Pure Cu		2.141	4.22	$5.05 \pm 0.1$
Z = 1				
Cu(Zn)	5.65	2.174	4.01	$4.9 \pm 0.1$
	10.07	2.205	3.82	4.8
	12.07	2.230	3.65	4.72
	14.00	2.260	3.56	4.62
	21.3	2.39	3.05	4.34
	31.2	$3.05 \pm 0.05$	2.62	4.11
Z = 2				
Cu(Ga)	0.72	2.151	4.125	
	1.08	2.157	4.06	
	2.31	2.167	3.93	
	5.10	2.213	3.54	$4.62 \pm 0.07$
	7.43	2.262	3.21	$4.49 \pm 0.07$
	12.65	2.375	2.73	4.32
Cu(Al)	1.06	2.160	4.07	
	1.35	2.161	4.01	
	2.8	2.175		
	3.95	2.208	3.46	$4.67 \pm 0.1$
	6.65	2.295	3.03	$4.46 \pm 0.1$
	13.55	$2.44 \pm 0.05^*$	2.58	4.22
Cu(In)	0.4	2.151	4.13	
	0.8	2.151	4.09	
	1.25	2.156	4.03	
Z = 3				
Cu(Ge)	3.42	2.198	3.83	
	6.1	2.246		
	9.1	2.309		
Uncertainty <sup>†</sup>	$\pm 0.15$	$\pm 0.005$	$\pm 0.02$	$\pm 0.05$

\*Lower limit determined from  $\epsilon_2$  data.

<sup>†</sup>Some exceptions are indicated for spectra affected by broadening, overlap, uncertainty in extrapolations etc.



overlap by other features, broadening, and uncertainties due to extrapolation at the high energy limit. The data are graphically summarised in Figs.4.16 and 4.17.

#### Comparison with other optical results

In order to establish the extent to which the present results are consistent with those of previous studies using mainly static optical techniques it is relevant to compare:

- 1) the procedures used by different workers to

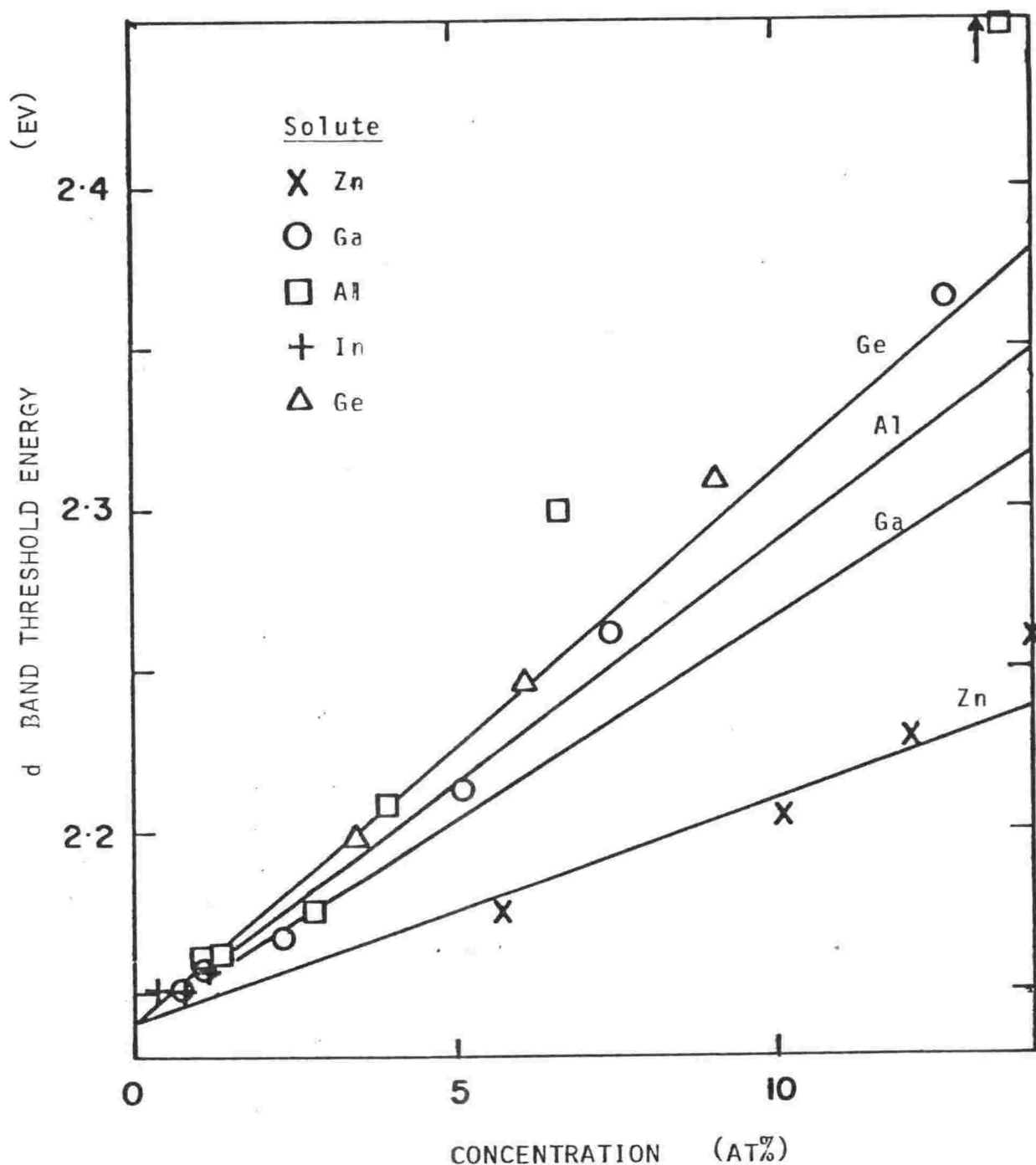


Fig. 4.16 Critical energy for d band threshold transitions as a function of alloy composition. Results for two more concentrated Zn alloys are not included. The lines represent estimates of the rate of shift of the threshold in the low concentration limit.

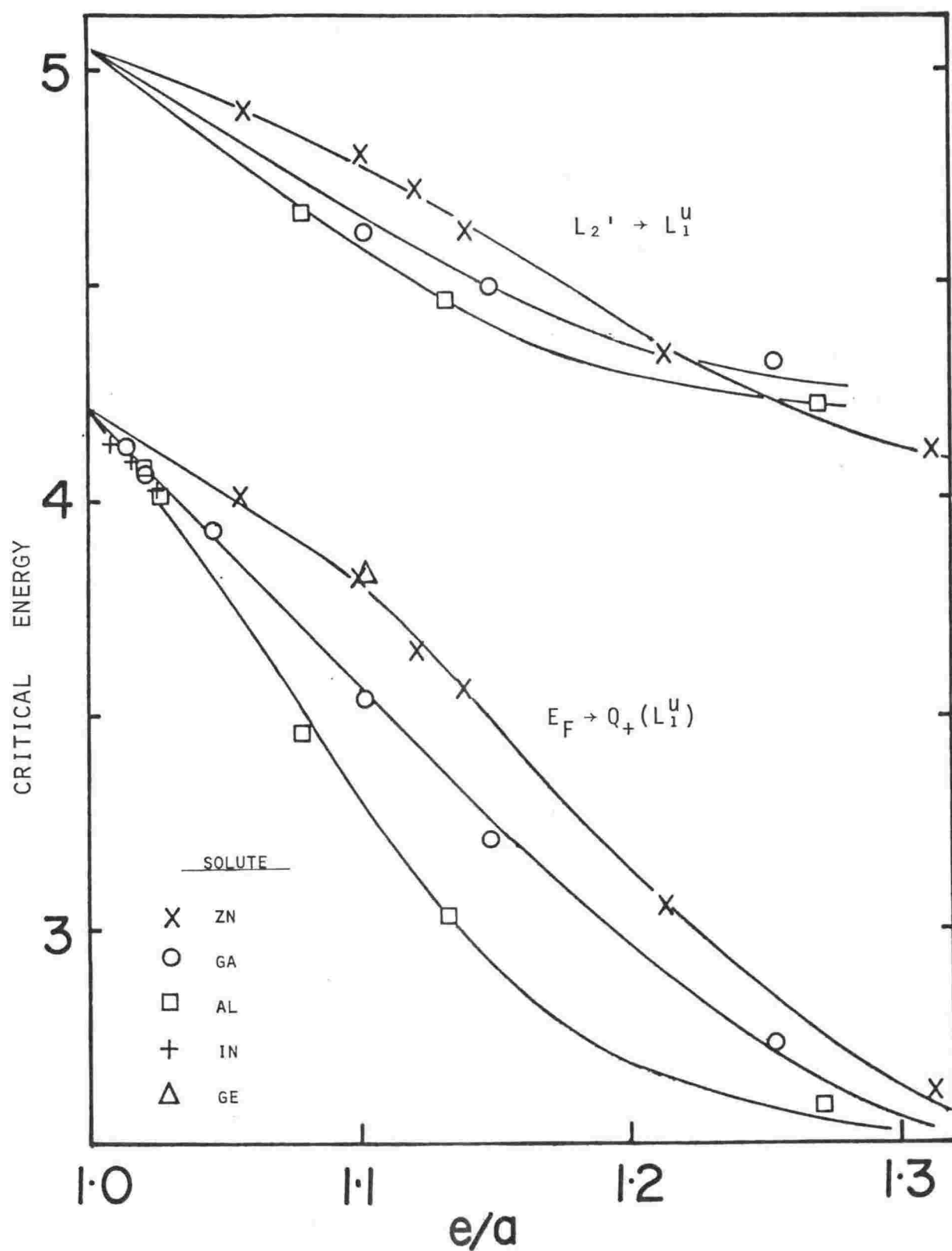


Fig. 4.17 Critical energies for interconduction band transitions  $E_F \rightarrow Q_+(L_1^u)$  and  $L_2' \rightarrow L_1^u$  plotted against electron per atom ratio for the alloys ( $e/a = 1 + cZ$ ).

It is apparent that there is a considerable range in the estimated threshold energy which reflects the different approximations of the procedures used to define it. In this work the d band threshold has been determined from the  $\epsilon_2$  spectra (using the fact that the threshold is a Fermi surface singularity:  $(\hbar\omega)^2 \epsilon_2 \propto (\hbar\omega - E_c)^{3/2}$  before broadening (Chapter 2.3) - some examples are shown in Fig.4.18) as well as by linefitting the piezoreflectance  $(\hbar\omega)^2 \Delta\epsilon_2$ . The difference between these two estimates ( $\epsilon_2$  and average of  $(\hbar\omega)^2 \Delta\epsilon_2$  || and  $\perp$  values - see page 83) is probably due to the approximation of parabolic bands - the  $((\hbar\omega)^2 \epsilon_2)^2$  plot is only linear to about 0.1 eV above the threshold. Although all the linefitting expressions involve the same approximations, piezoreflectance does have the great advantage of high resolution because it has a sharp threshold feature with little background structure.

The same remarks hold for the interconduction band critical energies except that the advantage in resolution of piezoreflectance is even greater because linefitting of  $\epsilon_2$  is out of the question. Broadening and a background of other interband absorption mean that the threshold is normally defined, if at all, by the point of maximum slope in  $\epsilon_2$ .

2) Comparison of present  $\epsilon_2$  and  $(\hbar\omega)^2 \Delta\epsilon_2$  results: The d band threshold determined by the extrapolation method described above generally shifted on alloying by the same amount as the piezoreflectance threshold. Its estimated uncertainty was however roughly twice as large. A number of  $\epsilon_2$  spectra are shown in Fig.4.19 with all the critical energies determined by piezoreflectance indicated. The interconduction band threshold in  $\epsilon_2$  becomes more difficult to determine with strongly scattering impurities but where it can be clearly identified the two methods are in reasonable agreement. The  $L_1^U - L_2'$  critical point is virtually impossible to detect in  $\epsilon_2$  spectra even with the hindsight of the piezoreflectance results.

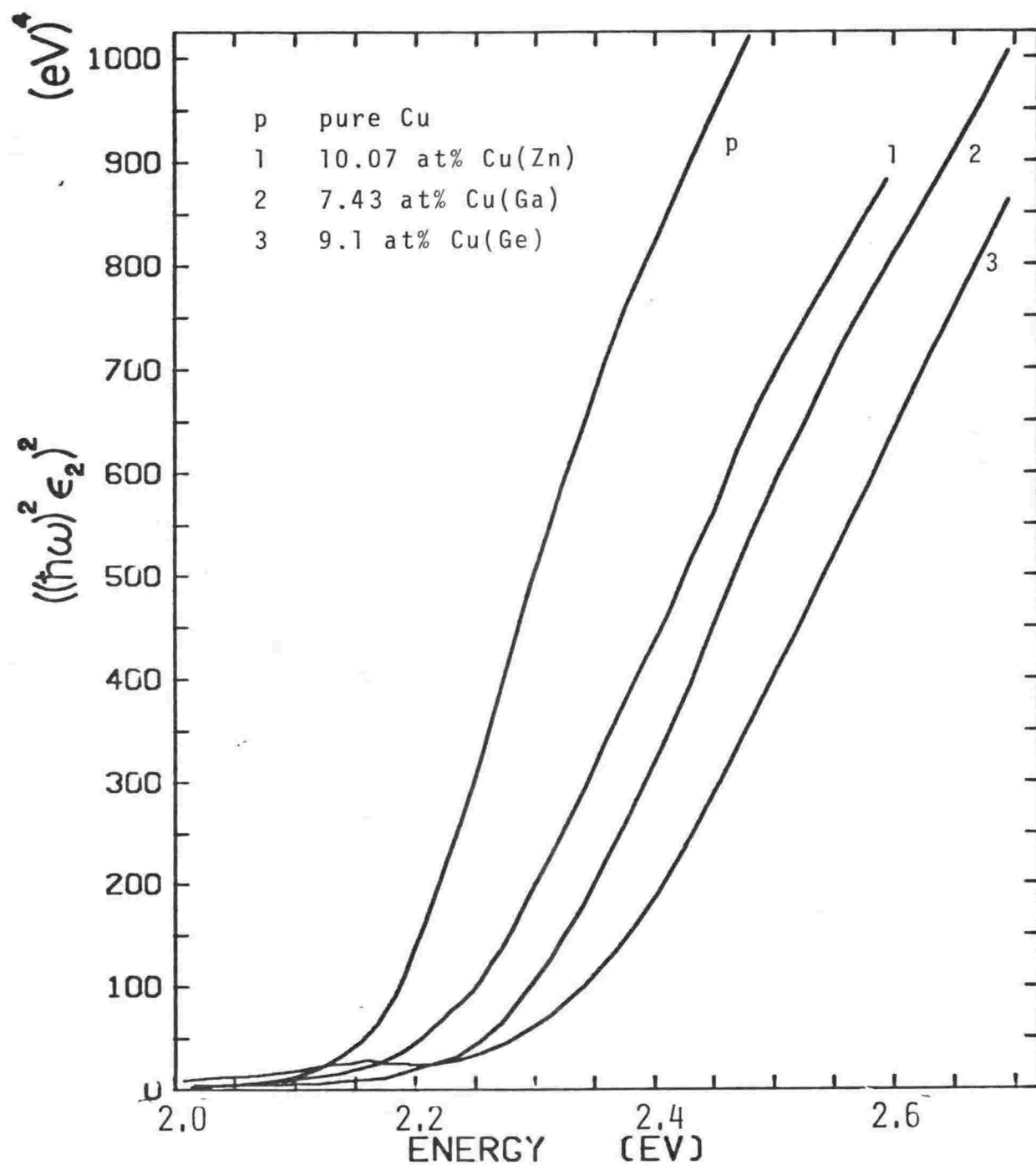


Fig.4.18 Examples of determination of d band threshold from static optical results. An extrapolation of the intraband contribution has been subtracted. The intercept of the extrapolation of the straight line portion of the function gives the critical energy.

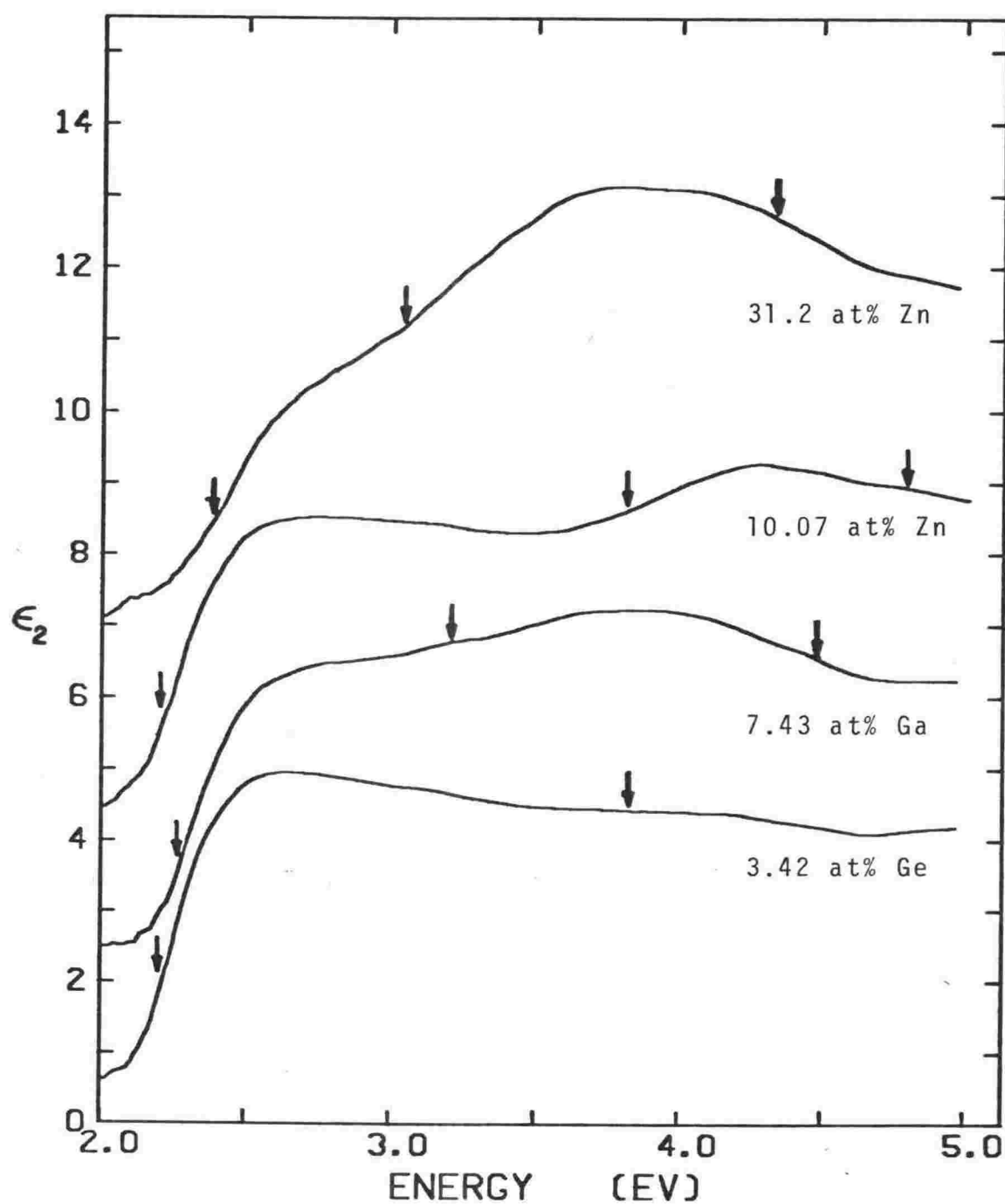


Fig.4.19 Examples of alloy  $\epsilon_2$  spectra with critical energies determined from piezoreflectance results marked. The critical energies are, from left to right, the d band threshold, the interconduction band threshold, and the  $L_2' \rightarrow L_1^U$  singularity.

3) Comparison with other alloy results: The results of optical studies of the same alloy systems by other workers are summarised in Figs. 4.20 and 4.21. The difficulties of optical sample preparation, variations in optical technique and, probably most important, differing procedures for determining threshold energies, all contribute to the differences in the findings.

For the d band threshold, data of high precision has been obtained by Nastasi-Andrews and Hummel (1977) (abbrev. NH) by linefitting differential reflectance results for pairs of samples differing slightly in concentration. Biondi and Rayne (1959), Rayne (1961) and Pells and Montgomery (1970) determined the threshold more arbitrarily from the point of maximum slope of the absorption or an extrapolation from it. The piezoreflectance results are generally in fair agreement with those of NH with the exception of the Cu(Zn) results. This discrepancy is genuine and cannot be attributed to some fundamental difference in the origin of the effective threshold determined by piezoreflectance and static optical studies because the  $(\hbar\omega)^2\Delta\epsilon_2$  and the static  $\epsilon_2$  results of the present study are all in agreement, and furthermore the maximum fractional change in reflectance at the threshold produced by alloying (i.e. the size of the threshold peak in the differential reflectance spectrum) is  $-17.10^{-3}/\text{at}\%$  according to NH and  $-9.10^{-3}/\text{at}\%$  according to our differential reflectance measurements.

The interconduction band threshold results disagree quantitatively with those of NH who in this case have arbitrarily identified a minimum in the differential reflectance spectra with interconduction band transitions. The close resemblance to the piezoreflectance spectra suggest the zero crossing would have been a better choice. Furthermore their transition energies for different impurities extrapolate to different values at zero concentration - they do not coincide with alloy

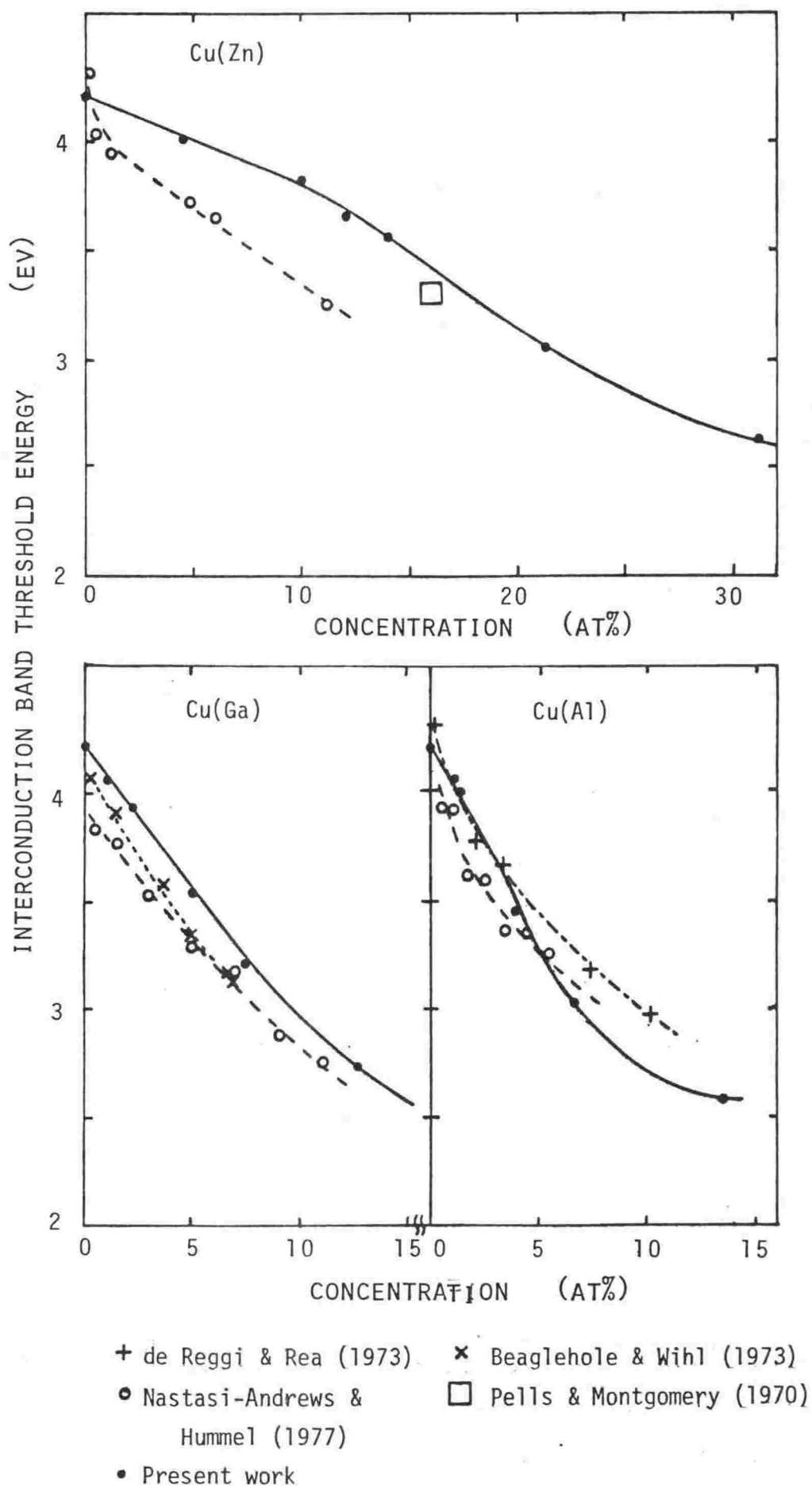


Fig.4.20 Comparison with other optical work :interconduction band threshold.



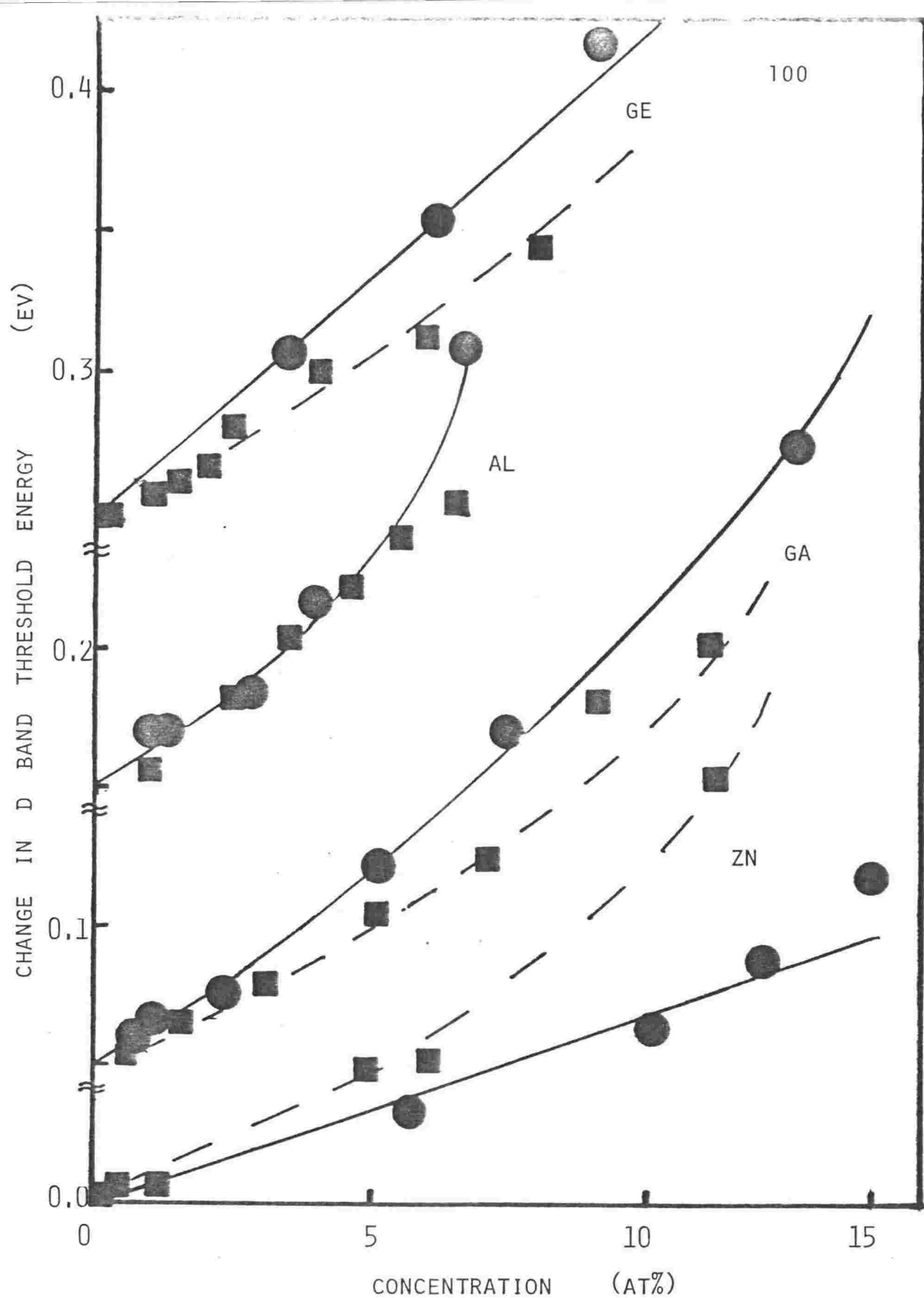


Fig.4.21 Comparison with other optical work ; changes in the d band threshold energy from work of Nastasi-Andrews and Hummel (1977) (squares) and results of present study (circles). The results for different solutes have been displaced from the origin for clarity.

band gaps and are not directly comparable with the results of other optical studies. Agreement between the present data and those of other studies based on absorption or  $\epsilon_2$  spectra is imperfect. Inspection of the Pells and Montgomery data gives threshold energies for Zn and Ga alloys close to the piezo-reflectance estimates. It is contended that the discrepancies are likely to be due to the extreme difficulty of estimating the threshold onset from  $\epsilon_2$  curves.

## 5 DISCUSSION

### 5.1 d bands

Because the Fermi level is stationary in the dilute concentration limit (Chapter 2.2), any change of energy of the d band threshold at low concentrations must be due to shifts of the upper d band levels, apart from a contribution from the lattice expansion caused by alloying.

The effect of lattice expansion can be estimated from the hydrostatic deformation potential for the threshold in pure copper obtained by Gerhardt (1967) from piezo-reflectance measurements (Table 2.2) and alloy lattice constant data (Pearson, 1964) in Table 3.3 by assuming

$$\frac{\Delta E}{C} = \frac{\Delta E}{\Delta V/V} \times \frac{\Delta V/V}{C}$$

(Beaglehole & Erlbach, 1972). The lattice expansion in an alloy is not uniform - the region of the host lattice immediately surrounding an impurity will be compressed and considerably distorted - so the effect on the d bands may be overestimated. The threshold shift rates and estimated shifts associated with lattice expansion are given in Table 5.1.

The corrected shift rates (i.e. those that would be observed in the absence of lattice expansion) indicate a decrease in energy of the states at the top of the d band which may be caused by a combination of: 1) narrowing of the d band due to the reduced mean Cu d-d overlap (Beeby, 1964); 2) a shift in the mean energy of the d band caused by (i) screening charge transfer between impurity and host sites affecting the atomic potential on copper sites close to impurities (Levin & Ehrenreich, 1971) (ii) interaction between the host and impurity d bands forcing them apart in energy (Nilsson, 1970). Expressing these additive shifts as

$$\Delta E_d^U = \delta E_n + \delta E_{sc} + \delta E_{dd}' ,$$

we now discuss each contribution in turn.

Table 5.1  $E_d^U \rightarrow E_F$  - interband threshold shift rates in the low concentration limit

<u>Solute</u>	<u>Shift rate</u> ( $10^{-3}$ eV at% $^{-1}$ )		
	<u>Experiment</u>	<u>Lattice</u>	<u>Adjusted for lattice expansion</u>
Zn	$6 \pm 1$	-1.9	8
Ga	$12.5 \pm 2$	-2.5	15
Al	$14 \pm 2$	-2.2	16
In	$15 \pm 5$	-8.6	24
Ge	$17 \pm 2$	-3.7	21

- 1) The narrowing of the d band,  $\delta E_n$  is a consequence only of the dilution of the host by substitution of atoms without d states in the same energy range - it should be independent of the impurity valence. The width of the d band is the result of roughly additive broadening due to d-d and s-d interactions:

$$W = W_{dd} + W_{sd}.$$

$W_{dd}$  accounts for about 2.8 eV of the total 3.5 eV d band width in Cu (Mueller, 1967).

According to the resonance theory of the d band (Heine, 1967),  $W_{dd}$  is proportional to the probability of tunnelling to a d state on a like atom so that  $W_{dd}(\text{alloy}) = (1 - c)W_{dd}(\text{pure})$ . In passing one notes that the calculations of Velicky et al (1968) imply a  $(1 - c)^{1/2}$  variation of the host bandwidth but explicit calculations of alloy electronic structure (Bansil et al, 1974; Soven, 1966) exhibit narrowing

which varies closer to  $(1 - c)$ . Any changes in that part of the bandwidth due to s-d hybridisation would depend on the extent of charge transfer but would not figure in the experimental results because hybridisation does not affect the states associated with threshold transitions; it depresses the  $X_1^L$  and  $L_1^L$  levels at the bottom of the d band and raises the  $X_1^U$  and  $L_1^U$  levels in the upper conduction band (Mueller, 1967). If the narrowing is symmetrical one thus estimates that the top of the d band will drop at a rate  $\delta E_n/c = 0.014 \text{ eV at\%}^{-1}$  due to dilution of the d-d interaction.

- 2i) The increase in the mean energy of the d bands due to charge transfer from impurity sites to the surrounding host sites has been explored in a series of papers by Ehrenreich and co-workers using renormalised atom potentials (Chapter 2.1) to incorporate charge transfer. By this means, with a charge transfer of 0.13 eV from Zn to Cu sites, Bansil et al (1974) raised the top of the d band by 0.67 eV in a 30 at% Cu Zn alloy to produce agreement with optical results. It seems likely that renormalisation is an unsatisfactory representation of localised charge transfer, particularly in dilute alloys, and that it underestimates the charge transfer required for such substantial shifts because it assumes the transferred charge to be evenly shared over all host sites and to be symmetrically distributed within the host cells by renormalisation of the 4s wavefunction. In fact, screening theories (Chapter 2.2) suggest the charge perturbation is largely restricted to nearest neighbours of impurities and heavily concentrated in the section of the cell adjacent to the impurity cell. Consequently the bonding d orbital directed towards the impurity - dangling into the screening cloud - will be most affected. Painter (1978) in calculations on a Cu monolayer found that d bonds dangling outside the layer were destabilised

by about 2.1 eV relative to the bulk states while bonds within the layer were little affected. In an alloy, one expects that some of the bonding states lying low in energy in the d band density of states will be transferred to higher energies while the majority of states are relatively unperturbed, an effect which seems to be present in the density of states calculation of Moruzzi et al (1974) for the intermetallic compound Cu Zn. Thus charge transfer should produce a form of crystal field splitting rather than a bodily shift of the d bands. Nonetheless,  $E_d^U$  must change somewhat in response to charge transfer and on most grounds one expects the transfer to be from the polyvalent impurity to the host so that  $E_d^U$  increases ( $\delta E_{sc}$  is positive) and if anything, the amount of charge transfer and the size of  $\delta E_{sc}$  should increase with increasing impurity excess valence.

- 2ii) The interaction between the host and impurity d bands can be described by an application of the result of Velicky et al (1968) in the coherent potential approximation, valid for identical tight binding bands when the band separation is much greater than their width, according to which the Cu d bands are raised by

$$\delta E_{dd'} = c(E_d^{Cu} - E_d^{imp})^{-1} \int E^2 \rho(E) dE .$$

The integral gives the second moment  $\mu_2$  of the density of states about its centroid. In pure Cu one can estimate that  $\mu_2$  has a value about 5 eV<sup>2</sup>, taking 2.8 eV to be the bandwidth due only to dd interactions. The significance of the moment can be understood by comparison with the second-order perturbation expression (Schiff, 1968, p.247) in which  $\mu_2$  corresponds to

$$|\langle \psi_d | V_{dd'} | \psi_{d'} \rangle|^2$$

summed over the impurity d states (distinguished by the prime). In the theory of Velicky et al the model bands have identical widths implying that

$$V_{dd} = V_{dd'} = V_{d'd'}$$

so that the moment, as a measure of bandwidth, indirectly measures  $dd'$  interactions. However, for these alloys it is reasonable to assume rather that

$$V_{dd} > V_{dd'} > V_{d'd'}$$

and that  $V_{dd'}$  for  $\text{Cu}(\text{Zn}) > \text{Cu}(\text{Ga}) > \text{Cu}(\text{Ge})$  on the grounds of decreasing orbital overlap. The  $d$  band binding energies  $E_d$ , obtained from alloy photo-emission studies are listed below.

	Cu	Zn	Ga	Al	In	Ge
d band binding energy	3.1	9.7	18.6	-	17.1*	29.2 eV

Data from Norris and Williams (1978) and \*Riley et al (1976) [Ag(In)]

Except in the case of Al,  $\delta E_{dd'}$  will be positive -  $E_d^u$  increases as the bands are repelled - and roughly inversely proportional to  $Z$  (because the  $d$  band separation increases nearly linearly with  $Z$ ).

These estimates are compared with the experimental data in Fig.5.1. Line 1 represents narrowing and band repulsion contributions  $\delta E_n + \delta E_{dd'}$  with  $\delta E_n/c = -0.014 \text{ eV at}\%^{-1}$  and  $\mu_2 = 5 \text{ eV}^2$  as estimated before. The discrepancy between the experimental data and  $\delta E_n + \delta E_{dd'}$  is attributed to charge transfer (i.e.  $\delta E_{sc}$ ) and is uniformly negative, implying transfer of charge onto impurities. A more satisfactory result is obtained if the estimate of  $\delta E_n$  is increased by 30% (line 2). The curve indicates also the qualitative effect of the likely variation of  $\mu_2$  with valence. The implied  $\delta E_{sc}$  for Zn, Ga and Al impurities are now positive and the negative values for Ge and In are probably not

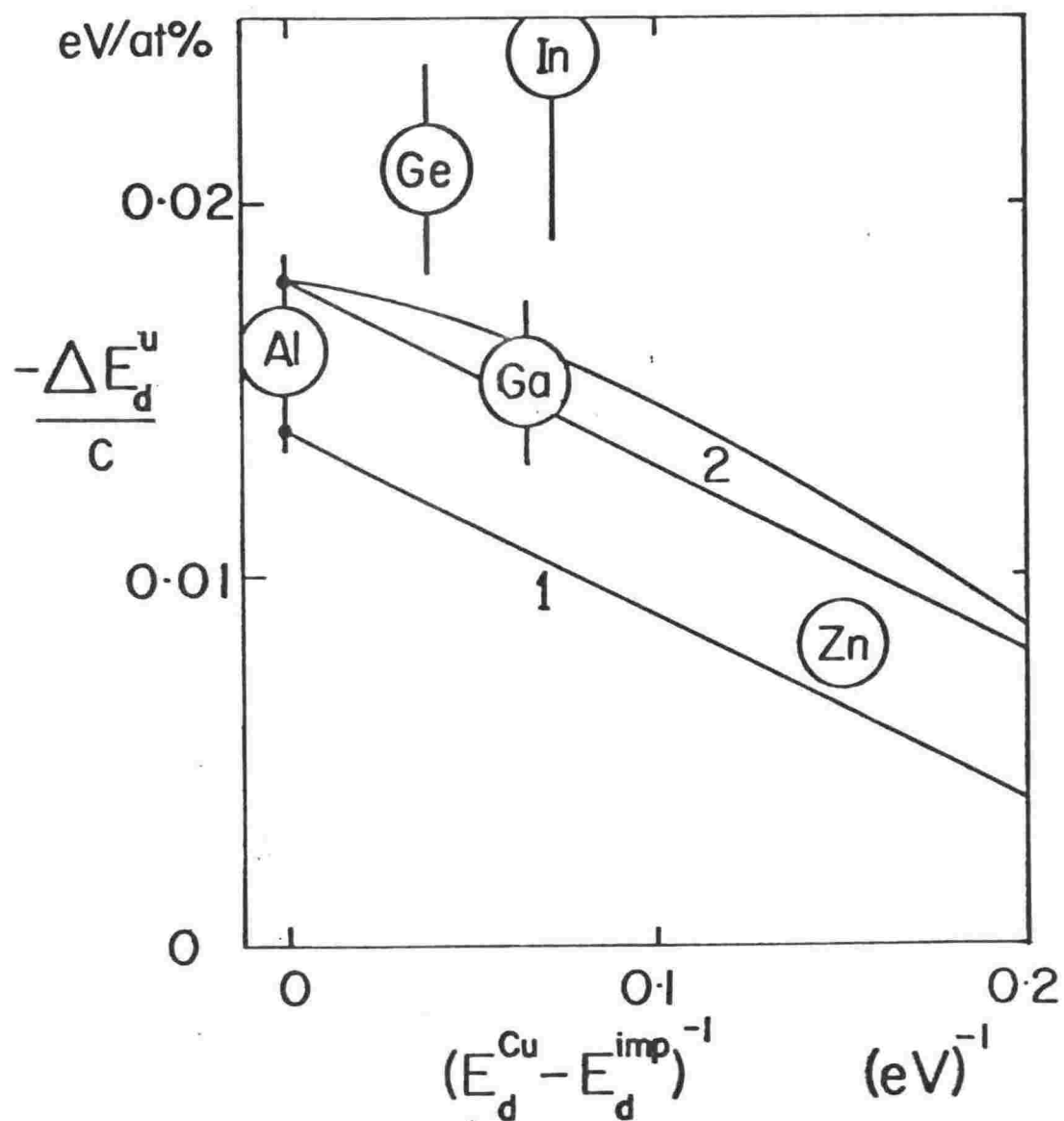


Fig. 5.1 Shift rates of the d band threshold at low concentration plotted against the inverse of the separation in energy of the host and impurity d bands. The solid lines 1 and 2 are explained in the text. The experimental shift rates have been corrected for lattice expansion.



significant in view of the large correction required for lattice expansion in In and the oversimplification of the theory. Because of the uncertainty in  $\delta E_n + \delta E_{dd}$  it is unwise to infer the relative magnitude of charge transfer for different impurities from our results.

To summarise: the most significant feature of the experimental results is that the shift rate  $\Delta E_d^u/c$  for Zn is much smaller than for the other impurities. This has been attributed to a pushing-up of the Cu d bands by the relatively shallow Zn d bands and cannot be explained convincingly by band narrowing and charge transfer alone, as other theoretical work has done, because to produce the required elevation of  $E_d^u$  the charge transfer would need to be larger than that calculated in the renormalised atom approach and, more importantly, the amount of charge transferred would have to decrease significantly as the impurity valence increased - contrary to simple ideas of screening and to the fact that the observed shifts of the Fermi level, discussed next, are larger for Ga and Al impurities than for Zn.

## 5.2 Fermi level

At alloy concentrations greater than about 5 at% the energy of the d band threshold  $E_F - E_d^u$  begins to increase more rapidly; this is attributed to an increase in the Fermi energy. (Otherwise the unlikely event of a sudden increase in the rate of band narrowing or the onset of massive charge transfer from the host onto impurities is required.) In Fig.5.2, the higher concentration d band threshold data are shown. The linear contribution deduced from the low concentration shifts ( $\Delta E_d^u$ ) has been subtracted and the remainder normalised by the excess valence to give  $\Delta E_F/Z$ . The prediction of Friedel for Thomas-Fermi screening of a point charge in an electron gas (Chapter 2.2) is also shown.

The Zn data lie below the prediction up to nearly 20 at% and then rapidly rise above it. This is probably due to shortcomings of the Thomas-Fermi screening - the quantum mechanical treatment of Langer and Vosko (Fig.2.3) predicts a screening charge distribution exceeding the Thomas-Fermi

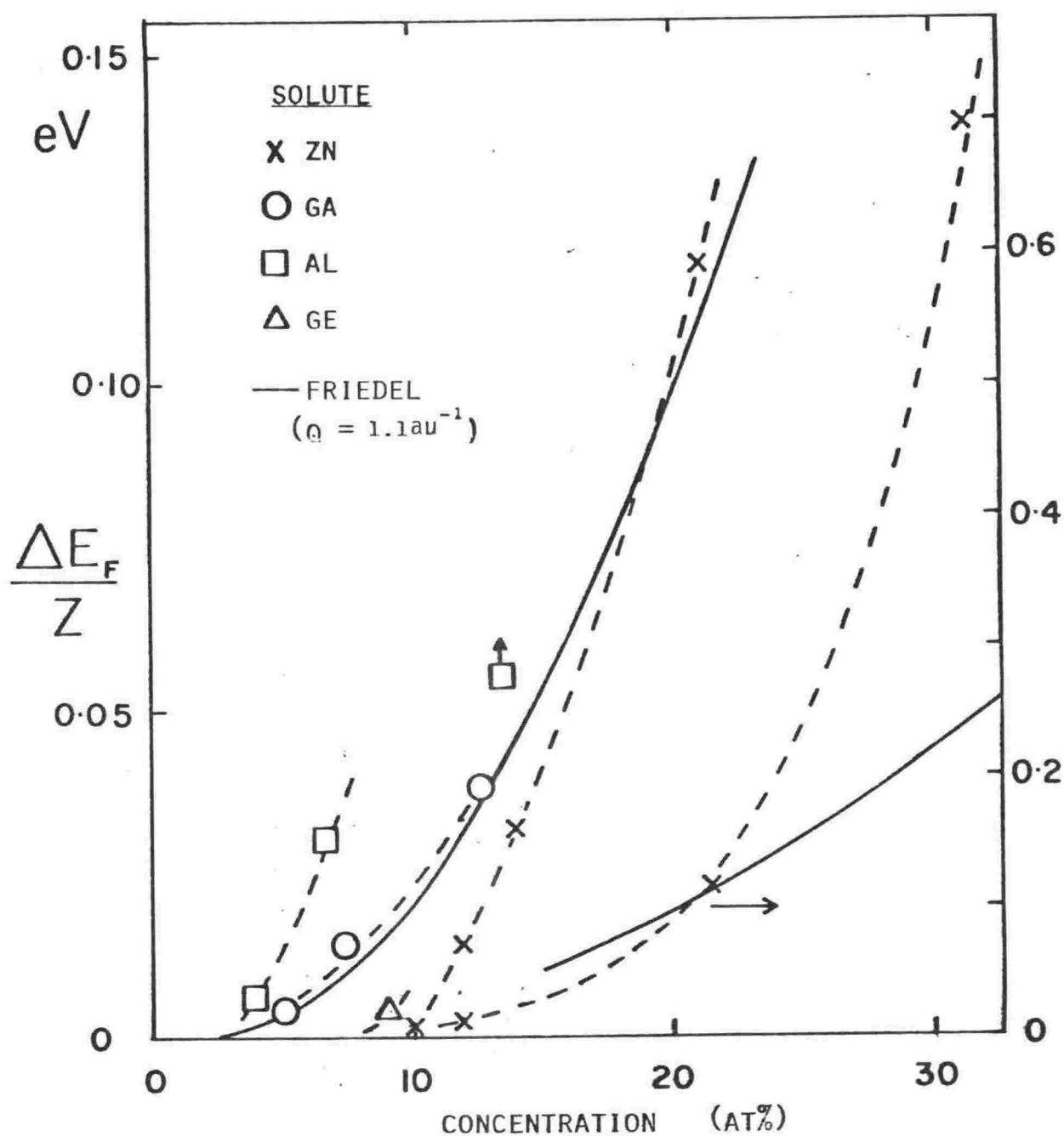


Fig. 5.2 Variation in the Fermi energy; the d band threshold energies in alloys at higher concentration with linear contribution to the shift subtracted. Dashed lines join the experimental points. The solid line is the theory of Friedel (1954) - see page 13.

prediction by up to 100% between 1.1 and 3.5 au and oscillating about it at larger distances. Since the rise in the Fermi level is due to the overlap of screening charge distributions about impurity atoms one might guess that  $\Delta E_F$  is less than the Thomas-Fermi at low concentrations because at low impurity densities the oscillating tails of the charge distributions cancel to give little net charge overlap. At higher concentrations very few Cu atoms are without at least one impurity amongst their nearest neighbours and so the larger Langer and Vosko screening charge density at close range produces a more rapid increase in  $E_F$ . These data would provide an interesting test for self-consistent calculations of the local charge distribution around impurities.

The Ga and Al data exceed the Friedel Thomas-Fermi prediction and demonstrate that factors other than valence are clearly important - both have  $Z = 2$ . The less rapid rise of  $E_F$  for Ga implies a more localised screening distribution and this correlates with the greater electronegativity of Ga on most scales (see the compilation by Chelikowsky and Phillips (1978)) and its more compact Herman-Skillman 4s wavefunction. Ge ( $Z = 3$ ) impurities produce smaller  $\Delta E_F/Z$ . One notes a correlation with the Bloch-Simons ionic radius parameter  $r_s$  derived from atomic data (see reference above) -  $\Delta E_F/Z$  increases in the order Zn, Ge, Ga, Al; the corresponding values for  $r_s$  are 0.64, 0.64, 0.66, 0.74 (Cu = 0.43).

### 5.3 Conduction bands

#### 1) Interpolation band scheme

To discuss the variation with alloy concentration to the critical energies for interconduction band transitions we will make use of the interpolation band scheme referred to in Chapter 2. Within this scheme the energies of states at symmetry points can be expressed as a sum of parameters related to aspects of tight-binding d bands, NFE conduction bands, and s-d interactions.

In the formulation of Smith and Mathiess (1974) (but with slightly altered notation) the energies

of the conduction band states at L are given by:

$$L_1^U = V_0 + aK^2 + V_{111} + \Delta_{ot} + \Delta_h$$

$$L_2' = V_0 + aK^2 - V_{111}$$

The first pair of terms describes free-electron dispersion, the following terms comprise the pseudopotential Fourier component  $V_{111}$  (producing an NFE band gap) and further contributions to the  $L_1^U - L_2'$  bandgap from orthogonalisation and hybridisation interactions with d states. Note that the p-like  $L_2'$  state is unhybridised and is simply depressed from the free-electron energy by  $V_{111}$ .

According to a recent parametrisation (Smith, 1979) of the band structure calculation by Janak et al (1975) the appropriate parameters for Cu are  $aK^2 = 9.25$  eV,  $2V_{111} = 2.65$  eV,  $\Delta_{ot} = 1.15$  eV,  $\Delta_h = 1.45$  eV. Our approach will be to estimate the likely changes in these parameters caused by alloying in order to derive changes in the energies  $L_1^U$  and  $L_2'$  as an aid to interpreting the experimental results. These estimates can only be a guideline since the values of the original parameters were after all chosen to best reproduce a given first principles band structure rather than to give an accurate measure of well-defined terms in the exact Hamiltonian.

In the following subsection estimates are made of the expected variation of the individual parameters on alloying and of the effect on the threshold energy of changes in the radius of Fermi surface neck and the curvatures of the conduction bands. These estimates are summarised in subsection 3) and compared with the experimental results at low impurity con-

centrations. In 4) the variation of the critical energies at high alloy concentrations is considered.

## 2) Alloy parameters

Free electron terms,  $V_0 + aK^2$ : The conduction bands should sink relative to the Fermi level to accommodate the additional states introduced by a polyvalent impurity. If all states on the Fermi surface sink at the same rate then

$$\delta(V_0 + aK^2)/c = -Z/n_0(E_F) = -0.038 Z \text{ eV at\%}^{-1}$$

in the low concentration limit when  $E_F$  is stationary. This is the usual rigid band model estimate.

Pseudopotential  $V_{111}$ : In the virtual crystal approximation the potential for an AB alloy is taken to be  $V = (1 - c)V_A + cV_B$ . Applying this to the pseudopotential components (Mathewson & Myers, 1973) gives

$$\delta V_{111}/c = V_{111}^{\text{imp}} - V_{111}^{\text{Cu}}$$

If  $V_{111}^{\text{imp}} < V_{111}^{\text{Cu}}$  this narrows the NFE gap, raising the  $L_2'$  bonding state and lowering the  $L_1^u$  anti-bonding state. Impurity pseudopotentials estimated from the compilation by Cohen and Heine (1970) and normalised to the atomic volume of the host

$$(\text{i.e. } V_{111}^{\text{imp}} = V(\underline{L})_{\Omega_{\text{imp}}/\Omega_{\text{Cu}}})$$

are listed below. The compilation does not give a comparable value for Cu but  $V_{111}^{\text{Cu}} \sim 1.3 \text{ eV}$  according to the interpolation band structure.

---

	Zn	Ga	Al	In	Ge	
$V_{111}^{\text{imp}}$	1.0	0.5	1.0	1.0	0.2	eV
$\delta V_{111}/c$	-3	-8	-3	-3	-11	$10^{-3} \text{ eV at\%}^{-1}$

---

Orthogonalisation,  $\Delta_{\text{ot}}$ : This involves a combination of the overlap and energy integrals  $\langle d|\underline{k} \rangle$  and

$\langle d|H|k \rangle$  for the d atomic orbital and sp plane wave basis states. The removal of Cu d states on substitution of impurities, along with the increase in sp charge density on Cu sites surrounding an impurity, suggest that

$$\Delta_{ot}(\text{alloy}) = (1 - c + cQ)\Delta_{ot}(\text{pure})$$

where Q represents the effective charge transfer from the impurity to the host, which is retained in the expression in the interests of completeness even though it is small and not amenable to calculation. Thus

$$\delta\Delta_{ot}/c = -(1 - Q)\Delta_{ot} \sim -0.011 \text{ eV at}\%^{-1}$$

if charge transfer is negligible.

Hybridisation,  $\Delta_h$ : The variation of  $\Delta_h$  on alloying is complicated by its dependence on the separation of the  $L_1^U$  and unhybridised  $L_1^L(E_d)$  levels:  $\Delta_h = \frac{\gamma^{2*}}{L_1^U - E_d}$  (Heine, 1967). The hybridisation matrix element  $\gamma$  involves the same overlap integrals as  $\Delta_{ot}$  so the same dilution is expected while the diminishing separation of  $L_1^U$  and  $E_d$  brought about by alloying acts in opposition to increase the hybridisation. Thus in the dilute limit

$$\begin{aligned} \frac{\delta\Delta_h}{\Delta_h} &= 2\frac{\delta\gamma}{\gamma} - \frac{\delta(L_1^U - E_d)}{L_1^U - E_d} \\ &= -2(1 - Q)c - (L_1^U - E_d)^{-1}\delta(V_0 + aK^2 + V_{111} + \Delta_{ot} + 8A_3) \end{aligned}$$

( $8A_3$  is the energy  $\Gamma_{25'} - E_d$  in the interpolation scheme - about 0.6 eV. Its inclusion here accounts for d band narrowing.) Simplifying the earlier estimates by assuming that  $V_{111}$ ,  $\Delta_{ot}$  and  $8A_3$  decrease linearly to zero at  $c = 1$ , we obtain

$$\delta\Delta_h/c = -0.024 + 0.006Z + 0.029Q \text{ eV at}\%^{-1} .$$

One might suppose that this treatment exaggerates the rate at which the orthogonalisation and hybridisation components of the gap are reduced since, with the possible exception of Al, some residual s-d interaction with the impurity d states is to be expected, more so for the low Z impurities with more extended d wavefunctions.

Neck radius and band curvature: Lastly, one must consider the effect on the interconduction band threshold energy of changes in the Fermi surface neck radius and in the curvature  $m_u^{-1}$  of the upper conduction band. The threshold energy  $Q_+ - E_F$  exceeds  $L_1 - E_F$  by  $Q_+ - L_1^u = (E_F - L_2') \frac{m_l}{m_u}$  (see Fig.2.11). In pure Cu,  $\frac{m_l}{m_u} \sim 0.12$  from the band structure of Burdick (1963<sup>u</sup>) and  $E_F - L_2' \sim 0.9$  eV (Knapp et al, 1979) so  $Q_+ - L_1^u$  is only about 0.1 eV. The neck radius increases in the alloys at about the rate predicted by the rigid band approximation ( $\sim 30\%$  slower in the case of Zn) according to positron annihilation studies (Berko & Mader, 1975). Thus one estimates  $Q_+ - L_1^u$  increases due to the expansion of the neck at the rate

$$\delta(Q_+ - L_1^u)_n / c = \frac{m_l}{m_u} \delta(V_0 + aK^2) / c \sim 0.005 Z \text{ eV at\%}^{-1}$$

Changes in  $m_u$  are difficult to estimate, but one might expect the three levels at the ends of the  $Q_+$  and  $Q_-$  branches of the conduction bands (see Fig.2.1) to sink in order of increasing rapidity:  $\delta L_2' < \delta W_3 < \delta L_1^u$  on the basis of their interpolation scheme eigenvalues. (Smith & Mathiess, 1974; both  $W_3$  and  $L_1^u$  are repelled from the d bands by hybridisation, both  $W_3$  and  $L_2'$  are the lower states of NFE band gaps at W and L.) An extreme estimate of the change in  $m_u$  can be made by assuming that  $\delta L_2' \sim \delta W_3$  so that changes in band curvature are directly related to narrowing of the  $L_1^u - L_2'$  band gap by  $\delta m_u / m_u \sim \delta(L_1^u - L_2') / (W_3 - L_1^u)$

$$\delta(Q_+ - L_1^U)c = -(Q_+ - L_1^U)\delta m_u/m_u.$$

According to the Cu band structure of Janak et al (1975)  $W_3 - L_1^U \sim 2.5$  eV; even if  $\delta(L_1 - L_2')/c$  is as large as  $-0.1$  eV at%<sup>-1</sup> the effect is only  $\delta(Q_+ - L_1^U)/c \sim 0.004$  eV at%<sup>-1</sup> and can be disregarded in most of the following discussion.

### 3) Comparison with experiment

The essential feature of the estimates of changes in  $L_1^U$  and  $L_2'$  based on interpolation scheme parameters is that the  $L_1^U - L_2'$  band gap narrows at about  $-0.03$  eV at%<sup>-1</sup> almost irrespective of the impurity species while the valence dependent rigid band filling of states contributes the major part of the shift of both  $L_1^U$  and  $L_2'$  relative to the Fermi level.

The experimental data and theoretical estimates for shift rates in the low concentration limit are collected in Figure 5.3. Notable features of the experimental data (vertical bars) are the low shift rates for Zn, the significant difference between the shift rates for the  $Z = 2$  impurities Ga and Al, and the relatively low value for Ge. Comparison with the theoretical estimates (horizontal bars) shows that although the agreement is reasonable for Ga (and In) none of the notable experimental features mentioned above is predicted. The discrepancies point to two effects not considered in the original estimates:

- i) significant differences in the degree of s-d interaction associated with impurities of different species,
- ii) non-rigid sinking of conduction states at the Fermi level, which we now discuss in turn.
- i) The results for the  $L_1^U - L_2'$  band gap in the Zn alloys (light vertical bar) show that there is negligible gap narrowing apart from that due to lattice expansion. This requires  $\Delta_{ot}$  and  $\Delta_h$  to be small, suggesting very little reduction in s-d interaction on Zn sites. Although the Zn d states are



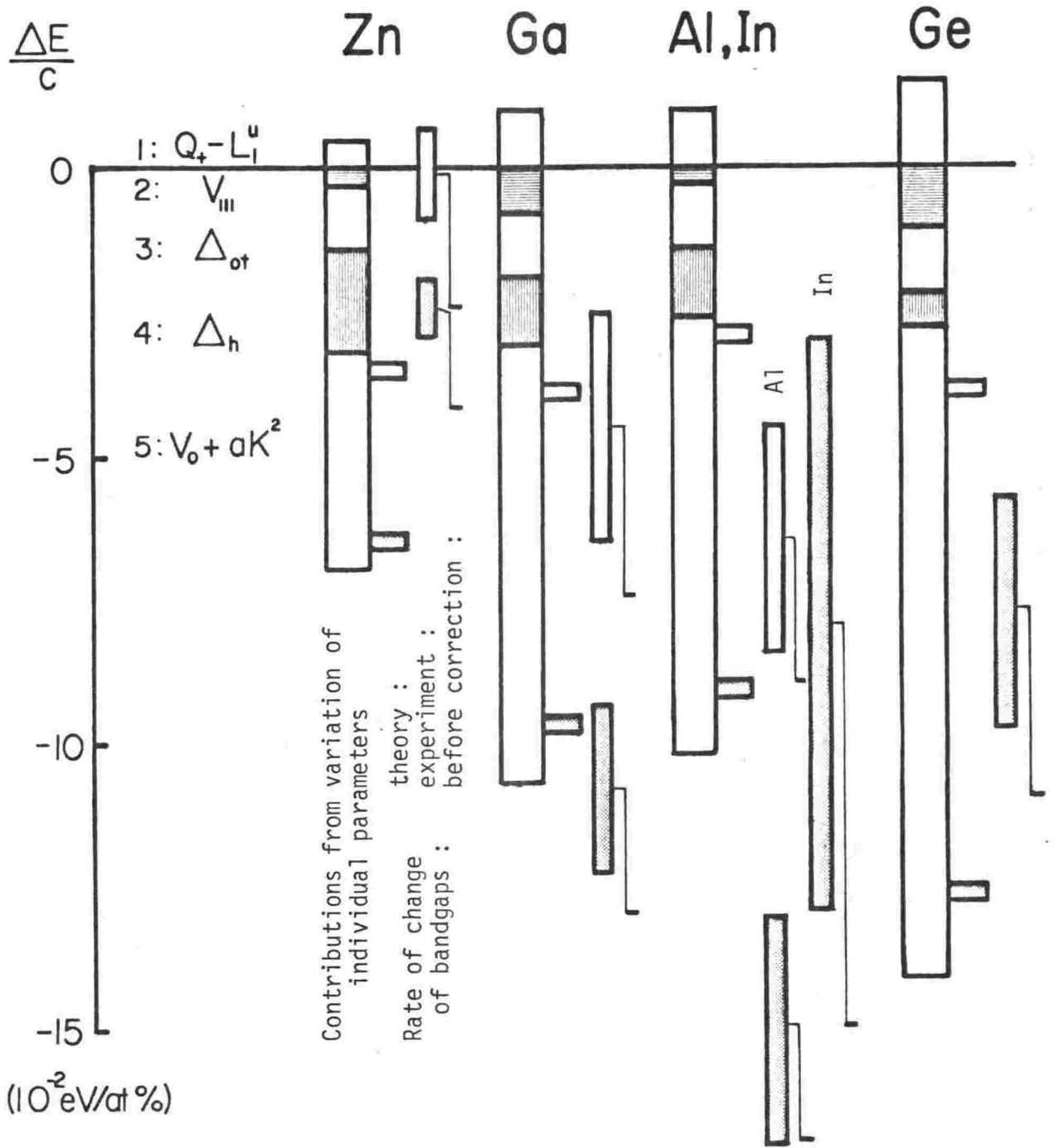


Fig. 5.3 Shift rates of interconduction band critical energies at low concentration compared with theoretical estimates based on band structure interpolation scheme parameters. The theoretical contribution arise from changes in 1) the Fermi surface neck radius, 2) the pseudopotential form factor, 3) s-d orthogonalisation, 4) s-d hybridisation, 5) the free electron energy at the zone boundary.

The dark (light) horizontal bar gives the appropriate sum of the individual contributions to the change in  $Q_+(L_1^u) - E_F (L_1^u - L_2^-)$ . The vertical bars give the corresponding experimental result including correction for the effect of lattice expansion caused by alloying.

degenerate with the bottom of the alloy conduction band according to photomission studies (Norris & Williams, 1978) it is surprising that hybridisation is so little reduced - the high local s electron density of the screening cloud surrounding the impurity must compensate for the more tightly bound d states.

The rapid narrowing of the  $L_1^U - L_2'$  band gap in the Al alloys suggests that in the absence of impurity d states the dilution of s-d interactions is greater than we have estimated.

- ii) The validity of the rigid band approximation\* can be assessed from our results as follows. The rate at which the lower conduction band state  $L_2'$  shifts relative to the Fermi level can be obtained from the difference in the two interconduction band critical energies with allowance made for the widening of the neck as in the preceding subsection:

$$\delta(E_F - L_2') = \delta(L_1^U - L_2') - \delta(Q_+ - E_F) + \delta(Q_+ - L_1^U)$$

The results are given in Table 5.2 expressed as a fraction of the rigid band prediction (-0.038 eV at%). The variation of the  $L_1^U - L_2'$  gap could not be determined for Ge so the two values given assume a rate of narrowing similar to Zn and Ga respectively. The latter estimate, which gives the smallest value of  $\delta(E_F - L_2')$ , seems most reasonable in the light of the discussion in i) above.

---

\*"Rigid band approximation" is used in a restricted sense here to refer to the hypothesis that the energies of conduction band states in the vicinity of the Fermi energy change by the same amount throughout the Brillouin zone to accommodate Z additional states per impurity. The more general rigid band model in which the entire band structure shifts rigidly is plainly in error regarding the d bands and the  $L_1^U - L_2'$  interconduction band gap.

The results for variation in the neck dimensions for these alloys obtained from Fermi surface studies are given for comparison.

Table 5.2 Changes in  $E_F - L_2'$  and the Fermi surface neck as a fraction of the rigid band prediction

	<u>Zn</u>	<u>Ga</u>	<u>Al</u>	<u>Ge</u>
Present work: $\delta(E_F - L_2')$	$0.79 \pm 0.10$	$0.96 \pm 0.15$	$1.28 \pm 0.25$	$0.40 - 0.95^\dagger$
de Haas van Alphen <sup>1</sup> neck area	1.0*	1.0	0.9	0.6
Positron annihilation <sup>2</sup> neck radius	0.7	1.0	1.0	1.0

<sup>1</sup>Coleridge and Templeton, 1971; Templeton and Coleridge, 1975

<sup>2</sup>Berko and Mader, 1975 (review article)

\*Possible overestimated by 30% due to incorrect residual resistivity data

<sup>†</sup>Different values of  $\delta(L_1^U - L_2')$  assumed - see text

Despite some contradictions in the Fermi surface data it seems that changes near L occur more slowly than the rigid band model predicts for Zn and Ge.

Failure of the rigid band model in this sense may have two causes. Firstly, the requirement that added electrons fill states within the Fermi surface is of limited validity because of the incoherence of the alloy wavefunctions (Stern, 1968).

One expects the Fermi surface to expand at most at a rate only 0.99, 0.92, 0.83 (for  $Z = 1, 2, 3$ ) of that assumed by the rigid band model due to the "volume defect" referred to in Chapter 2.2. Secondly, the conduction band may distort; states at different parts of the Fermi surface may sink at different rates. Part of this effect is directly described in terms of variation

of the pseudopotential form factors but there is an indirect effect: for example, even if  $V_{111}$  is unaffected by alloying any swelling of the Fermi surface belly to accommodate more than its share of added states will reduce the rate of sinking of  $L_2'$ . The atomic counterpart of this argument would suggest that the  $4s^2$  closed subshell configuration of a Zn impurity is most attractive to s-like conduction band states in the host and thus produces a greater lowering of the energy of the s-like states around the belly than of the p-like states around the neck. The  $s^2p$  configuration of the  $Z = 2$  impurities would differentiate less between s- and p-like states, producing less distortion of the conduction band.

However, to clearly distinguish volume defect and band distortion effects requires data at a number of locations on the Fermi surface. Phase shift fittings of the various de Haas van Alphen orbits as has been done for Cu(Al) by Templeton and Coleridge (1975) seems to be the most fruitful approach here.

The data of Table 5.2 is also relevant to the question of the existence of bound s states on impurity sites. The fact that Ga, for instance, causes expansion of the Fermi surface corresponding to an excess valence of two seems to discount the theoretical prediction by Zeller and Dederichs (1979) of a bound  $4s$  state on this impurity. The data for Ge impurities might be evidence for such a bound state but the positron annihilation results (McLarnon & Williams, 1977), photoemission studies (Norris & Williams, 1978) and the Hume-Rothery  $\alpha$  phase boundary rule itself (Chapter 1) do not support this view.

#### 4) Results at high concentrations

The changes in the interconduction band shift rates at high concentration are indicative of increasing s-d interaction as explained below. The  $Q_+ - E_F$  and  $L_1^U - L_2'$  critical energies begin to fall less rapidly as alloy concentration increases (see Fig.4.17) in the Al and (to a lesser extent) Ga alloys. The Zn curve has a slight but definite kink. A shift in the Fermi level cannot be responsible; it would produce a faster shift rate, would not affect  $L_1^U - L_2'$ , and in any case the rigid band approximation implies that the conduction bands will move in sympathy with any change in the Fermi level apart from those shifts necessary to accommodate the added impurity states. The decrease in the density of states above the Fermi level (Janak et al, 1975) would also increase rather than decrease the shift rates. Neither can the observed slowing shift rates be due to changes in band curvature or neck radius - these would not affect  $L_1^U - L_2'$ . It therefore seems likely that the slowing shift rate is caused by increased s-d hybridisation brought about by the higher conduction electron density when screening becomes ineffective at high concentrations (Beaglehole & Wihl, 1973). This effect, and the rise in the Fermi level (Chapter 5.2) both result from the overlap of screening clouds and become evident at similar concentrations of impurity. The relative size of the non-linearity in Al, Ga and Zn correlates with the degree of delocalisation of screening charge deduced from the d band threshold data. The required charge transfer is quite large - if 4 eV of the  $L_1^U - L_2'$  gap is assumed to be due to s-d interaction an increase by 0.4 eV (as seems to be the case by ~ 12 at% Cu(Al)) implies a 10% average increase in s charge density which

corresponds to a loss of 0.7 e from each Al site. The nett charge transfer could be reduced if some p charge was transferred in exchange from the host to the impurity.

#### 5.4 Comparison with alloy band structure calculations

The results of average T-matrix calculations for a 30 at% Cu(Zn) alloy by Soven (1966) and Bansil et al (1974) are compared with the experimental results in Table 5.3.

Table 5.3 Changes in critical energies relative to pure Cu for a 30 at% Cu(Zn) alloy (energies in eV)

	<u>Soven</u>	<u>Bansil et al</u>			<u>Experiment*</u>
		CR	SMT	NA	
$\delta(E_F - L_3^U)$	0.80	0.28	0.16	0.96	$0.82 \pm 0.06$
$\delta(L_1^U - E_F)$	-1.22	-1.41	-1.15	-1.43	$-1.15 \pm 0.1$
$\delta(L_1^U - L_2')$	-0.17	-0.22	+0.41	-0.51	$-0.24 \pm 0.1$

\*Corrected for lattice expansion (omitted in the calculations)

and for the effect of expansion of the Fermi surface neck.

The corrections contribute up to 50% of the quoted uncertainty.

The abbreviations CR and SMT refer to the use of empirical charge renormalisation and shifting of the muffin-tin zero in constructing the alloy potential to produce an artificially low d band threshold shift by simulating charge transfer. It seems that neither is a good model of charge transfer, in fact the neutral atom (NA) treatment and Soven's calculation reproduce the d band threshold shift better. This does not imply that charge transfer is negligible, merely that the upper d band states are insensitive to realistic distributions of transferred charge as argued earlier.

The calculated changes in the interconduction band critical energies are in qualitative agreement with experiment except for the SMT prediction of an increasing  $L_1^U - L_2'$  gap and the general overestimate of the rate at which  $L_1^U$  descends.

One important failing of the calculations is that non-

linear changes with concentration of the d band threshold or other critical energies are not predicted, possibly because no attempt has been made to introduce self-consistent localised charge transfer. For this reason the comparison with experiment at a single alloy concentration is unduly flattering.

The above comparison invites several observations. Although the agreement is good in places it reveals little about the underlying interactions. Alloy band structure calculations using the same method for different polyvalent impurities would help a great deal in this area, providing a quantitative basis for the ideas of chemical bonding, valence, charge exchange, electronegativity and the like which it is natural to use to explain alloying trends. The importance of effects due to charge overlap and local lattice distortion - both outside the scope of periodic muffin-tin potentials - might be profitably explored by model calculations.

Finally, efforts should be made to make comparison between experiment and theory as direct as possible. The Fermi energy should be determined explicitly (as Bansil et al have done) and if  $\epsilon_2$  itself cannot be computed, optical threshold energies should be determined since they do not usually occur at symmetry points. For example, the interpretation of the present results would have been more straightforward if alloy band structure calculations had provided the curvature of the bands near L.

### 5.5 Hume-Rothery $\alpha$ phase boundary rule

A strong motivation for the present work was to see whether one might be able to throw light on the origin of the Hume-Rothery  $\alpha$  phase boundary rule by monitoring features of the alloy band structure at high concentration. As related in Chapter 1 the boundary for the fcc-bcc transformation occurs in the alloys (except Cu(In)) at an e/a ratio of about 1.4. Hume-Rothery and Roaf (1961) suggested that the phase boundary occurs when the Fermi surface contacts the Brillouin zone boundary at X, in other words as the  $X_4'$  level sinks

below the Fermi energy. A clear indication of this event would be given by the disappearance of the  $X_5 \rightarrow X_4'$  signature in the piezoreflectance tetragonal shear response as it merged with the structure marking the d band threshold. Unfortunately the  $X_5 \rightarrow X_4'$  feature was not visible in the piezoreflectance results for alloy films and the behaviour of  $X_4'$  can only be inferred indirectly from experimental results concerning the conduction band states at L.

To begin with we can estimate the rate at which  $X_4'$  must sink relative to the Fermi level in order to reach it by  $e/a = 1.4$ . Despite assertions to the contrary (Heine & Weaire, 1970) an implausibly high shift rate is not required. Allowing for the variation of the density of states above the Fermi level ( $n(E) \sim 0.26 \text{ eV}^{-1}$  at  $E_F$  decreasing to  $0.22 \text{ eV}^{-1}$  at  $X_4'$  according to the Cu band structure of Janak et al (1975)) then a rigid band shift will lower  $X_4'$  from 2.0 eV above  $E_F$  in pure Cu to only 0.35 eV above when  $e/a = 1.4$ . This means an average shift rate only 20% greater than the rigid band estimate is sufficient to produce contact with the (200) zone face at the phase boundary.

If the conduction band does not sink rigidly and the slow shifts near  $L_2'$  seen in the Cu(Zn) results are compensated by more rapid sinking near  $X_4'$  it is arguable that zone touching can take place. However, Cu(Al) de Haas van Alphen results (Templeton & Coleridge, 1975) indicate that, in extremely dilute alloys, the states in the X direction sink more slowly than those elsewhere on the Fermi surface - at only 76% of the rigid band rate. This seems to rule out zone-touching at the phase boundary in this alloy.

We do observe one common feature of the band structure of the Zn, Ga and Al alloys which may be related to the phase boundary; the  $Q_+ - E_F$  critical energy for these alloys tends to level off to a common value of about 2.5 eV as  $e/a$  approaches 1.4 despite their quite different shift rates in the dilute range (see Fig.4.17). The reasons for this regularity are not clear. In fact



if it were not for this single instance of a common band structure feature in the concentrated alloys one would be inclined to view the phase boundary rule as being a consequence of increasing conduction electron density unrelated to electronic structure. This favours the explanation advanced by Stroud and Ashcroft (1971) and others which connects the phenomenon with the anomaly in the wavevector dependent dielectric constant  $\epsilon(q)$  at  $q = 2k_F$ . When the electron density increases to a point where  $2k_F$  is commensurate with a reciprocal lattice vector their calculations show a change in the relative stability of the different crystal structures.

#### 5.6 Summary of experimental findings and conclusions

Due to the high resolution of piezoreflectance measurements, the results of the present study, although in qualitative agreement with previous optical work, reveal some new features of alloying behaviour and provide accurate critical energy data for comparison with theory.

The d band threshold data showed the effects of:

- 1) d band narrowing due to dilution of the host
- 2) repulsion between host and impurity d bands.

The results were not consistent with elevation of the d bands due to charge transfer.

The Fermi level was seen to rise relative to the centre of gravity of the d bands as screening became ineffective and the results suggested that in concentrated alloys the d band threshold occurs at energies above the interconduction band threshold - as clearly seen in the most concentrated Cu(Zn) alloy.

The interconduction band results showed:

- 1) s-d interaction is undiluted at Zn impurity sites, in contrast to Ga and Al. Higher conduction electron density in the more concentrated alloys tends to oppose dilution of the interaction.
- 2) For alloys with Zn and Ge, states in the lower conduction band near the neck appear to sink relative to the Fermi level more slowly than the rigid band prediction, in support of de Haas van Alphen results.

One feature common to all alloys\* near the phase boundary was an interconduction band threshold energy  $Q_+(L_1^U) - L_2'$  of  $\sim 2.5$  eV. Information about the crucial transition for zone-touching,  $X_5 \rightarrow X_4'$ , was not accessible - piezoreflectance measurements on single-crystal specimens of alloys close to the phase boundary should be made to remedy this failing.

The d band and interconduction band data plainly showed differences between the isovalent impurities Ga and Al with the implication that simple arguments based on the electron to atom ratio must be augmented by more sophisticated theoretical efforts.

---

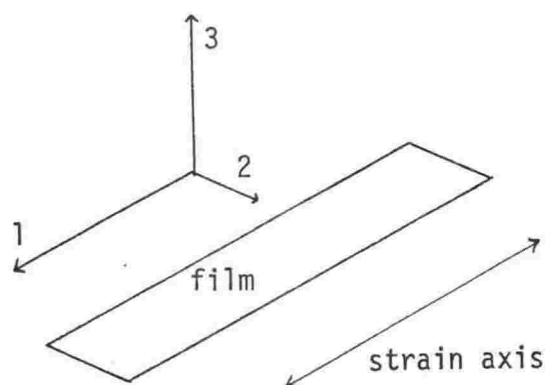
\*The relevant information was unobtainable for Ge and In alloys.

## APPENDICES

1 Strain-optic response of textured films

We calculate the combination of the single crystal (fcc) piezo-optic constants (see Chapter 2.4) which would be measured in the present experimental confirmation for a film of pure (hkl) texture - in which all crystals have a given (hkl) vector normal to the substrate plane but are orientated randomly around it.

The co-ordinate system is as shown.



The strain in the substrate is defined by  $e_{22} = -\nu e_{11}$  where  $\nu$  is Poisson's ratio for the substrate material fused quartz ( $\nu = 0.17$ ). Shear strains are negligible.

The crystals of the film are assumed to follow the substrate strain in the plane of the film:

$$e_{11}^i = e_{11}, e_{22}^i = \nu e_{11}$$

but the strain perpendicular to the film is determined in the individual crystals by the condition  $\sigma_{33} = 0$ . Thus  $e_{33}^i = -k e_{11}$  where  $k$  depends on the orientation of the crystal with respect to the substrate normal and (in general) the strain axis. These assumptions seem to be justified by the study by Vook and Witt (1965) of evaporated films subjected to strain by thermal expansion of the substrate. They found that the  $e_{33}^i$  for a given (hkl) orientation calculated on the basis of the assumptions above agreed with the strain measured by X-ray diffractometry.

The procedure is straightforward, but sufficiently tedious, considering that the results have no direct application, that only the (001) and (111) textures were treated. The single crystal tensors were transformed to the desired (hkl) orientation and the responses for light polarised  $\parallel$  and  $\perp$  to the strain axis averaged over rotations of the crystals about (hkl). The results, expressed in terms of the symmetry combinations of  $Q_{ij}$ , are summarised in the table on page 77.

## 2 Alloy concentrations from resistance and X-ray fluorescence measurements

The thickness of the films is deduced from fluorescence measurements:  $t \propto X/n$  where  $X$  is the total copper fluorescent counts measured under standard conditions,  $n$  is the density of copper atoms in the sample. The correction to  $X$  for attenuation of the exciting and fluorescent radiation in the sample was less than 1% because the films were thin.

The copper density in the alloy is related to that in the pure material by

$$n = n_0(1 - c)/(1 + \frac{1}{V} \frac{dV}{dc} c) = An_0$$

where the bracketed factors account for dilution of the solvent and expansion of the lattice.

The resistance of a section of film of length  $l$ , width  $w$ , and thickness  $t$  is given by  $R = \frac{\rho l}{wt}$ . The fractional difference in resistivity of an alloy and pure sample is then

$$\frac{\rho - \rho_0}{\rho_0} = \frac{tR}{t_0 R_0} - 1 = A^{-1}xr - 1 \quad (1)$$

where  $x$  and  $r$  are fluorescence counts and resistance both normalised to the values for the pure sample.

The literature supplies the relationship

$$\frac{\rho - \rho_0}{\rho_0} = (\delta\rho c + \delta'\rho c^2)/\rho_0 \quad (2)$$

and residual resistivity data.

Equating (1) and (2) gives

$$\delta' \rho c^3 + c^2(\delta \rho - \delta' \rho) - c(\delta \rho - \rho_0(1 + \frac{1}{v} \frac{dV}{dc} x r)) + \rho_0(x r - 1) = 0$$

which is readily solved for  $c$  using a programmable calculator.

### 3 Notes on experimental systems

#### Strain transducer

The longitudinal strain in the substrate is given by (Robinson & Edgar, 1974)

$$e_{11} = 1.12 \times 10^{-5} C_m v_g \sin(2\pi X/\lambda) \sin(\omega t)$$

for transducers of the type and dimensions used with capacitive loading of the gauge crystal.  $C_m$  and  $v_g$  are the capacitance and rms voltage across the gauge crystal.  $C_m$  is determined by measuring the reduction in gauge voltage  $\delta v$  on connecting a test capacitance in parallel with the gauge crystal:

$$C_m = C_t(v_g - \delta v)/\delta v.$$

The components were cemented with Loctite I.S.12 or equivalent adhesive. Wiping the surfaces to be joined with dilute NaOH solution made the joint easier to snap when demounting samples.

#### Optical systems

Calibration of monochromators: the following lines from spectral lamps are sufficient: Hg 546.1 nm, Cd 643.8 nm, Cd 326.1 nm.

Filters to eliminate second order monochromator output and reduce stray light: (all long wavelength pass filters)

<u>Spectral range</u>	<u>Filter</u>
350 - 620 nm	CS 0-52
620 - 720 nm	CS 2-62
720 - 800 nm	RG-9

Calibration of differential reflectometer: with a sample in one aperture and the T beam (Fig.4.5) blocked by an absorber the phase of the lock-in was set and the system calibrated for unity by adjusting the photomultiplier gain control to give full scale deflection on the X-Y recorder. Sensitivity was altered using the lock-in gain control which had been trimmed to give less than 1 part in  $10^3$  error between ranges.

#### Choice of time constants

Experimental systems like the piezoreflectance and differential reflectance systems have associated with them four characteristic frequencies:  $\omega_m$  - the modulation frequency, at which the lock-in amplifier operates;  $\omega_c$  - the inverse of the time constant of the d.c. channel (the photomultiplier automatic gain control);  $\omega_d$  - the inverse of the time constant of the lock-in amplifier;  $\omega_s$  - the scanning frequency of the system,  $\frac{1}{\Delta\lambda} \frac{d\lambda}{dt}$ , in optical bandwidths per second.

To avoid systematic errors one must ensure  $\omega_m > \omega_c > \omega_d > \omega_s$ .  $\omega_m > \omega_c$  ensures there is no attenuation of the signal by the action of the gain control,  $\omega_c > \omega_d$  and  $\omega_d > \omega_s$  ensure there is no variation in the output due to fluctuations in light intensity,  $\omega_d > \omega_s$  ensures there is no displacement or distortion of the experimental spectrum from scanning too fast. The final constraint is usually most important since the overriding objective is to minimise the scan time without degrading the quality of the data (i.e. to maximise  $\omega_s$  and minimise  $\omega_d$ ). The time constants selected for the two systems were as follows ( $\omega = 1/\tau$ ):

	$\tau_m$	$\tau_c$	$\tau_d$	$\tau_s$
Piezoreflectance	$2 \cdot 10^{-6}$	$3 \cdot 10^{-3}$	3	22
				(seconds)
Differential reflectance	$7 \cdot 10^{-3}$	0.03	0.3	2.5

For the differential reflectance system to scan this rapidly a notch filter at  $2\omega_m$  (or a ladder filter at the output to increase the high frequency attenuation) was required to

attenuate the large component of the signal at this frequency (see Fig.4.5).

#### 4 Computing

The basic data to be processed are  $\frac{\Delta R}{R}_{||}$  and  $\frac{\Delta R}{R}_{\perp}$  (PR)  $(R_a - R_p)/(R_a + R_p)$  (DR), and  $R_p$ . These are digitised from XY recorder traces at a standard set of energy points. (280 points in the range 0-10 eV at average 2 nm spacing over the range 600-250 nm.) Data are only recorded at energies necessary to define the experimental curve with straight line segments - blank entries are deleted later. Since more than 100 individual files were processed the standard energy file was essential to minimise labour. The four files above were entered on a magnetic disk and checked for errors by plotting on a visual display unit.

A programme (BATCH) then produced a single combined file with the following operations:

- i) Scaled PR by calibration factor (original entries were as rms signal in  $\mu V$ ). Adjusted PR to zero in IR.
- ii) Produced common reduced set of energy values based on the union of the sets for  $||$  and  $\perp$  PR spectra, interpolating where necessary.
- iii) Applied stray light correction to PR data.

$$X = X'(1 + B) = X_s B$$

where  $X(\omega)$  is the true signal  $\frac{\Delta R}{R}$  which would be measured in the absence of stray light,  $X'(\omega)$  is the experimental signal,  $X_s$  is the signal due to stray light only (measured at 235 nm), and  $B(\omega)$  is the ratio of stray light intensity to true light intensity. (Fig.A.1) (Measured for a pure sample assuming that the stray light intensity throughout the region where the correction is important is equal to the value at 235 nm.  $B(\omega)$  is not significantly different for alloy samples because the difference in reflectance averaged over the spectrum is small.) The accuracy of the correction was checked as recounted in Chapter 4.1 for  $||$  polarisation. For

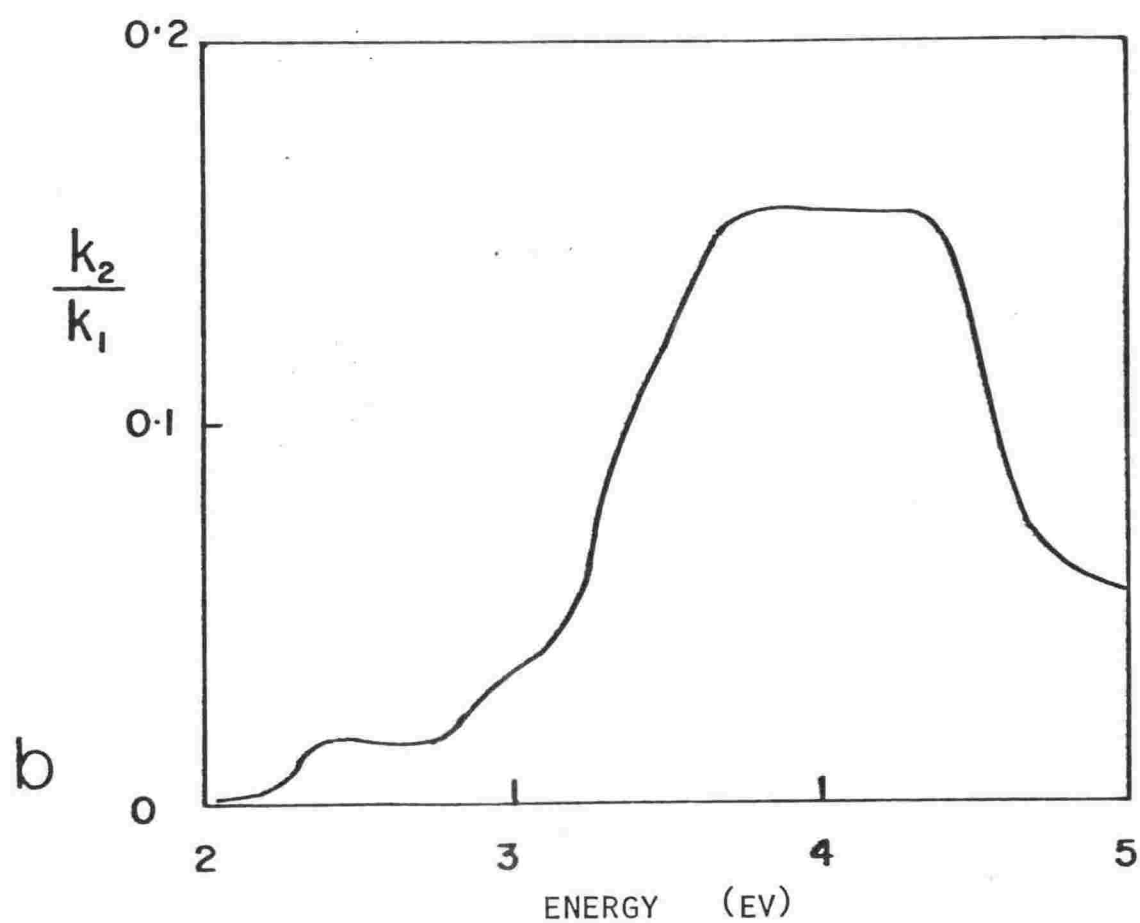
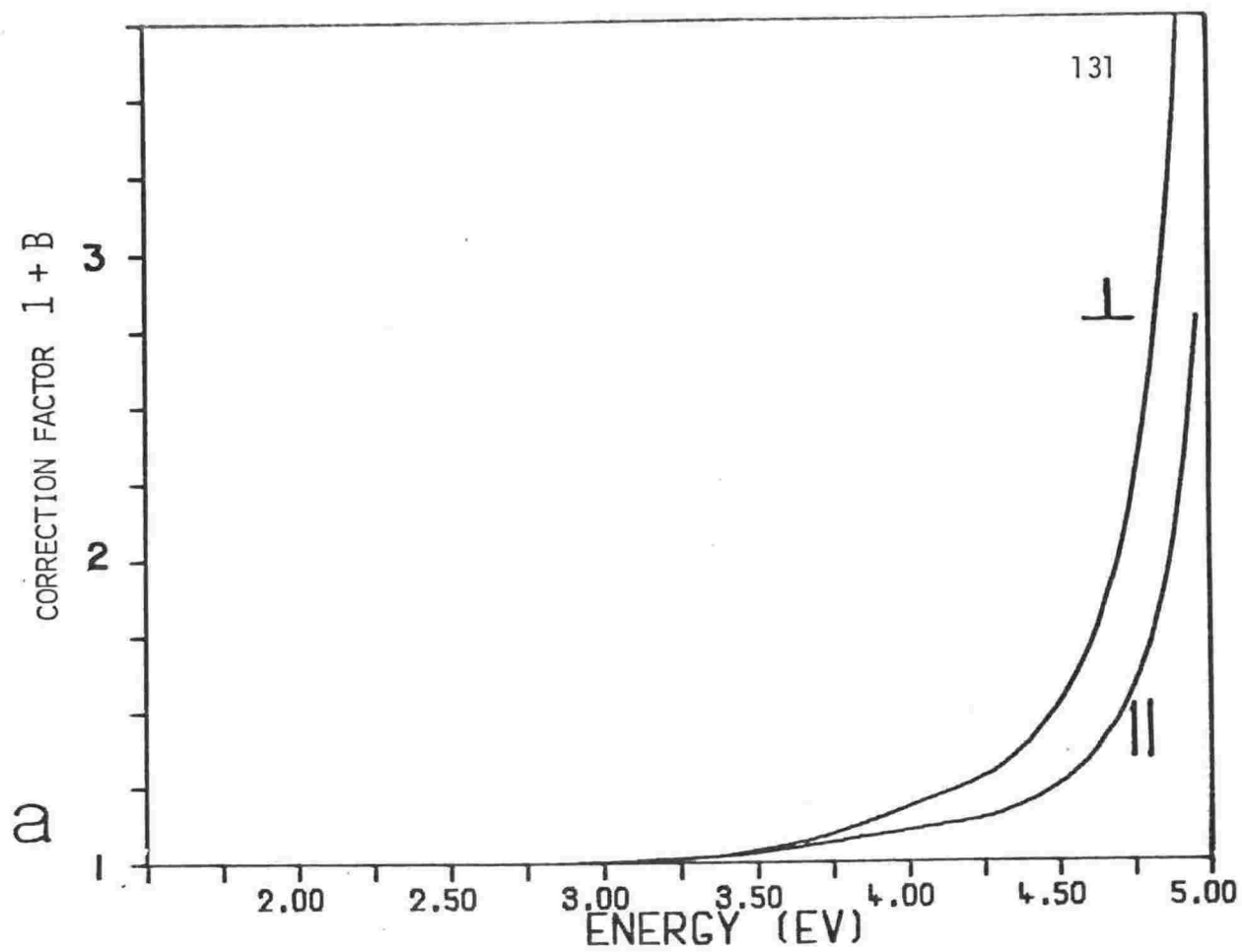


Fig.A.1 Stray light and polariser data.

- a) Piezoreflectance spectra stray light correction factor (see text).
- b) Typical data provided by manufacturer for extinction ratio of Polacoat polariser.



the  $\perp$  polarisation the correction is not reliable above 4.5 eV but this region of the  $\perp$  spectrum contains no useful information in any case.

- iv) Applied optional correction for low polarisation.  
 "Crosstalk" between the  $\parallel$  and  $\perp$  polarisations can be corrected for using

$$X_{\parallel} = (1 + A)X'_{\parallel} - AX_{\perp}$$

and a similar expression with  $\parallel$  transposed for  $\perp$ .  
 $A = k_2 I_{\perp} / k_1 I_{\parallel}$ , where  $\frac{k_2}{k_1}(\omega)$  is the polariser transmittance data displayed in Fig.A.1b;  $I_{\perp}/I_{\parallel}$  is the ratio of intensities of each polarisation. Since the  $k_2/k_1$  data were typical specs supplied by the manufacturer the correction is of questionable reliability. An example is shown in 4.10b, the correction can be disregarded as explained there.

#### Extrapolations

The PR, DR and R data need extrapolations in three spectral regions.

- i) Infrared 0-1.7 eV:

PR : the small constant signal level in the near IR was adjusted to zero as described above.  
 DR, R : the nearly constant level in the near IR was adjusted to 0 and 1 respectively at zero energy consistent with free-electron absorption.

Any reasonable variation on these procedures, e.g. small non-zero PR in the IR had negligible effect on the interband results.

- ii) Ultraviolet (5-10 eV): This is the most difficult region since the determination of the  $L_2' \rightarrow L_1^U$  critical energy is affected in the more dilute alloys.

PR: adjusted smoothly to zero by 10 eV. A standard extrapolation of the form:

$$\frac{\Delta R}{R}(\omega) = \frac{\Delta R}{R}(\omega') [(\omega' - \omega_0)/(\omega - \omega_0)]^n$$

was used with  $\omega_0$  chosen to match slopes at the limit of experimental data  $\omega'$  and the exponent  $n$  usually  $\sim 4$  to maintain a similarly shaped drop-off in the pure and alloy spectra. This choice of the extrapolation for PR was unavoidably somewhat arbitrary but was guided by the shape of the PR high energy tail exposed in the near UV in the most concentrated alloys.

DR: adjoined smoothly to zero at 10 eV

R : data from far UV studies by D. Beaglehole (1965) was used.

- iii) Far ultraviolet ( $10 \text{ eV} \rightarrow \infty$ ): Reflectivity data were extrapolated in the Kramers - Kronig transform from the high energy of the file data at  $\omega_0$  by the standard expression

$$R = R_0(\omega_0/\omega)^X$$

where  $X$  was chosen to reproduce the results of independent optical measurements in the visible.  $X$  was usually between 1 and 1.4.

In fact,  $X$  was chosen for pure Cu samples to produce  $\epsilon_2 \sim 5.5$  at 460 nm (typical of unoxidised films) and for alloys was chosen to reproduce  $\epsilon_2(\text{pure}) - \epsilon_2(\text{alloy})$  measured by the method of Chapter 4.3.

By using the difference in  $\epsilon_2$  to determine the extrapolation the gross effects of the oxide film common to both pure and alloy samples should be subtracted. The details of this procedure are unimportant as is evident from Fig.A.2 which shows the typical effects on the  $(\hbar\omega)^2\Delta\epsilon_2$  spectra of variations in the input data and extrapolations.

The basic programme used to perform the numerical Kramers-Kronig integral (see Chapter 2.3) is listed by Bassett (1974). The general input is a file of  $R(\omega)$  data points and the parameter defining the high energy extrapolation; the output is  $\epsilon_1(\omega)$  and  $\epsilon_2(\omega)$  or other desired functions of the optical constants. In the present application files of alloy reflectance and strained alloy reflectance ( $\parallel$  and  $\perp$ ) are derived from the input data in the obvious manner,

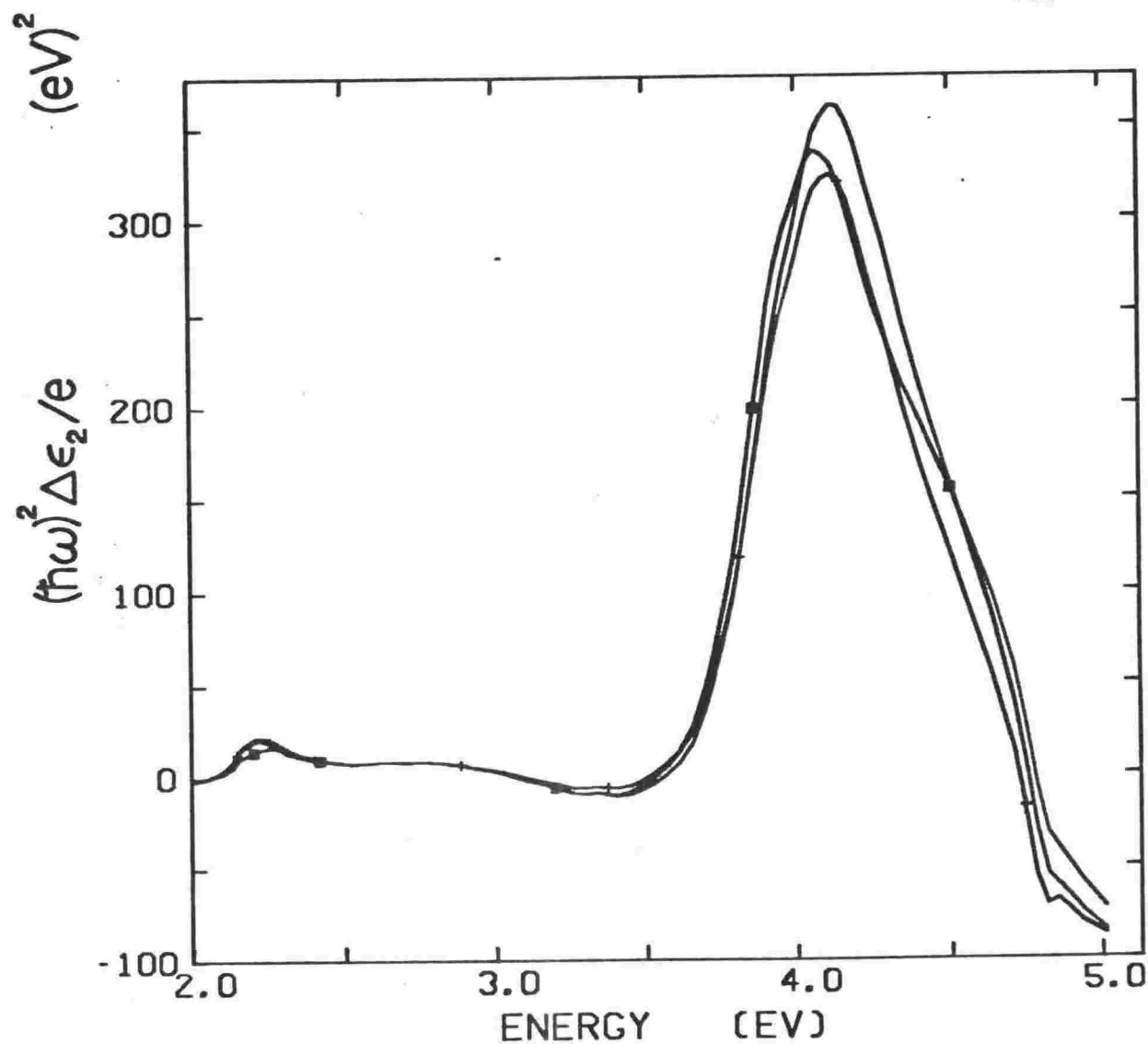


Fig.A2 Computational effects in  $(\hbar\omega)^2\Delta\epsilon_2/e$  || results. The three spectra shown are the result of Kramers-Kronig integration of the  $\Delta R/R$  data for a 5.65 at% Cu(Zn) alloy using i) the normal procedure ii) a far UV extrapolation parameter some 30% too large iii) the reflectance data for pure Cu rather than the alloy itself. Effects ii) and iii) are much larger than anticipated systematic errors but the energy of the peak is only shifted of the order of 0.04 eV.

the three separate Kramers-Kronig transforms performed and quantities such as  $(\hbar\omega)^2\Delta\epsilon_2$  obtained by subtraction. Twelve minutes of PDP-15 computer time are required for a 150 point spectrum.

## REFERENCES

- Ashcroft, N. W. and Mermin, N. D., 1976, "Solid State Physics", Holt, Rinehart and Wilson, New York.
- Bansil, A., Ehrenreich, H., Schwartz, L. and Watson, R. E., 1974, Phys.Rev. B9, 445.
- Bassani, G. F. and Parravicini, G. P., 1975, "Electronic States and Optical Transitions in Solids", Pergamon, Oxford.
- Bassett, M. B., 1974, unpublished M.Sc. thesis, Victoria University of Wellington.
- Batz, B., 1967, Solid State Commun. 5, 985.
- Beaglehole, D., 1965, Proc.Phys.Soc. 85, 1007.
- \_\_\_\_\_, 1968, Appl.Opt. 7, 2218.
- \_\_\_\_\_ and Erlbach, E., 1972, Phys.Rev. B6, 1209.
- \_\_\_\_\_ and Wihl, M., 1973, J.Phys. F3, 1760.
- Beeby, J. L., 1964, Phys.Rev. 135, A130.
- Berko, S. and Mader, J., 1975, Appl.Phys. 5, 287.
- Biondi, M. A. and Rayne, J. A., 1959, Phys.Rev. 115, 1521.
- Blatt, F. J., 1968, "Physics of Electronic Conduction in Solids", McGraw-Hill, New York, p.199.
- Burdick, G. A., 1963, Phys.Rev. 129, 138.
- Cardona, M., 1969, "Solid State Physics", (eds. F. Seitz, D. Turnbull and H. Ehrenreich), Academic Press, N.Y., Supplement 11.
- Carotenuto, C., Rosei, R. and Sommacal, M., 1976, Solid State Commun. 19, 547.
- Chelikowsky, J. R. and Phillips, J. C., 1978, Phys.Rev. B17, 2453.
- Chen, A. B. and Segall, B., 1976, Solid State Commun. 18, 149.
- Chopra, K. L., 1969, "Thin Film Phenomena", McGraw-Hill, N.Y.
- \_\_\_\_\_, Suri, R. and Thakoor, A. P., 1977, Phys.Rev. B15, 4682.
- Cohen, M. L. and Heine, V., 1970, Solid State Physics, 24, 38.

- Colavita, E., Modesti, S. and Rosei, R., 1975, Solid State Commun. 17, 931.
- Coleridge, P. T., 1979, J.Phys. F9, 473.
- \_\_\_\_\_ and Templeton, I. M., 1971, Can.J.Phys. 49, 2449.
- Cooper, B. R., Ehrenreich, H. and Philipp, H. R., 1965, Phys.Rev. 138, A494.
- Crisp, R. S. and Henry, W. G., 1978, J.Phys. F8, 1767.
- Dalton, N. W., 1970, J.Phys. C3, 1912.
- Davis, H. L., Faulkner, J. S. and Joy, H. W., 1968, Phys.Rev. 167, 601.
- De Reggi, A. S. and Rea, R. S., 1973, Phys.Rev.Lett. 30, 549 (also Phys.Rev. B9, 3285 (1974)).
- d'Henrle, F., Alliota, C., Brusic, V., Dempsey, J. and Irmischer, D., 1977, Vacuum 27, 321.
- Ehrenreich, H. and Schwartz, L., 1976, Solid State Physics 31, 150.
- Friedel, J., 1954, Adv.Phys. 3, 446.
- Garfinkel, M., Tiemann, J. J. and Engeler, W. E., 1966, Phys.Rev. 148, 695.
- Gerhardt, U., 1968, Phys.Rev. 172, 651.
- Giaque, R. D., Goulding, F. S., Jaklevic, J. M. and Pehl, R. H., 1973, Anal.Chem. 45, 671.
- Glang, R., 1970, "Handbook of Thin Film Technology" (eds. L. I. Maissel and R. Glang), McGraw-Hill, N.Y.
- Grüner, G. and Minier, M., 1977, Adv.Phys. 26, 231.
- Hansen, M., 1958, "Constitution of binary alloys", McGraw-Hill, N.Y.
- Harbeke, G., 1972, in "Optical Properties of Solids", (ed. F. Abelés), N.Holland, Amsterdam, p.21.
- Heine, V., 1967, Phys.Rev. 153, 673.
- \_\_\_\_\_ and Weaire, D., 1970, Solid State Physics, 24, 250.
- Herman, F., and Skillman, S., 1963, "Atomic Structure Calculations", Prentice-Hall, New York.
- Hodges, C. H., 1978, Phil.Mag. B38, 205.
- Hodges, L., Ehrenreich, H. and Lang, N. D., 1966, Phys.Rev. 152, 505.

- Hodges, L., Watson, R. E. and Ehrenreich, H., 1972, Phys.Rev. B5, 3953.
- Hodgson, J. N., 1970, "Optical Absorption and Dispersion in Solids", Chapman and Hall, London.
- Hume-Rothery, W. and Roaf, D. J., 1961, Phil.Mag. 6, 55.
- Hunderi, O., 1972, Appl.Optics 11, 1572.
- \_\_\_\_\_, 1979, Thin Solid Films 57, 15.
- Janak, J. F., Williams, A. R. and Moruzzi, V. L., 1975, Phys.Rev. B11, 1522.
- Jenkins, R. and de Vries, J. L., 1957, "Practical X-Ray Spectrometry", Philips Technical Library.
- Juras, G. E. and Segall, B., 1973, Surface Sci. 37, 929.
- Knapp, J. A., Himpfel, F. J. and Eastman, D. E., 1979, Phys.Rev. B19, 4952.
- Koster, G. F. and Slater, J. C., 1954, Phys.Rev. 95, 1167.
- Langer, J. S. and Vosko, S. H., 1960, J.Phys.Chem. Solids 12, 196.
- Levin, K. and Ehrenreich, H., 1971, Phys.Rev. B3, 4172.
- Linde, J. O., 1932, Ann.d.Phys. 15, 219.
- Mathewson, A. G. and Myers, H. P., 1973, J.Phys. F3, 623.
- McLarnon, J. G. and Williams, D. L., 1977, J.Phys.Soc.Japan, 43, 1244.
- Morris, C. E. and Lynch, D. W., 1969, Phys.Rev. 182, 719.
- Moruzzi, V. L., Williams, A. R. and Janak, J. F., 1974, Phys. Rev. B10, 4856.
- Mott, N. and Jones, H., 1958, "The Theory of the Properties of Metals and Alloys", Dover, New York.
- Mueller, F. M., 1967, Phys.Rev. 153, 659.
- Nastasi-Andrews, R. J. and Hummel, R. E., 1977, Phys.Rev. B16, 4314.
- Nikitine, S., 1969, in "Optical Properties of Solids", (ed. S. Nudelman and S. S. Mitra), Plenum, N.Y.
- Nilsson, P. O., 1970, Phys.Scripta 1, 189.
- \_\_\_\_\_, and Sandell, B., 1970, Solid State Commun. 8, 721.
- \_\_\_\_\_, 1974, Solid State Physics, 29, 139.
- Norris, C. and Williams, G. P., 1978, Phys.Stat.Sol. (b) 85, 325.

- Nye, J. F., 1957, "Physical Properties of Crystals", Oxford, London.
- Painter, G. S., 1978, Phys.Rev. B17, 3848.
- Pearson, W. B., 1964, "A handbook of lattice spacings and structures of metals and alloys", Pergamon, Oxford.
- Pells, G. P. and Montgomery, H., 1970, J.Phys.C. 3, S330.  
 \_\_\_\_\_ and Shiga, M., 1969, J.Phys.C.2, 1835.
- Rayne, J.A., 1961, Phys.Rev.121, 456.
- Riley, J. D., Leckey, R. C. G., Jenkin, J. G., Liesegang, J. and Poole, R. T., 1976, J.Phys. F 6, 293.
- Roberts, S., 1960, Phys.Rev. 118, 1509.
- Robinson, W. H. and Edgar, A., 1974, IEEE Trans.Sonics Ultrason. SU-21, 98.
- Rowland, T. J., 1962, Phys.Rev. 125, 459.
- Sagalyn, P. L. and Alexander, M. N., 1977, Phys.Rev. B15, 5581.
- Segall, B., 1962, Phys.Rev. 125, 109.
- Seraphin, B. O., 1972, in "Optical Properties of Solids", (ed. F. Abelés), N.Holland, Amsterdam, p.163.  
 \_\_\_\_\_, 1973, editor : "Proceedings of First International Conference on Modulation Spectroscopy", Surface Science, Vol. 37.
- Shewman, P. G., 1963, "Diffusion in Solids", McGraw-Hill, New York.
- Slater, J. C. and Koster, G. F., 1954, Phys.Rev. 94, 1498.
- Smith, N. V., 1979, Phys.Rev. B19, 5019.  
 \_\_\_\_\_ and Matthiess, L. F., 1974, Phys.Rev. B9, 1341.
- Soven, P., 1967, Phys.Rev. 156, 809.
- Stern, E. A., 1966, Phys.Rev. 144, 545.  
 \_\_\_\_\_, 1968, Phys.Rev. 168, 730.  
 \_\_\_\_\_, 1973, Phys.Rev. B7, 1303.  
 \_\_\_\_\_, 1976, Phys.Rev. B13, 621.
- Stroud, D. and Ashcroft, N. W., 1971, J.Phys. F1, 113.
- Szczepanek, P. and Glosser, R., 1974, Solid State Commun. 15, 1425.
- Templeton, I. M. and Coleridge, P. T., 1975, J.Phys. F5, 1307.



- Vassamillet, L. F. and King, H. W., 1967, in "Handbook of X-Rays" (ed. E. F. Kaelble), McGraw-Hill, New York, pp.9-21.
- Velicky, B., Kirkpatrick, S. and Ehrenreich, H., 1968, Phys.Rev. 175, 747.
- Vook, R. W. and Witt, F., 1965, J.Appl.Phys. 36, 2169.
- Wooten, F., 1972, "Optical Properties of Solids", Academic Press, New York.
- Zeller, R. and Dederichs, P. H., 1979, Phys.Rev.Lett. 42, 1713.
- Ziman, J. M., 1960, Phil.Mag. 5, 757.